

EXCITED STATE BEHAVIOR OF MOLECULAR AND HETEROGENEOUS
SYSTEMS: ELECTRON TRANSFER AND VIBRATIONAL COOLING

By MENGDI LIU

A dissertation submitted to the

Graduate school- Newark

Rutgers, The state university of New Jersey

In partial fulfillment of the requirements

for the degree of

Doctor of Philosophy

Graduate Program in Chemistry

Written under the direction of

Professor Piotr Piotrowiak

and approved by

Newark. New Jersey

May 2020

© [2020]

Mengdi Liu

ALL RIGHTS RESERVED

Abstract

EXCITED STATE BEHAVIOR OF MOLECULAR AND HETEROGENEOUS SYSTEMS: ELECTRON TRANSFER AND VIBRATIONAL COOLING

By MENGDI LIU

Dissertation director: Dr. Piotr Piotrowiak

This thesis consists of five chapters. Chapter 1 gives a brief introduction of the concepts and mechanisms regarding radiative and nonradiative decay processes of an excited state, followed by the discussion on how the overall electronic and optical properties of a system change upon alteration of these decay processes. Three examples in either molecular or heterogeneous materials that covered three projects were discussed in detail to enrich the context of this work, which can be found in Chapter 3 to Chapter 5. The experimental techniques used in this thesis were summarized in Chapter 2.

In the first project (Chapter 3), excited state behavior of both single strand and bulk RR-P3HT in contact with an Au nanowire array was studied. By utilizing pump-probe spectroscopy and single molecule fluorescence spectroscopy, information about electron transfer of photoexcited P3HT both in a bulk layer (P3HT@AuNR) and at single molecular level (SMP3HT@AuNR) was obtained. The results showed multifaceted influence of AuNRs on energy and electron transfer processes in P3HT@AuNR. While single molecule measurements show strong enhancement of fluorescence of P3HT, the average lifetime of singlet excitons is dramatically reduced due to efficient quenching by AuNRs.

The second project (Chapter 4) focused on the nonradiative, vibrational cooling in a series of oligovioloens consists of MV^{+*} with different size and topology. Ultrafast transient absorption spectroscopy and classical molecular dynamics (MD) simulations were employed. The results show ballistic vibrational energy transfer at early times in all oligomers. Partially cooled molecules show more pronounced size dependence caused by diffusive vibrational energy transfer. Interference effects brought about by symmetric, equivalent pathways and slower cooling were observed in the meta linked “star” topology.

Later we compared initial transient kinetics in singly reduced (MV^{+*} - MV^{++}) and doubly reduced (MV^{++} - MV^{++}) methyl viologen dimers to investigate the influence of electron transfer upon the rate of internal conversion of MV^{+*} when coupled to MV^{++} . The frequency mismatch between singly and doubly reduced methyl viologen moieties in MV^{+*} - MV^{++} dimer was proved to cause a slower vibrational cooling rate.

The final project looked into the excited state dynamics of an anthracenylboronic compound that contains sterically crowded anthracene and phenyl substituents. Transient absorption measurements and molecular orbital calculations as well as theoretical modeling by semi-classical Marcus-Jortner equation were employed to investigate solvent effect upon photoninduced intramolecular charge transfer and its emission. The results revealed the nature of the charge separated state in such compound: a slight electron density shift from anthracene groups to boron atom instead of a complete charge transfer. The corresponding fluorescence is quenched in more polar solvents, which is caused by the reverse of the dipole moment orientation in this compound upon the transition from S_1 to S_0 . In addition, with the help of careful thermodynamic calculations and the comparison between transient decay kinetics in acetonitrile and in hexane, it was found that the

transition between localized singlet excited state (S_A) and partially delocalized state (S_1) and intersystem crossing from S_1 to T_1 accelerate in more polar solvents.

Acknowledgements

I would like to express my appreciation to the chemistry department at Rutgers- Newark for the opportunity to come here and the funding as well as numerous support in the past seven years,

I would like to express my gratitude to my Ph.D. advisor Dr. Piotr Piotrowiak. He has been very patient and always generous with sharing his knowledge with others. He encouraged me too many times in the past few years, without his support, I might have given up and quit. His dedication to science and passion to research set a good example to not only me but also many others in the group.

I also want to thank my collaborators, Dr. Iyoda, Dr. Kawauchi, Dr. Vacha and Dr. Thilagar for their time and effort in synthesis of the compounds I used in this thesis. It has been an honor for me to work with them.

Many thanks go to my colleagues. Jianhua taught me how to operate the laser system with great patience. Vivid has been my dear friend. We not only spent happy times but also conquered difficulties in laboratory together. Jaren has been very kind and covered for me many times with teaching when I was late in the morning. I wish Lujia and Yaroslav good luck and happiness in the future.

Great appreciation goes to my family. Thank my parents for their love. Thank my lovely husband, who never comforted me with just words but with great patience and caring, not to mention the random financial support. Thank my beloved cat, Dingding, for being a good listener and friend.

Lastly, I would like to thank the committee members, Dr. Jaekle, Dr. Pavanello and Dr. Kohler for their time and inputs for this thesis.

Table of Contents

Abstract	ii
Acknowledgements	v
Table of Contents	vii
List of Figures	xi
List of Tables	xvii
Chapter 1. Introduction of radiative and non-radiative decay of excited states	1 -
1.1 Radiative transitions and plasmonic effects	3 -
1.1.1 Plasmons and surface plasmon resonance effect	5 -
1.1.2 Effects on radiative decay	6 -
1.2 Non-radiative transitions	9 -
1.2.1 Phonons and heat transport	10 -
1.2.1.1 Ballistic and diffusive heat transport	11 -
1.2.1.2 Thermal conduction in molecular junctions and quantum interference effects	12 -
1.2.2 Quenching of excited states via electron transfer	14 -
1.2.2.1 Marcus theory for electron transfer	15 -
1.2.2.2 Long distance electron tunneling	18 -
References:	20 -

Chapter 2.	Experimental methodology	- 24 -
2.1	Pump-probe spectroscopy	- 24 -
2.1.1	Transient absorption system 1	- 25 -
2.1.2	Transient absorption system 2	- 26 -
2.2	Computational simulations.....	- 27 -
2.2.1	Molecular orbital calculations.....	- 27 -
2.2.2	Molecular dynamics simulations	- 28 -
2.3	Single molecule fluorescence spectroscopy	- 29 -
2.4	Steady state spectroscopy and others	- 30 -
	References.....	- 31 -
Chapter 3.	Excited state behavior of single strand and bulk P3HT in contact with an Au nanowire array	- 32 -
3.1	Introduction	- 33 -
3.1.1	Properties of RR-P3HT.....	- 34 -
3.1.2	Charge carrier generation in P3HT@AuNR.....	- 36 -
3.2	Sample preparation.....	- 39 -
3.3	Results and discussion.....	- 40 -
3.3.1	Pump-probe measurement	- 41 -
3.3.2	Single molecule spectroscopy.....	- 49 -
3.4	Conclusions	- 56 -

References	- 58 -
Chapter 4. Vibrational cooling and electron transfer in oligomeric viologens of different size and topology	- 63 -
4.1 Introduction	- 64 -
4.1.1 Properties of the methyl viologen radical cation	- 66 -
4.2 Sample preparation.....	- 69 -
4.3 Vibrational cooling in linear and branched oligoviologens	- 70 -
4.3.1 Steady state absorption measurements.....	- 70 -
4.3.2 Pump-probe experiments	- 71 -
4.3.3 MD simulations.....	- 79 -
4.4 Electron transfer competes with a conical intersection in $MV^{+\bullet}$ – MV^{++} and $MV^{+\bullet}$ – $MV^{+\bullet}$ dimeric viologens	- 82 -
4.4.1 Ground state absorption spectra.....	- 82 -
4.4.2 Pump-probe measurements	- 83 -
4.5 Conclusions	- 89 -
References	- 92 -
Chapter 5. Excited state dynamics of an anthracenylboronic compound.....	- 96 -
5.1 Introduction	- 96 -
5.2 Sample preparation.....	- 99 -
5.3 Results and discussion.....	- 100 -

5.3.1	Steady state absorption	- 100 -
5.3.2	Charge transfer emission of BN.....	- 106 -
5.3.3	Transient absorption measurements.....	- 112 -
5.4	Conclusion.....	- 121 -
	References.....	- 123 -

List of Figures

Figure 1.1	Jablonski energy diagram.	- 1 -
Figure 1.2	Comparison of time scales of decay pathways of an excited state.	- 2 -
Figure 1.3	Schematics for absorption and emission.	- 3 -
Figure 1.4	Schematic diagram of the 3-level lasing system of ruby.	- 4 -
Figure 1.5	Schematic diagram for SPR and LSPR.	- 5 -
Figure 1.6	IC, IVR and VC in a hot molecule.	- 10 -
Figure 1.7	Flow chart of heat transfer mechanisms in molecular junctions.	- 11 -
Figure 1.8	Schematic representation of ballistic and diffusive heat transport.	- 11 -
Figure 1.9	The out of plane phonon modes for free benzene molecule and eigen-modes 3,4 are superposed to form LPM.	- 14 -
Figure 1.10	The Marcus parabola and three regions defined by the Marcus theory.	- 15 -
-		
Figure 2.1	Scheme of the pump-probe set-up using multi-pass amplifier and lock-in detection.	- 25 -
Figure 2.2	Scheme of the pump-probe set-up using regenerative amplifier and photodiode array detection.	- 26 -
Figure 2.3	Scheme of the single molecule fluorescence microcope.	- 29 -
Figure 3.1	Schematic representation of P3HT@AuNR.	- 33 -
Figure 3.2	Structure of RR-P3HT and RRa-P3HT.	- 34 -
Figure 3.3	Edge-on and face-on packing of crystalline RR-P3HT.	- 36 -

Figure 3.4	Competing radiative and non-radiative processes in a polymeric material. ...	37 -
Figure 3.5	(Left) Schematic representation of the nanowire array filled with P3HT. The side view of P3HT@AuNR is shown on the left, a horizontal slice on the right. (Right) Top view of the Au-nanowire array with two-zone division.	39 -
Figure 3.6	Absorption spectrum of P3HT@glass and the difference spectrum $\Delta A = A_{\text{P3HT@AuNR}} - A_{\text{AuNR}}$. All spectra were collected at normal incidence.	41 -
Figure 3.7	Computed positions and intensities of low-lying electronic transitions of the S_0 , S_1 and T_1 states, as well the radical cation and radical anion of a regioregular tetramer (a) and octamer (b) of 3-methylthiophene. The DFT (B3LYP, 6-31G*) calculations were carried out using Spartan'16 by Wavefunction, Inc.	42 -
Figure 3.8	Transient absorption spectra of (a) P3HT@glass; (b) P3HT@AuNR. Data collected under 525 nm excitation at different delay times.	44 -
Figure 3.9	Normalized transient absorption decay profiles and the fits (red) obtained for P3HT@glass (blue) and P3HT@AuNR (green) at probe wavelengths of: (a) 668 nm; (b) 876 nm; (c) 1032 nm.	46 -
Figure 3.10	Single molecule fluorescence blinking profiles for P3HT embedded in PMMA deposited on the Au-nanorod array (a-d) and on glass (e-f). Each trace shows the photon count of a randomly selected emitter plotted versus time.	49 -
Figure 3.11	The average autocorrelation curves of P3HT embedded in PMMA on Au nanorod array (blue) and on glass (green).	53 -

Figure 3.12	(a) Averaged single molecule emission spectra measured on glass (red) and the Au nanorod substrate (black); (b) Normalized double Gaussian fits of the spectra in (a) plotted together with the spectrum of the Au nanorod array (blue).....	55 -
Figure 4.1	Molecular structure of oligomers. (a) Monomer. (b) Para (linear) dimer. (c) Para (linear) trimer. (d) Meta dimer. (e) Meta (star) dimer.	64 -
Figure 4.2	Schematic diagram showing the monoreduction of MV^{++} and the photoexcitation of $MV^{+\bullet}$	67 -
Figure 4.3	3D plot of energy versus varying dihedral angle and central bond lengths in D_0 and D_1 states of $MV^{+\bullet}$ and the S_0 state of MV^{++}	68 -
Figure 4.4	Structure of the singly (top) and doubly (bottom) reduced dimer.	69 -
Figure 4.5	Ground state absorption of the reduced monomer (blue), linear dimer (red), meta dimer (light green), linear trimer (black) and star trimer (olive).	71 -
Figure 4.6	(a) Normalized transient absorption spectra of the reduced monomer (blue), linear dimer (red), meta dimer (light green), linear trimer (black) and star trimer (olive) at 4 ps after excitation at 550 nm. (b) Overlay of ground state absorption and TA spectrum at 4 ps spectrum of the reduced dimer.	73 -
Figure 4.7	Transient absorption decay profiles for the monomer (blue), para dimer (red), meta dimer (light green), linear trimer (black) and star trimer (olive) excited at 550 nm and probed at different wavelengths: (a) 703 nm; (b) 762 nm; (c) 845 nm.....	75 -
Figure 4.8	Survival time vs. population profiles at different probe wavelengths. Blue: monomer; Red: dimer; Black: linear trimer; Green: star trimer.	78 -

Figure 4.9	Averaged MD trajectories of the hot viologen (black), cold viologen (blue) and the bridge (red) in: (a) para dimer; (b) linear trimer; (c) meta dimer; (d) star trimer. ...	80 -
Figure 4.10	Normalized ground state absorption spectra of the $MV^{+\bullet}$ monomer (blue), the $MV^{+\bullet}-MV^{++}$ dimer (red) and $MV^{+\bullet}-MV^{+\bullet}$ dimer (black).....	83 -
Figure 4.11	Transient decay kinetics at early times probed at 703, 762 and 845 nm....	84 -
Figure 4.12	Schematic representation of the competing internal conversion (IC) and electron transfer (ET) deactivation pathways of the D_1 excited state in the mixed-valence $MV^{+\bullet}-MV^{++}$ and the doubly reduced $MV^{+\bullet}-MV^{+\bullet}$ redox form of the dimer.	86 -
Figure 4.13	Transient decay profiles of $MV^{+\bullet}-MV^{+\bullet}$ and $MV^{+\bullet}-MV^{++}$	87 -
Figure 4.14	Vibrational frequency matching between $MV^{+\bullet}$ (green line on the left) and MV^{++} (red line on the right) normal modes based on B3LYP, 6-31G** calculations (Spartan '16). The frequency overlap based on an arbitrary 15 cm^{-1} linewidth is shown in solid blue on both sides of the graph. The high frequency CH stretching modes are of minor relevance to the cooling process and were not included.	89 -
Figure 5.1	Structure of borazane, borazene and borazine.	97 -
Figure 5.2	Conformational change of aminoborane upon photoexcitation.....	97 -
Figure 5.3	Structure of the BN molecule.	98 -
Figure 5.4	3D plot of the ground state energy of BN plotted as a function of the dihedral angle and the B-N bond order.	99 -
Figure 5.5	UV-Vis spectra of BN in different solvents.....	100 -
Figure 5.6	Simulated UV-VIS spectrum of BN in vacuum.	101 -

Figure 5.7	Molecular orbitals of BN with arrows indicating the contributions to the low-lying electronic transitions.	- 102 -
Figure 5.8	Calculated B-N bond lengths with respect to different dihedral angles in the S_0 and the S_1 of BN. Green stars show the optimum B-N bond length and the dihedral angle at both states.	- 104 -
Figure 5.9	Structures of the reference molecules and the HOMO, LUMO orbitals for 9-anthracene boronic acid.	- 105 -
Figure 5.10	UV-Vis spectra of the reference molecules in hexane.	- 106 -
Figure 5.11	Emission spectrum of BN in hexane.	- 107 -
Figure 5.12	Charge transfer emission spectra of BN in different solvents. Inset: Normalized charge transfer emission spectra of BN.	- 108 -
Figure 5.13	Charge transfer emission spectra of BN in various solvents and the corresponding fits by the Marcus-Jortner equation.	- 109 -
Figure 5.14	Schematic diagram showing the change of dipole moment orientation with arrows in BN molecule.	- 111 -
Figure 5.15	Energy level diagram of BN.	- 112 -
Figure 5.16	DFT calculated spin density of the triplet state in comparison with the HOMO orbital of S_0 of BN.	- 113 -
Figure 5.17	2D transient absorption maps of BN molecule in acetonitrile and hexane obtained upon 390 nm and 450 nm excitation. The transient spectrum of the reference compound 9-anthracene boronic acid in hexane obtained upon excitation of 390 nm is shown at the bottom.	- 114 -

Figure 5.18	1D transient absorption spectra of BN with 390 nm excitation in acetonitrile and in hexane.	- 115 -
Figure 5.19	Schematic diagram of the energy levels involved in the deactivation of the S _A state in BN molecule.....	- 116 -
Figure 5.20	Transient decay kinetics of BN obtained upon 390 nm excitation in acetonitrile and in hexane, probed at 700 nm.	- 117 -
Figure 5.21	1D transient absorption spectra of BN obtained upon 450 nm excitation in acetonitrile and in hexane.	- 119 -
Figure 5.22	Transient decay kinetics of BN obtained upon 450 nm excitation in acetonitrile and in hexane, probed at 700 nm.	- 120 -

List of Tables

Table 3.1	Double exponential decay fitting parameters for transient dynamics probed at 650, 850 and 1000 nm in P3HT@AuNR and P3HT@Glass	- 47 -
Table 3.2	Time constants recovered from the autocorrelation curves shown in Figure 3.11.	- 54 -
Table 3.3	Fitting parameters retrieved from the fluorescence spectra in Figure 3.12. ...	- 55 -
Table 4.1	Rise time of populations probed at 703 nm, 762 nm and 845 nm in the linear dimer excited at 550 nm.....	- 72 -
Table 4.2	Double exponential decay fitting parameters of monomer, linear dimer, meta dimer, linear trimer and meta trimer excited at 550nm and probed at 703 nm, 762 nm and 845 nm.	- 76 -
Table 4.3	Fitting parameters for the cooling of hot viologen units as well as the heating of the bridge moieties and the cold viologens. Energy gain by bridging moieties of meta dimer is absent due to poor fitting convergence.	- 81 -
Table 4.4	The rates of the formation of the hot ground state in the studied viologen systems probed at several wavelengths. The Δk_{decay} is the difference between the hot ground state formation rate in $MV^{+\bullet}-MV^{++}$ and $MV^{+\bullet}-MV^{+\bullet}$	- 85 -
Table 4.5	Kinetic parameters of the cooling of the hot ground state probed at 845 nm for monomer, para dimer and meta dimer.	- 88 -
Table 5.1	Molecular orbital composition of the calculated absorption bands of BN. The color shading corresponds to the transitions indicated in Figure 5.7.....	- 103 -

Table 5.2	Charge transfer fluorescence fitting parameters obtained by using the Marcus-Jortner equation.	- 110 -
Table 5.3	Single exponential growth fitting parameters gathered for transient decay kinetics upon 390 nm excitation of BN in acetonitrile and hexane.	- 117 -
Table 5.4	Single exponential growth fitting parameters gathered for transient decay kinetics upon 450 nm excitation of BN in acetonitrile and hexane.	- 121 -

Chapter 1. Introduction of radiative and non-radiative decay of excited states

The decay of an excited state of any system, as shown in the Jablonski energy diagram [1] in Figure 1.1, can be either radiative or non-radiative. In radiative transitions, photons are emitted in the form of fluorescence or phosphorescence. For non-radiative processes, excess energy is dissipated within multiple energy levels of the system in a form other than photon through several pathways such as the internal conversion from S_{n+1} to S_n , internal vibrational relaxation from $v=n$ to $v=0$, as well as intersystem crossing from S_n to T_m . If the system is coupled to other molecules, quenching of the excited state via collision, electron transfer or electronic energy transfer are also possible. These decay processes occur on different time scales as shown in Figure 1.2. The rate for each process is the reciprocal of corresponding lifetime $\kappa = \frac{1}{\tau}$.

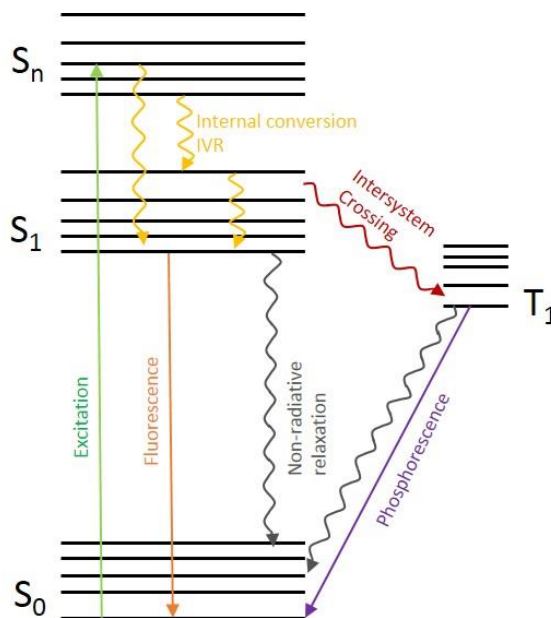


Figure 1.1 Jablonski energy diagram.

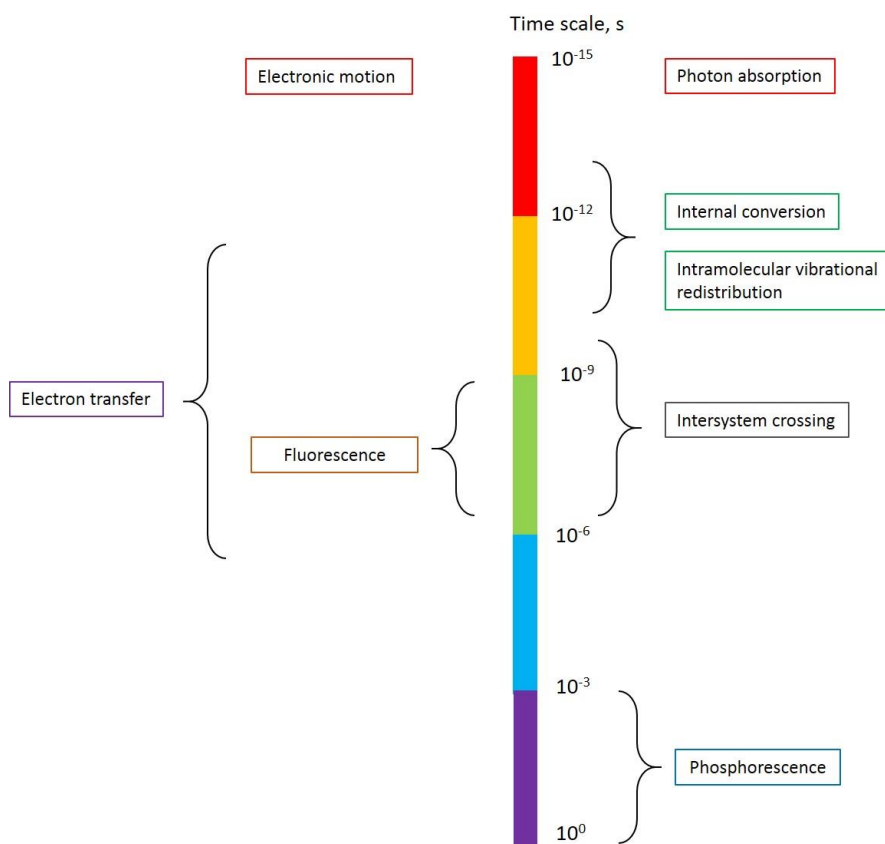


Figure 1.2 Comparison of time scales of decay pathways of an excited state.

The competition between radiative and non-radiative processes determines the emission quantum yield of the system,

$$\Phi = \frac{\kappa_{rad}}{\kappa_{rad} + \kappa_{nrad}} \quad (1.1)$$

where κ_{rad} and κ_{nrad} represent the rates of the radiative decay and non-radiative decay processes. The rate for nonradiative decay can be further written as

$$\kappa_{nrad} = \kappa_{ic} + \kappa_{isc} + \kappa_{et} + \kappa_{eet} + \kappa_{reaction} \quad (1.2)$$

These decay processes are vital in determining the optical properties of materials and are intensely studied by researchers [2]. How to effectively alter the rates of the decay processes and ultimately control the optical properties of materials has been the key question asked by physical chemists. In the next few sections of this chapter, the detailed mechanisms regarding decay processes together with some of the property altering approaches will be discussed.

1.1 Radiative transitions and plasmonic effects

Emission can be spontaneous or stimulated (Figure 1.3). Spontaneous emission is most common in materials where quantized energy is emitted in terms of photons from higher electronic states to lower electronic states. On the contrary, in stimulated emission, the incoming photon of specific frequency can interact with an excited state, causing it to drop to a lower energy level and creating a new photon identical to the incoming photon. Stimulated emission together with population inversion and proper feedback are the bases for lasing. Figure 1.4 shows a schematic diagram of a 3-level system for lasing.

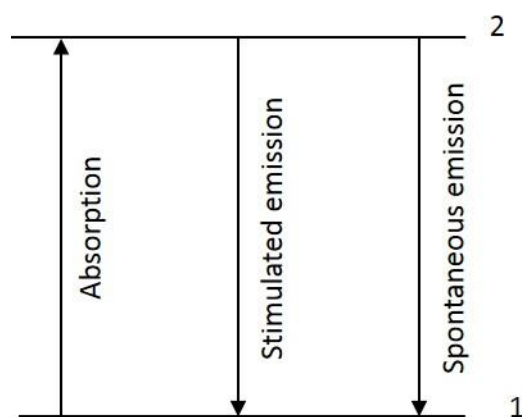


Figure 1.3 Schematics for absorption and emission.

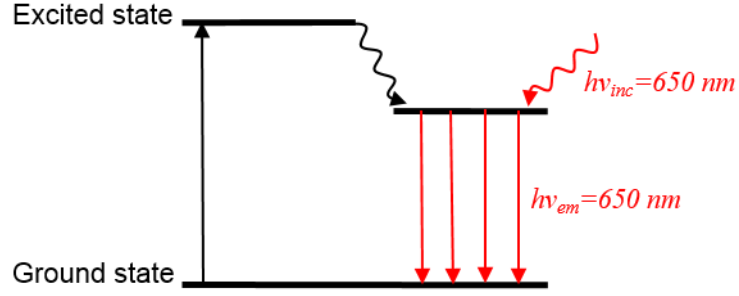


Figure 1.4 Schematic diagram of the 3-level lasing system of ruby.

The rate of each transition can be expressed as follows [2, 3]:

$$\left(\frac{d(N_1)}{dt}\right)_{abs} = -B_{12}\rho(\nu)N_1 \quad (1.3)$$

$$\left(\frac{d(N_2)}{dt}\right)_{spontaneous} = -A_{21}N_2 \quad (1.4)$$

$$\left(\frac{d(N_1)}{dt}\right)_{stimulated} = -B_{21}\rho(\nu)N_2 \quad (1.5)$$

where B and A are the Einstein's coefficients for absorption and emission, N represents the populations of the representative states and $\rho(\nu)$ is the radiation density at the frequency of the transition. In addition, we have

$$\tau_{rad} = \frac{1}{\kappa_{rad}} = \frac{1}{A} \quad (1.6)$$

and

$$A = \frac{16\pi^3\nu^3n^3}{3\epsilon_0hc^3}|\mu_{12}|^2, B = \frac{2\pi^2}{3\epsilon_0h^2}|\mu_{12}|^2 \quad (1.7)$$

where ϵ_0 is vacuum permittivity, n is the index of refraction, h represents Planck's constant, c is the speed of light and μ the transition dipole moment. Therefore,

$$\kappa_{rad} \propto |\mu|^2 \quad (1.8)$$

From Equation 1.8, we can easily conclude that by applying changes to the transition dipole moment of the system, the radiative transition rate will be affected and alter the emission properties of the molecule. This type of the alteration can be accomplished through a variety of electronic field effects. Among all, surface plasmon enhancement effects by nanostructured metals has been an active field of research for many years [4-6]. In Chapter 3, an example of multifaceted influence of gold nanorod array on excited state behavior of P3HT will be discussed.

1.1.1 Plasmons and surface plasmon resonance effect

When electromagnetic radiation is incident on a metal, it induces a collective oscillation of electrons and generates a strong electric field. In thin metal films (SPR), the oscillating electron waves, also called plasmons, can propagate tens to hundreds microns along the interface. If the resonance takes place in metal nanoparticles with size much smaller than incident wavelength, the plasmons are localized around the nanostructure and give rise to an intense, highly localized electromagnetic field. This phenomenon is called localized surface plasmon resonance (LSPR) [7]. LSPR is common in nanostructured noble metals such as silver nanoparticles, gold nanoparticles etc. Both SPR and LSPR are capable of altering the excited state behavior in semiconductors and molecules in close proximity and are frequently coupled to chromophores such as conjugated polymers or quantum dots.

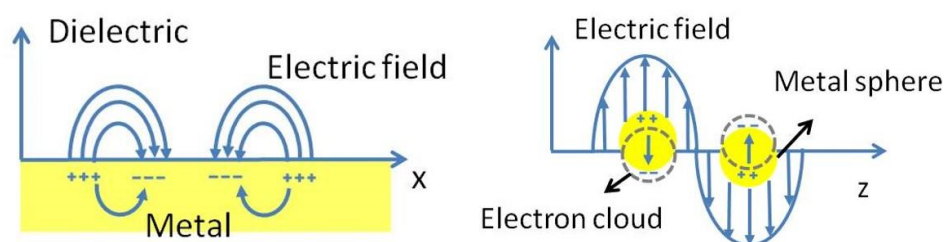


Figure 1.5 Schematic diagram for SPR and LSPR.

1.1.2 Effects on radiative decay

One of the most interesting applications of SPR or LSPR is the enhancement of the luminescence of chromophores [5], including both fluorescence and phosphorescence. The luminescence intensity of a chromophore is proportional to absorbed light intensity P_0 and the quantum yield Φ [8, 9]. Therefore, the overall enhanced luminescence I in presence of a nanobody can be expressed as

$$I(\omega, \omega', \mathbf{r}) \propto P_0 G(\omega, \mathbf{r}) \Phi(\omega, \mathbf{r})$$

$$= P_0 \left| \frac{\mathbf{E}(\omega, \mathbf{r})}{\mathbf{E}_0(\omega)} \right|^2 \frac{\gamma_{rad}(\omega', \mathbf{r})}{\gamma_{rad}(\omega', \mathbf{r}) + \gamma_{nonrad}(\omega', \mathbf{r})} \quad (1.9)$$

where ω and ω' is the excitation and emission radiation frequency. From Equation 1.9, one can easily conclude that the enhancement of luminescence of a chromophore in the presence of a metal nanoparticle comes from two sources: the change of the intensity of incident photon and quantum yield of the chromophores. The enhancement of excitation light in the presence of metal nanoparticles can be expressed in terms of the intensity enhancement factor G :

$$G = \left| \frac{\mathbf{E}(\omega, \mathbf{r})}{\mathbf{E}_0(\omega)} \right|^2 \quad (1.10)$$

where \mathbf{E} and \mathbf{E}_0 represent the electric field of incident light with frequency ω in the presence and in the absence of the metal nanobody. If we consider the G factor near a spherical nanoparticle of radius a and at a distance \mathbf{r} , we obtain the electric field generated by the nanoparticle

$$\mathbf{E}_P = -\frac{\mathbf{d}_p}{r^3} + 3\frac{(\mathbf{d}_p \mathbf{r})\mathbf{r}}{r^5} \quad (1.11)$$

where \mathbf{d}_p is the induced dipole moment of the nanoparticle

$$\mathbf{d}_p = \alpha \mathbf{E}_0 \quad (1.12)$$

with $\alpha = \frac{a^3(\varepsilon-1)}{\varepsilon+2}$ being the polarizability of spherical particle with dielectric permittivity of ε . Since $\mathbf{E} = \mathbf{E}_0 + \mathbf{E}_p$, applying Equation 1.11 and 1.12 to Equation 1.10, yields

$$\begin{aligned} G_{norm} &= \left| 1 + 2 \left(\frac{\varepsilon-1}{\varepsilon+2} \right) \left(\frac{a}{r} \right) \right|^2 \\ G_{tang} &= \left| 1 - \left(\frac{\varepsilon-1}{\varepsilon+2} \right) \left(\frac{a}{r} \right) \right|^2 \end{aligned} \quad (1.13)$$

where the two G factors represent the radial and tangential orientation of \mathbf{E}_0 field with respect to the nanoparticle.

The presence of metal nanoparticle also alters the rate of spontaneous emission by adding induced dipole moment $\delta \mathbf{d}$ to the dipole of the chromophore. Therefore, the enhancement factor of spontaneous emission rate η can be expressed as:

$$\eta = \frac{\gamma_{rad}}{\gamma_0} = \frac{|\mathbf{d}_0 + \delta \mathbf{d}|^2}{|\mathbf{d}_0|^2} \quad (1.14)$$

where γ_0 is the radiative decay rate without the metal nanoparticle and \mathbf{d}_0 is the dipole moment of the chromophore in vacuum.

The induced dipole moment of a chromophore in the presence of a metal nanoparticle can be derived as

$$\delta \mathbf{d} = a^3 \left(\frac{\varepsilon-1}{\varepsilon+2} \right) \left[-\frac{\mathbf{d}_0}{r^3} + 3 \frac{(\mathbf{d}_0 \mathbf{r}) \mathbf{r}}{r^5} \right] \quad (1.15)$$

Combining Equation 1.14 and 1.15, the enhancement factor of spontaneous emission rate η can be expressed as Equation 1.16.

$$\eta_{norm} = \left| 1 + 2 \frac{(\varepsilon - 1)}{(\varepsilon + 2)} \left(\frac{a}{r} \right)^3 \right|^2$$

$$\eta_{tang} = \left| 1 - \frac{(\varepsilon - 1)}{(\varepsilon + 2)} \left(\frac{a}{r} \right)^3 \right|^2$$
(1.16)

Therefore, $\Phi' = \frac{\eta\gamma_{rad}}{\eta\gamma_{rad} + \gamma_{nonrad}}$.

Experimentally, according to Beer's law,

$$A = kbc = \log P_0 - \log P$$
(1.17)

with k corresponding to molar absorption coefficient, P_0 and P is the incident light intensity before and after passing through the material, respectively. The corresponding fluorescence intensity of a chromophore can be written as

$$I = \Phi \cdot P_0 \cdot (1 - 10^{-\varepsilon bc}) \approx \Phi \cdot P_0 \cdot kbc$$
(1.18)

with Φ being the quantum yield of the chromophore. When coupled to the nanostructured metal, the fluorescence is enhanced and

$$I_{enhanced} = (G \cdot P_0) \Phi' \cdot kbc$$
(1.19)

Equation 1.13 and 1.16 show that the enhancement effects of nanostructured metals are highly dependent on the sizes of nanoparticles as well as the distance between emitter and nanoparticles. Numerous experiments have been done with metal nanoparticles of different size and shape such as spheres, nanorods, etc. and demonstrated enhancements from 2 to 30 fold. In some specially designed nanostructures that can generate “hotspots”-super intense local electric fields, the enhancement of luminescence can be as large as thousands [10-12]. Several other studies also show magnitudes of enhancement of phosphorescence in chromophores [13].

1.2 Non-radiative transitions

Non-radiative decay in molecular systems encompasses multiple processes, which allow the excited states to relax to lower energy levels without emitting photons. When an excited state passes through a conical intersection via internal conversion (IC), and lands onto a non-zero vibrational state of the lower electronic state, the molecule contains certain amount of excess vibrational energy and therefore can be considered “hot”. The excess energy contained by such “hot” molecules can be equivalent to a local temperature of thousands of kelvins, which would be very difficult to achieve by routine experimental techniques, especially in solution. The excess energy can be further dissipated into the manifolds of vibrational levels through intramolecular vibrational relaxation (IVR) and eventually equilibrated with the surrounding environment. Depending on the molecule and the environment, the time scales of IC and IVR can vary from tens of femtoseconds to a few picoseconds. The overall relaxation of such hot molecules with not fully equilibrated vibrational energies can be described by several heat transfer models. Understanding these processes is vital in the study of vibrational cooling. In Chapter 4, vibrational cooling in a series of oligoviologens studied by both pump-probe spectroscopy and MD simulations is reported.

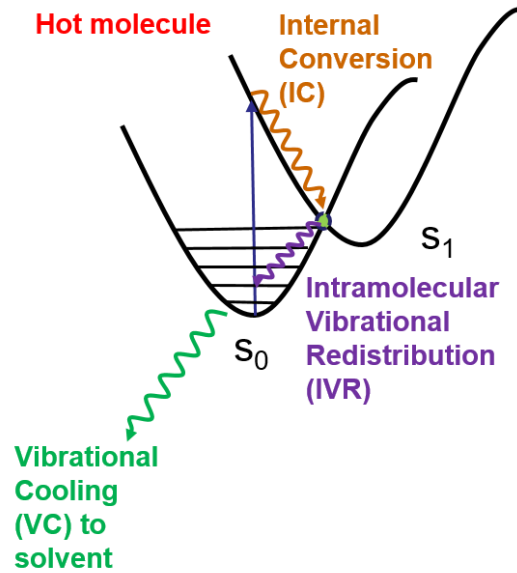


Figure 1.6 IC, IVR and VC in a hot molecule.

1.2.1 Phonons and heat transport

Phonons are quantized lattice vibrations and the major carrier in heat transport. In bulk materials, heat transport is frequently described by Fourier's Law of heat conduction,

$$Q = -\kappa \nabla T \quad (1.20)$$

where Q is the heat flux, κ is the thermal conductivity and ∇T the temperature gradient between the heat baths [14, 15]. However, as the size of system decreases (nanostructures or molecular level) so that the characteristic length becomes comparable to or even smaller than the phonon mean free path, heat conduction can significantly deviate from Fourier's law. Like photons, phonons can be treated either as waves or particles. The division is determined by the comparison between the system's characteristic length and the phonon coherence length. If the characteristic length is less than or comparable to the phonon coherence length, the phonon behaves similarly to a wave. Otherwise, they are treated as

particles. In most cases, the coherence length of phonons is very small. Therefore, phonons are often treated as particles.

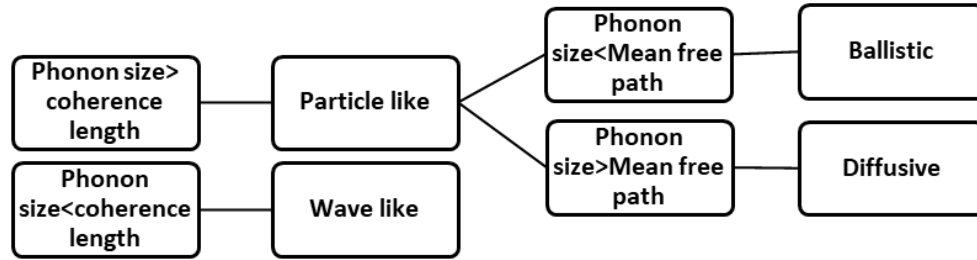


Figure 1.7 Flow chart of heat transfer mechanisms in molecular junctions.

Under the particle regime, depending on the relative amplitude of phonon mean free path l versus the size of the system L , two limiting regimes, ballistic and diffusive models are best suited to describe heat conduction [16, 17].

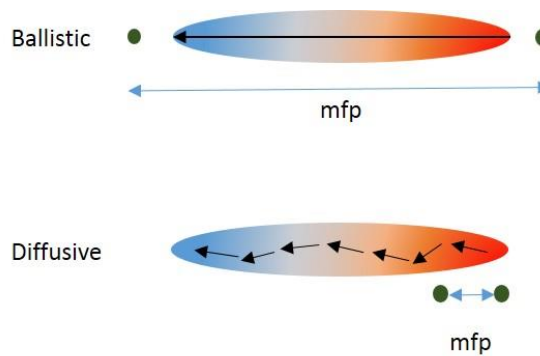


Figure 1.8 Schematic representation of ballistic and diffusive heat transport.

1.2.1.1 Ballistic and diffusive heat transport

As shown in Figure 1.8, diffusive transport occurs via random walk IVR, which is driven by the anharmonic interactions between the relevant modes when the phonon mean free path l is much smaller than the size of molecule L . In other words, the IVR process should

generally be diffusive. For diffusive transport, the distance traversed by heat is linearly proportional to time.

$$\frac{dE}{dt} = -\kappa \frac{\partial T}{\partial x} \quad (1.21)$$

Diffusive transport is frequently observed in bulk and disordered materials such as peptides and glasses.

In the case of $l > L$, ballistic transport is possible. This type of transport requires states delocalized over the whole molecule and the excitation of a superposition of these states. It is dominant in ordered structures such as polymers with identical repeat units. The energy flow occurs in a one-step manner from the hot site of the molecule with temperature T_2 to the cold site with temperature T_1 and is independent of distance.

$$\frac{dE}{dt} = -\kappa'(T_2 - T_1) \quad (1.22)$$

In relatively small molecules with sizes from 5 to 50 Å, distinction between diffusive and ballistic transport is not well defined. As a result, harmonic and anharmonic models are frequently used in these systems. In the harmonic model, the transport is coherent and shows ballistic current features. In the anharmonic model, a key signature is the temperature dependence of thermal conductance, which is observed when inelastic phonon scattering is dominant [18, 19].

1.2.1.2 Thermal conduction in molecular junctions and quantum interference effects

Thermal conduction in molecular junctions can be modeled by several theoretical methods including the generalized Langevin equation for the harmonic approximations or non-equilibrium Green's function for anharmonic effects. Both methods yield Landauer type

expression for the heat flux. Under the harmonic approximation which is prevalent in small molecules, the corresponding thermal conduction can be expressed as

$$\kappa(T) = \frac{\hbar^2}{2\pi k_B T^2} \int_0^\infty d\omega \omega^2 \mathcal{T}(\omega) \frac{e^{\hbar\omega/k_B T}}{(e^{\hbar\omega/k_B T} - 1)^2} \quad (1.23)$$

where $\mathcal{T}(\omega)$ represents the frequency-dependent phonon transmission function and T is the average temperature of the molecular junction [19].

Like in the case of electron transport, heat transport can also exhibit interference effects [20, 21]. The quantum interference (QI) effect is usually observed in cross-conjugated molecules which can bring destructive influence toward electronic conductance and is caused by the presence of nodes in the transmission functions [22-24]. A simple example is the para versus meta linked benzene molecule as shown in Figure 8. In a free benzene molecule, six out-of-plane phonon modes can be observed. The different size and color of the dots in Figure 1.9 represent modes with different amplitude of displacement and phase. Among all modes, modes 1,6 as well as 3,4 and 2,5 are three pairs of eigen-modes. When two leads are connected to benzene in meta positions, the linear combinations of eigen-modes 3,4 or 2,5 or 1,6 can form localized phonon modes (LPM) that closely resemble the situation of a Fano resonance (Figure 1.9 bottom), where a localized state (3+4) is coupled to a continuum (3-4). Such LMP topology is known to cause transmission node at the vibrational frequency of LPM. In the case of para linked benzene, transmission nodes are absent.

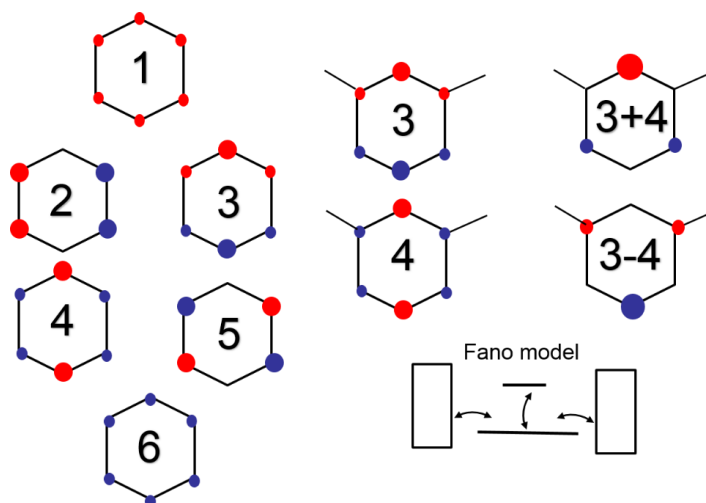


Figure 1.9 The out of plane phonon modes for free benzene molecule and eigenmodes 3,4 are superposed to form LPM.

Even though the concepts of QI induced destructive effect upon electronic conductance and interference effect upon thermal conductance in cross-conjugated molecules are similar, the magnitude of such effects is different. It has been reported that the electronic conductance in cross conjugated molecules shows 1-3 orders of magnitude of reduction whereas only a factor of 2-5 in thermal conductance was observed. This is due to the intrinsic difference between Fermi- and Bose-Einstein distribution functions. Phonon transmission encompasses contributions from a broader range of modes, while electronic transmission is determined in a narrow energy window around the Fermi level [19, 20].

1.2.2 Quenching of excited states via electron transfer

All non-radiative transitions are governed by Fermi's golden rule [25], which states that the probability of a transition is proportional to time, the square of diagonal element and the respective Franck-Condon weighted density of states. The rate of transition can be expressed as

$$\kappa_{if} = \frac{2\pi}{\hbar} |V_{if}|^2 \rho_{if} \quad (1.24)$$

where V_{if} is the off-diagonal element, ρ_{if} is the density of states.

Depending on different nature of coupling and the representation of the density of the states, the golden rule can be further elaborated for electron transfer and energy transfer.

1.2.2.1 Marcus theory for electron transfer

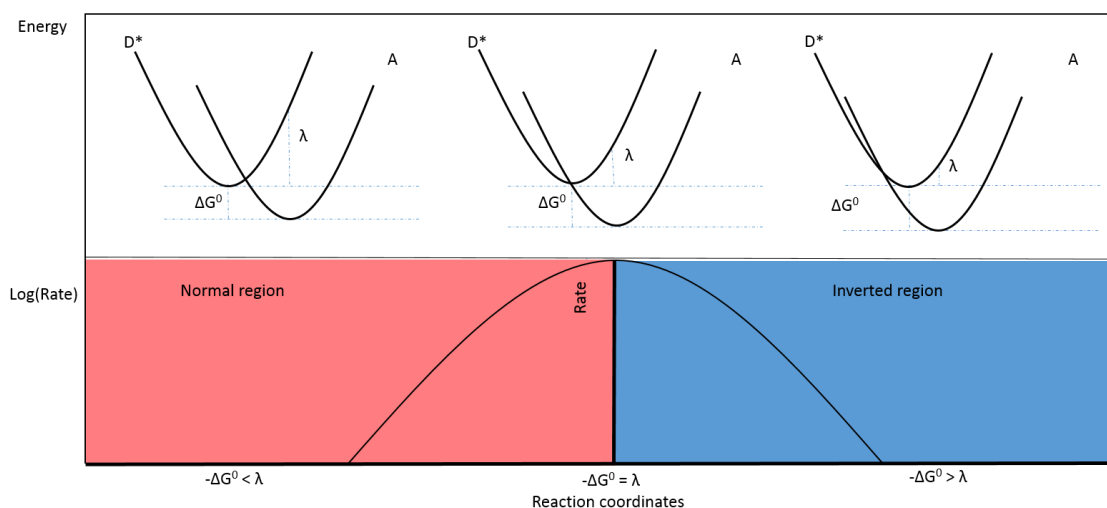


Figure 1.10 The Marcus parabola and three regions defined by the Marcus theory.

In 1956, Marcus developed the classical model for the electron transfer rate [26, 27] based on Fermi's golden rule and Libby's model [28], which states that

$$k_{et} = \left(\frac{1}{4\pi\lambda k_B T} \right)^{1/2} |V|^2 \exp \left[-\frac{(\Delta G^\circ + \lambda)^2}{4\lambda k_B T} \right] \quad (1.25)$$

where V is the electronic coupling between donor and acceptor, ΔG° is the driving force and λ is the reorganization energy.

The comparison between the driving force ΔG° and the reorganization energy λ gives rise to three regions for electron transfer rate:

- 1) Normal region: $-\Delta G^\circ$ is smaller than reorganization energy λ and the electron transfer rate shows positive correlation with driving force.
- 2) Activationless region: $-\Delta G^\circ$ is similar to reorganization energy λ . The reaction is therefore barrierless and the electron transfer rate is at maximum.
- 3) Inverted region: $-\Delta G^\circ$ is larger than reorganization energy λ and the electron transfer rate shows negative correlation with driving force.

The limit of this classical model is that the nuclear reorganization is implicitly assumed to proceed only through low frequency rotational and vibrational modes, however, if high frequency modes are included, the nuclear tunneling effects cannot be neglected. Jortner and co-workers expanded the classical Marcus theory and developed the semi-classical Marcus-Jortner equation, which allows the inclusion of high frequency modes into the overall reorganization energy while the low frequency modes are still treated classically [29]. In this model, the reorganization energy is divided into λ_{inner} for high frequency vibrations of the donor as well as the acceptor and λ_{sol} for low frequency motions of the solvents.

The solvent can be treated as a dielectric continuum, the corresponding reorganization energy λ_{sol} can therefore be approximated by the two-sphere model

$$\lambda_{\text{sol}} = \frac{e}{4\pi\epsilon_0} \left(\frac{1}{2r_{D^+}} + \frac{1}{2r_{A^-}} - \frac{1}{r_{D^+A^-}} \right) \left(\frac{1}{n_s^2} - \frac{1}{\epsilon_s} \right) \quad (1.26)$$

where r_{D^+} , r_{A^-} and $r_{D^+A^-}$ represent the radii for donor, acceptor and the center to center donor-acceptor distance. n_s , ϵ_s represent the refractive index and the solvent dielectric constant, respectively.

The overall rate expression becomes

$$k_{et} = \left(\frac{\pi}{\hbar^2 \lambda_{sol} k_B T} \right)^{1/2} \cdot |V|^2 \cdot \sum_{w=0}^{\infty} \left[\frac{S^w}{w!} \exp(-S) \right] \cdot \exp \left[- \frac{(whv + \Delta G^\circ + \lambda_{sol})^2}{4\lambda_{sol} k_B T} \right] \quad (1.27)$$

where w is the vibrational quantum number and $S = \frac{\lambda_{inner}}{hv}$, v corresponds to the frequency of the most strongly coupled mode in the single mode approximation.

The semi-classical Marcus equation can also be used in the interpretation of charge transfer absorption and emission spectra. The application in both cases is conceptually similar, except for differences in the pre-exponential parameters and signs. For charge transfer absorption, the molar absorptivity can be expressed as [30]

$$\varepsilon_v = \frac{8N\pi^3}{3000h^2cv \ln 10} n^3 V^2 \sum_{i=0}^{\infty} \exp(-S) \frac{S^i}{i!} \exp \left[- \frac{(\Delta G_0 - hv + ihv_V + \lambda_s)^2}{4\lambda k_B T} \right] \quad (1.28)$$

where v is the peak absorption frequency, and v_V is the frequency of the most strongly coupled mode in the single mode approximation.

For charge transfer emission, the intensity can be expressed as [30]

$$I_v = \frac{64\pi^4}{3h^3c^3 \ln 10} n^3 v V^2 \sum_{i=0}^{\infty} \exp(-S) \frac{S^i}{i!} \exp \left[- \frac{(\Delta G_0 + hv + ihv_V + \lambda_s)^2}{4\lambda k_B T} \right] \quad (1.29)$$

where v is the maximum frequency of the emission spectrum, and v_V is the frequency of the most strongly coupled mode in the single mode approximation.

In Chapter 4, we apply the semi-classical Marcus-Jortner equation to a mixed valence dimeric methyl viologen system and calculate the electron transfer rate in such molecular construct. The result is in a surprisingly good agreement with the experimental value. In Chapter 5, semi-classical Marcus equation for charge transfer emission is fitted to a charge transfer emission spectra of a boron-nitrogen compound containing sterically crowded anthracene side groups. Driving forces and solvent reorganization energies are extracted from the spectra, which allows for a more quantitative analysis of the solvent effects on the charge transfer rates in such molecule.

1.2.2.2 Long distance electron tunneling

Electron transfer over long distances that are significantly larger than the sum of van der Waals radii of the donor and the acceptor is possible via electron tunneling [31, 32]. In this case, the electrons from the donor can tunnel through the potential barrier and reach the acceptor site in a single step. The electronic coupling between donor and acceptor is dependent on the separation of donor and acceptor,

$$V(R_{DA}) = V_0 \exp[-\beta(R_{DA} - R_0)] \quad (1.30)$$

Therefore, the rate of electron tunneling is determined by the distance between donor and acceptor R_{DA} as well as the damping factor β .

$$\kappa_{ET} = k_0 \exp[-2\beta(R_{DA} - R_0)] \quad (1.31)$$

The damping factor β has been determined for a variety of media. For instance, saturated hydrocarbon spacers show $\beta \approx 1 \text{ \AA}^{-1}$. Phenylene bridges, depending on the dihedral angles between two adjacent aromatic rings, show β factors between $0.4\text{-}0.8 \text{ \AA}^{-1}$. For polyene and phenylenevinylene bridges, the β factor is as small as 0.04 \AA^{-1} , which results in a very

efficient electron transfer over long distances [31]. In Chapter 3, except for the observation of plasmonic enhancement effect of AuNR toward the emission of P3HT by single molecule measurement, the macroscopic, pump-probe measurements show a dominant quenching of charge carriers in P3HT by electron tunneling. The effect is very sensitive to the distance between charges and the gold just as described in equation 1.31.

References:

1. Lasorne, B., G.A. Worth, and M.A. Robb, *Excited-state dynamics*. Wiley Interdisciplinary Reviews: Computational Molecular Science, 2011. **1**(3): p. 460-475.
2. Turro, N.J., V. Ramamurthy, and J.C. Scaiano, *Principles of molecular photochemistry : an introduction*. 2009, Sausalito, Calif.: University Science Books. xxi, 495 p.
3. McHale, J.L., *Molecular spectroscopy*. 1st ed. 1999, Upper Saddle River, N.J.: Prentice Hall. xv, 463 p.
4. Atwater, H.A. and A. Polman, *Plasmonics for improved photovoltaic devices*. Nature Materials, 2010. **9**(3): p. 205-213.
5. Khurgin, J.B. and G. Sun, *Enhancement of optical properties of nanoscaled objects by metal nanoparticles*. Journal of the Optical Society of America B, 2009. **26**(12).
6. Wang, Z., et al., *Plasmon–polaron coupling in conjugated polymer on infrared nanoantennas*. Nano Letters, 2015. **15**(8): p. 5382-5387.
7. Clavero, C., *Plasmon-induced hot-electron generation at nanoparticle/metal-oxide interfaces for photovoltaic and photocatalytic devices*. Nature Photonics, 2014. **8**(2): p. 95-103.
8. Guzatov, D.V., et al., *Plasmonic enhancement of molecular fluorescence near silver nanoparticles: theory, modeling, and experiment*. Journal of Physical Chemistry C, 2012. **116**(19): p. 10723-10733.

9. Klimov, V.V., *Nanoplasmonics*. 2014, Singapore: Pan Stanford Publishing. xiv., 581 pages.
10. Chen, S., et al., *How to light special hot spots in multiparticle-film configurations*. ACS Nano, 2015. **10**(1): p. 581-587.
11. Li, J.-F., C.-Y. Li, and R.F. Aroca, *Plasmon-enhanced fluorescence spectroscopy*. Chemical Society Reviews, 2017. **46**(13): p. 3962-3979.
12. Moskovits, M. and D.H. Jeong, *Engineering nanostructures for giant optical fields*. Chemical Physics Letters, 2004. **397**(1-3): p. 91-95.
13. Mishra, H., et al., *Experimental and theoretical study of the distance dependence of metal-enhanced fluorescence, phosphorescence and delayed fluorescence in a single system*. Physical Chemistry Chemical Physics, 2013. **15**(45).
14. Bergfield, J.P. and M.A. Ratner, *Forty years of molecular electronics: Non-equilibrium heat and charge transport at the nanoscale*. physica status solidi (b), 2013. **250**(11): p. 2249-2266.
15. Cahill, D.G., et al., *Nanoscale thermal transport*. Journal of Applied Physics, 2003. **93**(2): p. 793-818.
16. Chen, G., *Phonon heat conduction in nanostructures*. International Journal of Thermal Sciences, 2000. **39**(4): p. 471-480.
17. Maldovan, M., *Transition between ballistic and diffusive heat transport regimes in silicon materials*. Applied Physics Letters, 2012. **101**(11).
18. Segal, D., A. Nitzan, and P. Hänggi, *Thermal conductance through molecular wires*. The Journal of Chemical Physics, 2003. **119**(13): p. 6840-6855.

19. Segal, D. and B.K. Agarwalla, *Vibrational Heat Transport in Molecular Junctions*. Annual Review of Physical Chemistry, 2016. **67**(1): p. 185-209.
20. Markussen, T., *Phonon interference effects in molecular junctions*. Journal of Chemical Physics, 2013. **139**(24).
21. Solomon, G.C., et al., *Understanding quantum interference in coherent molecular conduction*. Journal of Chemical Physics, 2008. **129**(5).
22. Markussen, T., R. Stadler, and K.S. Thygesen, *The relation between structure and quantum interference in single molecule junctions*. Nano Letters, 2010. **10**(10): p. 4260-4265.
23. Sautet, P. and C. Joachim, *Electronic interference produced by a benzene embedded in a polyacetylene chain*. Chemical Physics Letters, 1988. **153**(6): p. 511-516.
24. Solomon, G.C., et al., *Exploring local currents in molecular junctions*. Nature Chemistry, 2010. **2**(3): p. 223-228.
25. Fermi, E., *Nuclear physics: a course given by Enrico Fermi at the University of Chicago*. 1950: University of Chicago Press.
26. Marcus, R.A., *On the Theory of oxidation-reduction reactions involving electron transfer. I*. Journal of Chemical Physics, 1956. **24**(5): p. 966-978.
27. Marcus, R.A., *Chemical and electrochemical electron-transfer theory*. Annual Review of Physical Chemistry, 1964. **15**(1): p. 155-196.
28. Libby, W.F., *Theory of electron exchange reactions in aqueous solution*. Journal of Physical Chemistry, 1952. **56**(7): p. 863-868.

29. Jortner, J., *Temperature dependent activation energy for electron transfer between biological molecules*. Journal of Chemical Physics, 1976. **64**(12): p. 4860-4867.
30. Balzani, V., *Electron transfer in chemistry*. 2001.
31. Gray, H.B. and J.R. Winkler, *Long-range electron transfer*. Proceedings of the National Academy of Sciences, 2005. **102**(10): p. 3534-3539.
32. Winkler, J.R. and H.B. Gray, *Long-range electron tunneling*. Journal of the American Chemical Society, 2014. **136**(8): p. 2930-2939.

Chapter 2. Experimental methodology

In this thesis, time-resolved femtosecond pump-probe spectroscopy was used as the major tool to study the excited state dynamics of different molecular systems. In addition, we combined computational simulations such as molecular orbital calculations and molecular dynamics simulations to obtain comprehensive understanding behind spectroscopic behavior. Other tools such as steady state absorption spectroscopy and single molecular fluorescence microscopy were also used in the projects described in this thesis to gain insights of these molecular systems from multiple points of views.

2.1 Pump-probe spectroscopy

The development of ultrafast laser and spectroscopy has enabled researchers to study photo-physical processes such as vibrational relaxation and charge transfer that fall in the range of picosecond or even femtosecond time scales. Among many implementations of ultrafast laser spectroscopy, pump-probe spectroscopy is one of the widely used techniques in the field of laser spectroscopy.

A pump beam is used to excite the sample to higher electronic states and a probe beam (white light continuum) spatially overlapping with the pump detects the absorption change of variable delay times. Two pump-probe spectroscopy set-ups were used in the context of this work. One relied on a home build multi-pass amplifier and lock-in detection. The other one is a commercially available instrument with regenerative amplification and photodiode array detection [1].

2.1.1 Transient absorption system 1

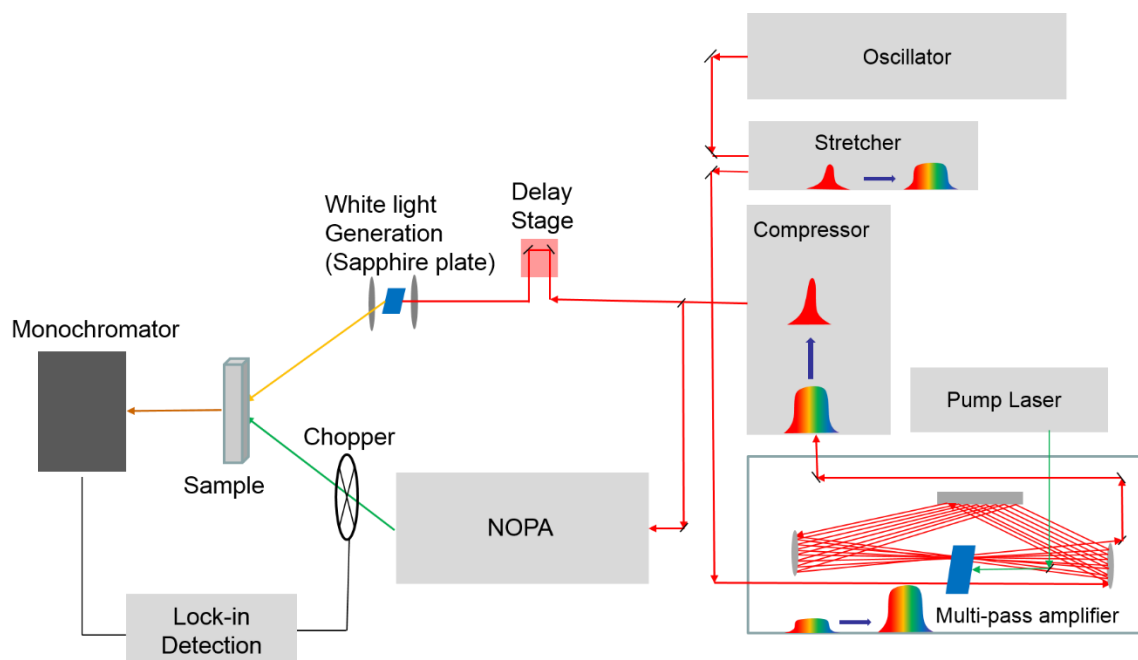


Figure 2.1 Scheme of the pump-probe set-up using multi-pass amplifier and lock-in detection.

A pulsed laser beam (70 fs, 795 nm) was produced by a mode-locked Ti-sapphire oscillator (Spectra-Physics Tsunami) and was amplified by a home-built 1.25 kHz multipass amplifier. The output of the amplifier was split into two stream of pulses. One of these was converted to white-light continuum in a 2 mm sapphire plate and used as the tunable probe. The other was used to drive a noncollinear optical parametric amplifier (NOPA, Topas White, Light Conversion) and used as the pump beam (525 nm, 120 μ W). The pump pulses were delayed with respect to the probe by a computer-controlled translation stage. The pump and probe beams were spatially overlapped on the sample films. The pump was modulated with a mechanical chopper at 50 Hz and the resulting signal was recorded by a

computer controlled digital lock-in amplifier (Stanford Research, SR810), with a monochromator (Oriel MS257) scanning the desired probe wavelength.

2.1.2 Transient absorption system 2

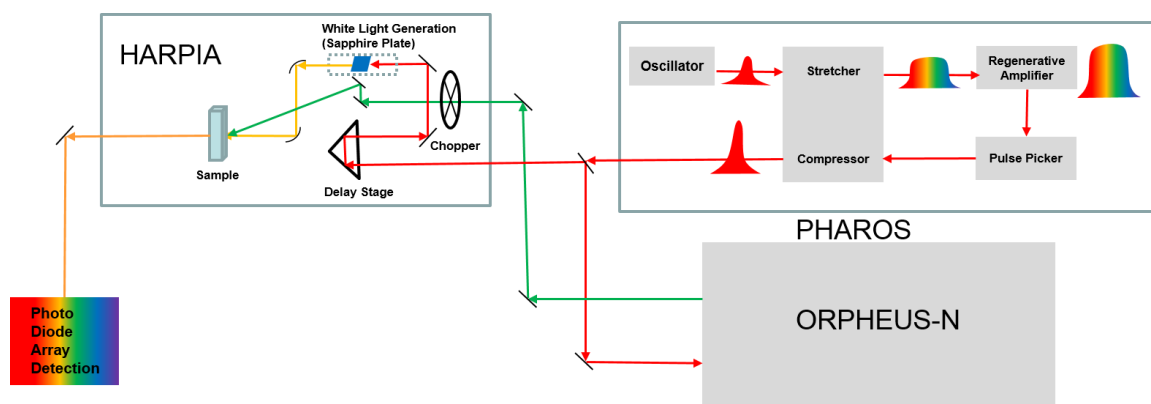


Figure 2.2 Scheme of the pump-probe set-up using regenerative amplifier and photodiode array detection.

In this case, 177 fs, 1030 nm pulsed output was generated by an integrated femtosecond laser system with variable repetition rate (PHAROS, Light Conversion). The output of PHAROS (2 kHz) was split into two pulses, one was used to pump a non-collinear optical parametric amplifier (ORPHEUS-N 3H) containing a third harmonic generator to deliver a pump beam at 550 nm which was modulated with a mechanical chopper at 50 Hz. The other stream of pulses was directed into an ultrafast spectroscopic system (HARPIA-TA) to generate white light continuum as the probe beam, which was spatially overlapped with the pump pulse at sample. A photodiode array and a monochromator were used to detect signal.

2.2 Computational simulations

In addition to experimental measurements, two types of computational simulations were applied in this thesis: molecular orbital calculations and molecular dynamics simulations.

2.2.1 Molecular orbital calculations

There are several widely used approaches in computational chemistry to calculate molecular energies and orbitals. Among all, density functional theory (DFT) is most popular due to its low-cost in computational effort and accuracy. DFT calculation falls in the category of quantum mechanical methods that treat molecules as collections of nuclei and electrons and solve Schrödinger equations in terms of motions of electrons. Since the Schrödinger equations can only be solved analytically for one-electron systems, several approximations are needed to simplify the calculations for multi-electron molecules. In DFT, the molecular energy is expressed in one-electron density instead of a wave function and the ground state energy of the system depends uniquely on the electron density according to the Hohenberg-Kohn Theorems. The key problem left is to employ the proper exchange/correlation functions. In local density models, functionals based on the local spin density approximation are used, where the energy is assumed to depend locally on the density in the same way it does for a uniform electron gas. In gradient-correlation models, the functionals based on generalized gradient approximations or the “exact” Hartree-Fock exchange are employed. The results obtained by DFT are dependent on these exchange/correlation functionals and better forms of functionals are still being developed [3]. In the context of this work, all molecular orbital calculations were carried out by the commercially available software package Spartan 16 using DFT at B3LYP/6-31G* level.

2.2.2 Molecular dynamics simulations

Classic molecular dynamics (MD) is a popular tool to simulate the motions and interactions of a collection of atoms or molecules. The basic machinery behind it is Newton's second law that states:

$$F_i = m_i a_i; a_i = \frac{d^2 x_i}{dt^2} \quad (2.1)$$

Where m_i , a_i and x_i represent mass, acceleration and position of atom i . The calculated potential energy surfaces are dependent on the force fields. Force fields are sets of functions and parameters extracted from either ab initio calculations or experimental data. Some commonly used force fields in MD simulations include AMBER, CHARMM OPLS-AA and so on. The subsequent time evolution of atom i can also be monitored and recorded as trajectories. Despite the convenience and insightful results classical MD gives, there are several major limitations of this method that should not be neglected. First of all, the use of classical forces automatically neglects the quantum nature of atoms. This limitation is especially pronounced when simulating very light systems such as H_2 and in low temperature regime. Second, even though more advanced force fields are being used in MD simulations and the agreement between experimental results and MD is getting better, there is always a deviation from reality. Lastly, MD is insufficient in simulating very large system and slow processes (microsecond to millisecond time scale). This is quite often the case for proteins and polymers. Nevertheless, MD simulations are able to provide highly useful insights into the behavior of beyond what experiments alone can accomplish [4].

In this thesis, we took the advantage of MD simulations and applied the tool in a series of oligomeric viologens. The simulations were carried out using commercial software

YASARA with AMBER 14 force field under no pressure and temperature controls both in vacuum and in solvents.

2.3 Single molecule fluorescence spectroscopy

In contrast to bulk measurements, single molecule experiments allow the investigation of the behavior for individual molecules. Single molecule fluorescence microscopy is used in Chapter 3 and the fluorescence for single strand P3HT on both gold nanorod substrate and cover glass was recorded. The experiments were carried out in Dr. Martin Vacha's laboratory in Tokyo Institute of Technology.

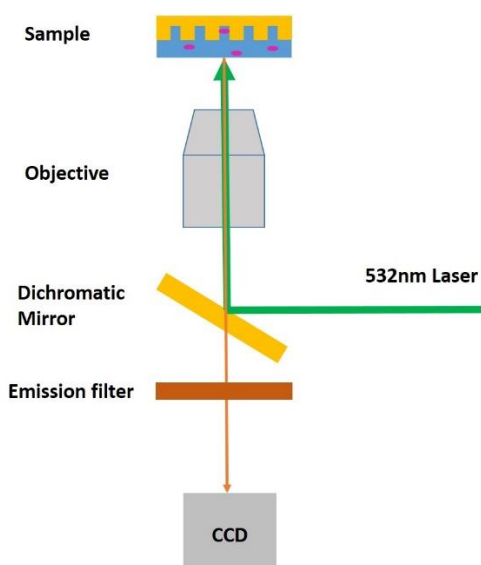


Figure 2.3 Scheme of the single molecule fluorescence microscope.

The set-up used in this work consists of an inverted wide-field microscope (Olympus IX 71). The sample was excited by a cw solid-state laser (TDG532-500, Changchun New Industries Optoelectronics Tech., 532 nm, 200 μ W). Emission from the sample was collected by a dry objective lens (UMPlanFL100x, N.A. 0.95, Olympus). The fluorescence imaging was carried out in an epi-fluorescence mode with a dichroic mirror (Di02-R532,

Semrock) and a long-pass filter (BLP01-532R, Semrock). The images were detected with an electron-multiplying (EM) CCD camera (iXon, Andor) with bin time of 0.1 s. Single-molecule fluorescence spectra were measured using an imaging spectrograph (Bunkou Keiki CLP-50, 0.5 nm resolution) inserted between the microscope and the EM-CCD camera.

2.4 Steady state spectroscopy and others

All UV-Visible absorption spectra were collected using a Cary 5000 UV-Vis-NIR spectrometer. For samples in solution, 1 cm quartz cuvette was used. Baselines were subtracted for solvents and empty cuvette.

All fluorescence measurements were collected using a Cary Eclipse fluorescence spectrometer. For samples in solution, 1 cm quartz cuvette was used. Baselines were subtracted for solvents and empty cuvette. The excitation wavelengths were selected depending on the target material monitored.

All other sample preparation procedures will be discussed in detail in the individual chapters.

References

1. Reid, G.D. and K. Wynne, *Ultrafast laser technology and spectroscopy*, *Encyclopedia of Analytical Chemistry*. 2006.
2. Jensen, F., *Introduction to computational chemistry*. 2nd ed. 2007, Chichester, England ; Hoboken, NJ: John Wiley & Sons. xx, 599 p.
3. Hehre, Warren J. *A guide to molecular mechanics and quantum chemical calculations*. Vol. 2. Irvine, CA: Wavefunction, 2003.
4. Ercolessi, F., *A molecular dynamics primer*. Spring college in computational physics, ICTP, Trieste, 1997. **19**.

Chapter 3. Excited state behavior of single strand and bulk

P3HT in contact with an Au nanowire array

In this chapter, the multifaceted influence of hexagonally packed Au nanowires on the excited state behavior of closely located regioregular (RR) P3HT both in bulk form and single strands is studied by pump-probe spectroscopy and single molecule fluorescence spectroscopy.

An average 5-fold increase of fluorescence intensity was detected for single strands of P3HT in the presence of the nanowire array, with the strongest emitters exceeding the brightness of their counterparts on glass by a factor of 40. The single molecule trajectories show that the same polymer strand is capable of exhibiting a wide range of enhancement levels. The “off” periods on the Au substrate are exceptionally long and erratic. This behavior is attributed to sporadic electron transfer events between the strand and the metal. Bulk P3HT deposited on the same Au nanowire array shows a dramatic reduction of the yield and lifetime of singlet excitons in comparison with glass support, indicating that the proximity of the metal greatly accelerates both exciton dissociation and charge recombination. Interestingly, a large increase of the triplet exciton population is observed in the presence of the metal, indicating a much faster loss of the spin-spin correlation. The bulk P3HT results suggest that the large fluorescence enhancement observed in the single molecule experiments occurs only for a few emitters which have been fortuitously placed at the optimum distance and orientation with respect to the metal.

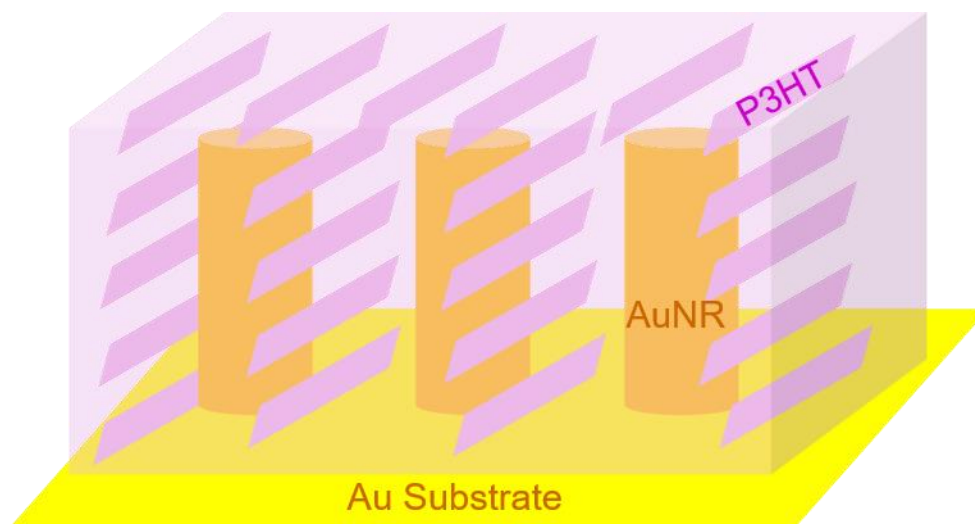


Figure 3.1 Schematic representation of P3HT@AuNR.

3.1 Introduction

As described in Chapter 1, the proximity of a metal surface can dramatically alter the radiative and nonradiative decay pathways and the corresponding lifetimes, τ_{rad} and τ_{nr} of the excited state of a molecular or polymeric emitter, especially when the metallic substrates exhibit localized surface plasmon resonance (LSPR). In such systems, the competing short and long-distance interactions contribute to the overall response which can range from substantial enhancement to total quenching of the intrinsic photoluminescence [1-4]. In this work, we report the behavior of regioregular polyhexylthiophene (RR-P3HT), both in the form of a bulk film and dispersed at a single molecule level, coupled to a dense array of 60 nm long hexagonally packed Au nanorods (NRs) with a pitch of 29 nm and diameter of 12 nm (Figure 3.1), which we prepared with the help of a unique bottom-up wet chemistry methodology [5]. Because of the high Au nanorod content ($\sim 30\%$ by volume) and the correspondingly large polymer-metal contact area, the photoresponse of the P3HT@AuNR system is expected to be determined to a

large degree by the interactions at the interface and to differ sharply from the reference in which a layer of P3HT has been deposited on a chemically and optically inert glass substrate (**P3HT@glass**).

3.1.1 Properties of RR-P3HT

Poly (3-hexylthiophene) is one of the most frequently used semiconducting polymers in the field of organic electronics [6, 7]. Depending on the sequence of 2-(head) and 5-(tail) positions in the two adjacent thiophene rings when coupled, P3HT shows different regiochemistry shown in Figure 3.2. Regioregular P3HT contains only head to tail (HT) coupling thus exhibiting planar conformation and extended π conjugation, which makes it perfect for applications in charge transport. On the other hand, in regiorandom (RRa) P3HT, the coupling between two thiophene rings is irregular (HH or TT). Therefore, the conformation deviates from being planar and shortens the conjugation length [8].

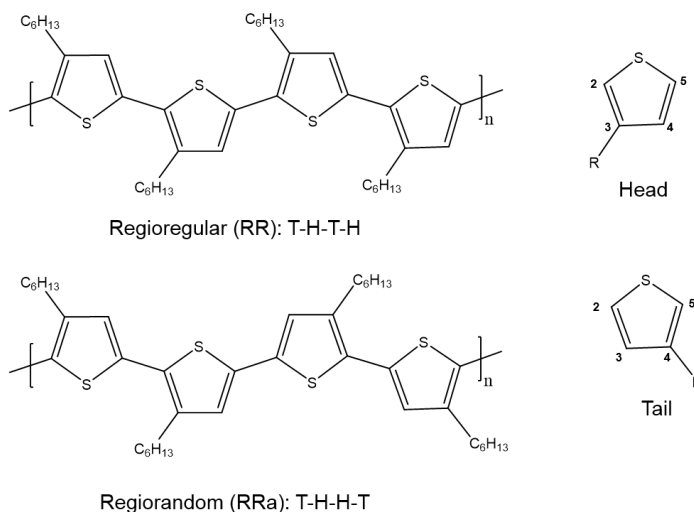


Figure 3.2 Structure of RR-P3HT and RRa-P3HT.

Regioregular P3HT is not conductive in neutral state and becomes conductive upon doping. The energy levels for P3HT can be determined by cyclic voltammetry (CV) and calibrated to the HOMO and LUMO levels in Fermi energy scale using the following equations,

$$E_{HOMO} = - \left(E_{(ox,vs.Fc^+/Fc)} + 5.1 \right) eV \quad (5.1)$$

$$E_{LUMO} = - \left(E_{(red,vs.Fc^+/Fc)} + 5.1 \right) eV$$

which yield -5.12 eV -2.84 eV for HOMO and LUMO in RR-P3HT [9].

RR-P3HT is readily soluble in many solvents and exhibits broad, featureless absorption that is dominated by isolated polymer chains. In thin films, RR-P3HT can form highly crystalline layers. The morphology is strongly affected by molecular weight of the RR-P3HT used and the processing conditions such as the deposition protocols (spin coating, drop casting etc.). In this work, we prepared RR-P3HT solution in toluene, a relatively fast evaporating solvent, and applied drop-casting technique to fabricate RR-P3HT thin films on both AuNR and glass substrates. The packing of such RR-P3HT film is edge-on, which is generally favored thermodynamically in comparison to the other, face-on packing which is more favored in P3HT with lower regioregularity [8].

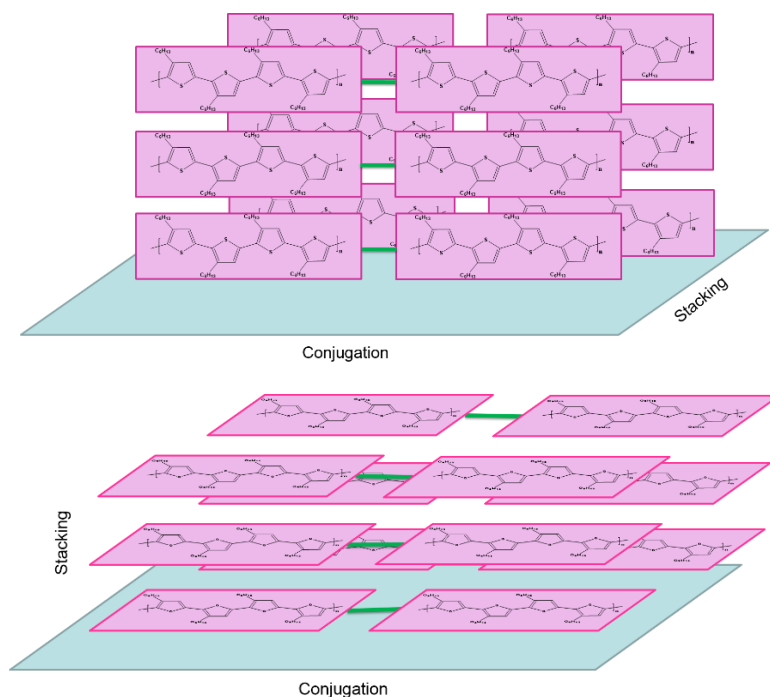


Figure 3.3 Edge-on and face-on packing of crystalline RR-P3HT.

3.1.2 Charge carrier generation in P3HT@AuNR

One of the unique properties of semiconductors is the generation of charge carriers upon photo-excitation. These charge carriers play central roles in the optical performance of conjugated polymers [10]. Singlet excitons and polaron pairs, electron-hole pairs bound by Coulomb interaction, are generated at the initial stage of photon excitation. There are two types of excitons: Mott-Wannier and Frenkel excitons. Mott-Wannier excitons are generated in materials with large dielectric constants which give rise to larger exciton radii and hence smaller binding energies (<0.01 eV). On the other hand, Frenkel excitons are generally more compact with larger binding energies (0.1-1 eV) and are formed in materials with lower dielectric constant. Excitons are not static, they tend to delocalize within delocalization radius and overcome the binding within the electron-hole pair to dissociate. When excitons dissociate, polarons, free moving electrons and holes, are

generated. The mechanism of dissociation is frequently described by the hot-exciton dissociation model, in which the excess energy carried by excitation photon leads to lattice phonon excitation and can be used to break the binding within the electron-hole pair. As a result, the yield of polarons and polaron pairs often exhibits pronounced dependence on the energy of the absorbed photon [11-13].

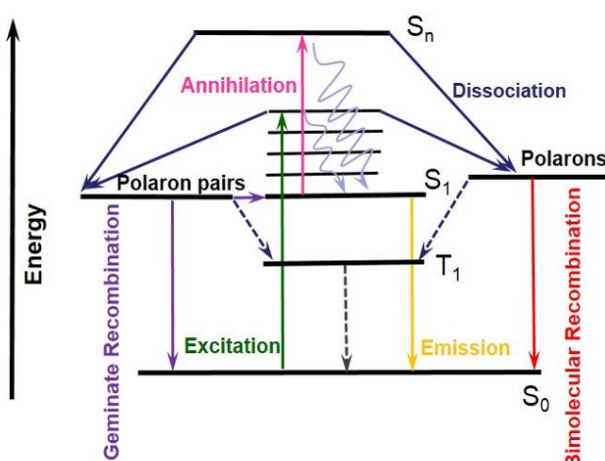


Figure 3.4 Competing radiative and non-radiative processes in a polymeric material.

In **P3HT@AuNR**, exoergic tunneling of electrons and holes between the photoexcited P3HT and the AuNR is possible. For excitons generated sufficiently close to the metal surface, excess excitation is therefore unnecessary in order to overcome the electron-hole binding. Free moving polarons generated by dissociation can follow a number of possible dynamic pathways such as diffusion, recombination, electron transfer or tunneling. In our case of **P3HT@AuNR**, the polarons are not only able to recombine with their charged counterparts in the polymer but can also rapidly recombine with electrons or holes tunneling from gold in the reverse direction. The image charges generated in the metal are likely to further accelerate the rapid electron exchange and charge recombination at the interface. Due to the dense continuum of energy states in gold, the electron or hole can

always find a matching final electronic state to which the transfer is thermodynamically favored. It has been shown that photoinduced electron transfer from chromophores anchored to metallic surfaces can be as fast as 10 fs [14].

Because electron tunneling is highly distance dependent, the initial behavior of the excitons formed further away from the interface should resemble these in **P3HT@glass**. As the distance to the Au surface increases, the transition from the “direct contact” to the “bulk-like” excited state behavior of in **P3HT@AuNR** is likely to be steep but gradual. Nevertheless, it is convenient to divide the area around the Au nanorods into two distinct zones defined by the delocalization length of the exciton (Figure 3.5 Right). The zone which lies within the delocalization length from the surface of the nanorod (light pink) defines the volume of strong interaction between the components of the photoexcited assembly. The area which extends further than the delocalization length (dark pink) corresponds to the volume where the initial behavior of the exciton is expected to be similar to pristine bulk P3HT. This simplified picture will be used to interpret the results of both the bulk and single molecule measurements on the nanostructured Au substrate.

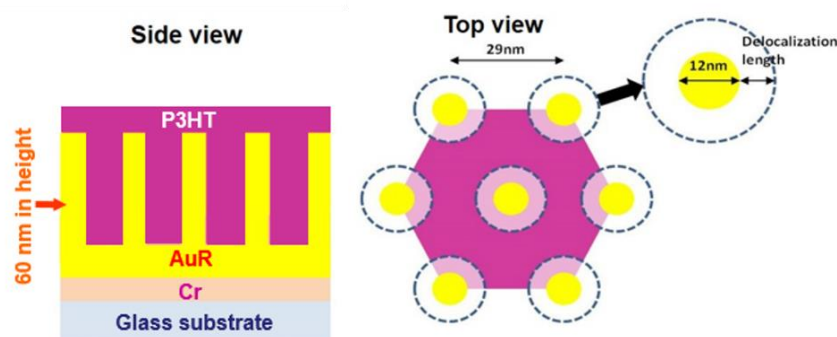


Figure 3.5 (Left) Schematic representation of the nanowire array filled with P3HT.

The side view of P3HT@AuNR is shown on the left, a horizontal slice on the right.

(Right) Top view of the Au-nanowire array with two-zone division.

In this chapter, we will demonstrate that when coupled to AuNR, not only the dynamics of existing charged carriers in RR-P3HT (singlet excitons, polaron pairs and polarons) is severely altered, there is also evidence of formation of triplet excitons, which are usually absent in RR-P3HT and only appears in RRa-P3HT.

3.2 Sample preparation

Gold nanorod array films: Au nanorod array substrates were fabricated using block copolymer templated electroplating method, which was modified from the fabrication methods of CeO_x and conducting polymer nanorod arrays [5, 15]. An electrode was prepared by sputtering Cr and Au on a cover glass. A 3% toluene solution of liquid crystalline block copolymer PEO₁₁₄-*b*-PMA(Az)₆₆ was spin-coated on the Au/Cr-sputtered glass electrode. The coated electrode was thermally annealed in vacuum for 6 h at 140°C to form vertically oriented cylindrical PEO domains surrounded by liquid crystalline PMA(Az) domains. Electroplating was performed in 1 mM HAuCl₄ aqueous solution by using a potentiostat/galvanostat (Ivium CompactStat, Ivium Technologies, Netherlands) with potential scanning method in a range between -1.0 V and 0.5 V vs. Ag/AgCl. The template was removed from the electrode by oxygen ion etching (Shinko Seiki, Japan) with a radio frequency power of 50 W at a pressure of 15 Pa for 140 s [5].

Samples: For pump-probe measurements regioregular (RR) P3HT (Sigma Aldrich, Mw 55k) was dissolved in toluene (Sigma Aldrich) to make a solution of 0.12 mg/ml and drop

cast on the cover glass and Au nanorod arrays. For single molecule measurements the regioregular (RR) P3HT was dissolved in PMMA (3% weight in toluene) to make a solution of approximately 3×10^{-8} molar and spin-coated on the cover glass substrates and gold nanorod arrays at 3000 rpm for 30 s.

3.3 Results and discussion

The electronic spectrum of **P3HT@AuNR** exhibits relatively minor non-additive effects. Only at short wavelengths (350–450 nm), the spectra on glass and on AuNR significantly diverge. As the difference spectrum $\Delta A = A_{\text{P3HT@AuNR}} - A_{\text{AuNR}}$ shows, the main features of the P3HT band in the ~500-650 nm range are retained (Figure 3.6). The altered intensity of the vibronic peaks and slight broadening are evident but not dramatic. This suggests that the packing of the P3HT strands on the AuNR substrate is similar to that on glass and that the average electronic interaction between the metal and the polymer is modest. A strong interaction with the substrate is likely manifest itself in the form of major changes of the absorption spectrum of the molecular component, such as the appearance of charge transfer transitions at the interface [16-19]. Furthermore, the magnitude of the $\Delta A = A_{\text{P3HT@AuNR}} - A_{\text{AuNR}}$ absorbance difference suggest that the **P3HT@AuNR** samples contain only a 20-30% more P3HT than the amount needed to fill the voids of the nanorod array. As a result, transient spectra discussed below originate primarily from P3HT embedded between the Au nanorods with a smaller contribution from a layer deposited on top of the array.

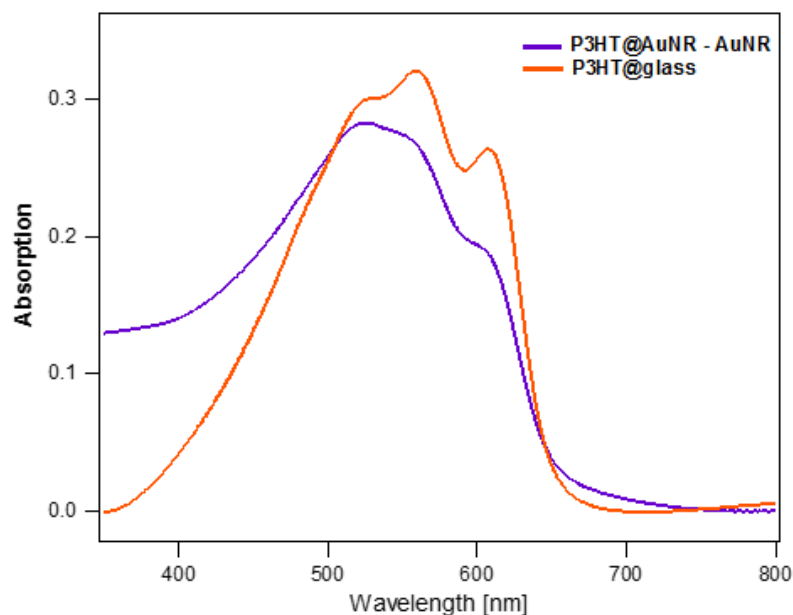


Figure 3.6 Absorption spectrum of P3HT@glass and the difference spectrum

$\Delta A = A_{\text{P3HT@AuNR}} - A_{\text{AuNR}}$. All spectra were collected at normal incidence.

3.3.1 Pump-probe measurement

The selected pump wavelength of 525 nm coincides with the third vibronic feature of **P3HT@glass** and the maximum of the $A_{\text{P3HT@AuNR}} - A_{\text{AuNR}}$ difference spectrum (Figure 3.6). While selective excitation of the P3HT component in the **P3HT@AuNR** assembly is impossible, this wavelength maximizes the fraction of photons absorbed by the polymer rather than the substrate. Unambiguous assignment of all spectral features of photoexcited bulk P3HT to all plausible excitonic and polaronic species is not trivial, as evidenced by the large and not always consistent literature [8, 20, 21]. The challenge is well illustrated by the calculated spectra of the hole, excess electron, T_1 , S_1 and S_0 states of short strands of P3HT (Figure 3.7). The evident spectral congestion becomes even more complex in bulk P3HT, where the strands interact with one another and a wide distribution of conformations modulates the delocalization length of the excitons and charge carriers. As a result, the

same species, e.g. a polaron or an exciton may exhibit a broad range of absorption wavelengths depending on the length of the unperturbed segment. In the interpretation of our results we followed the spectral assignments of Guo, Ohkita et al.[22], which we find particularly thorough and consistent.

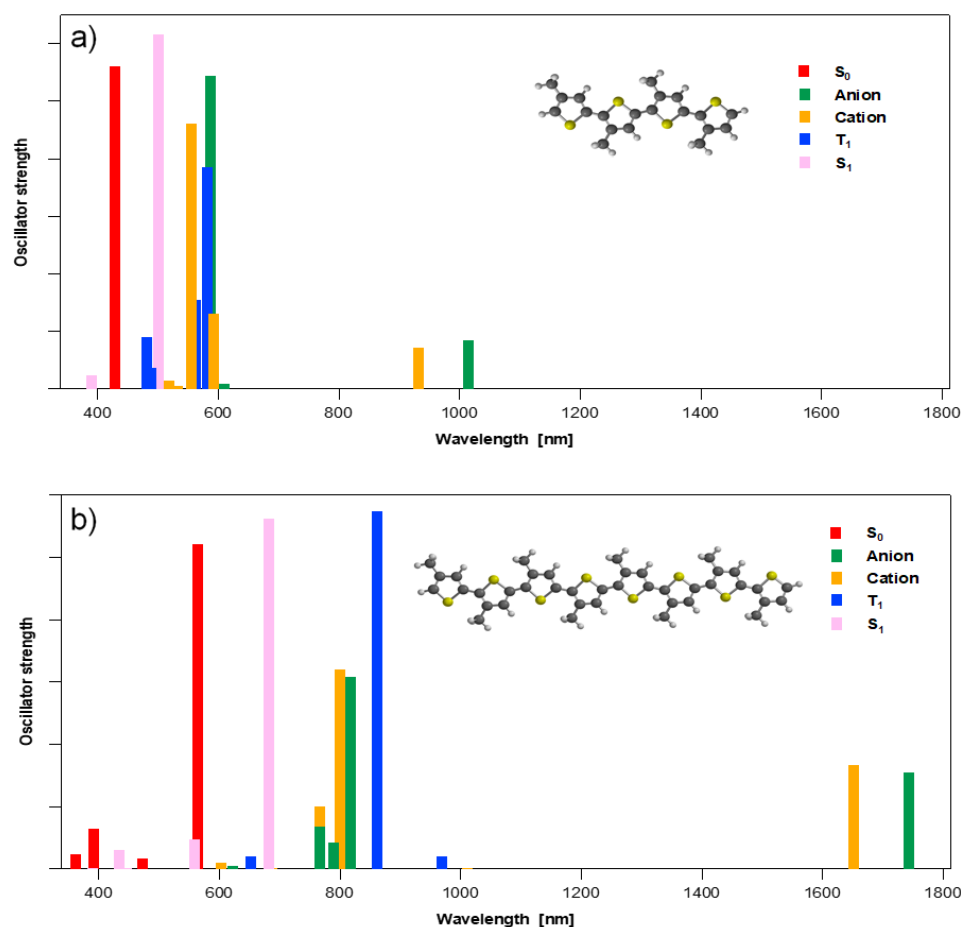


Figure 3.7 Computed positions and intensities of low-lying electronic transitions of the S_0 , S_1 and T_1 states, as well the radical cation and radical anion of a regioregular tetramer (a) and octamer (b) of 3-methylthiophene. The DFT (B3LYP, 6-31G*) calculations were carried out using Spartan'16 by Wavefunction, Inc.

As expected, the excited state spectra of **P3HT@glass** and **P3HT@AuNR** differ markedly from one another, especially in the near IR (Figure 3.8). **P3HT@glass** shows a very broad

absorption band the intensity of which steadily rises from 800 to the 1100 nm limit of our measurements (Figure 3.8a). Its maximum lies further in the near IR and is consistent with the 1250 nm band assigned by Guo et al to the singlet excitons. This prominent band is almost completely absent in **P3HT@AuNR**, however, a new peak at 800-850 nm appears along with another, weak and broad feature with a poorly defined maximum at ~900 nm (Figure 3.8b). The disappearance of the 1250 nm band indicates an extremely rapid consumption of singlet excitons in **P3HT@AuNR**. The most likely dominant decay mechanisms are exciton dissociation via electron exchange at the polymer-metal interface and energy transfer. These processes appear to be faster than sub 100 fs time resolution of our measurements.

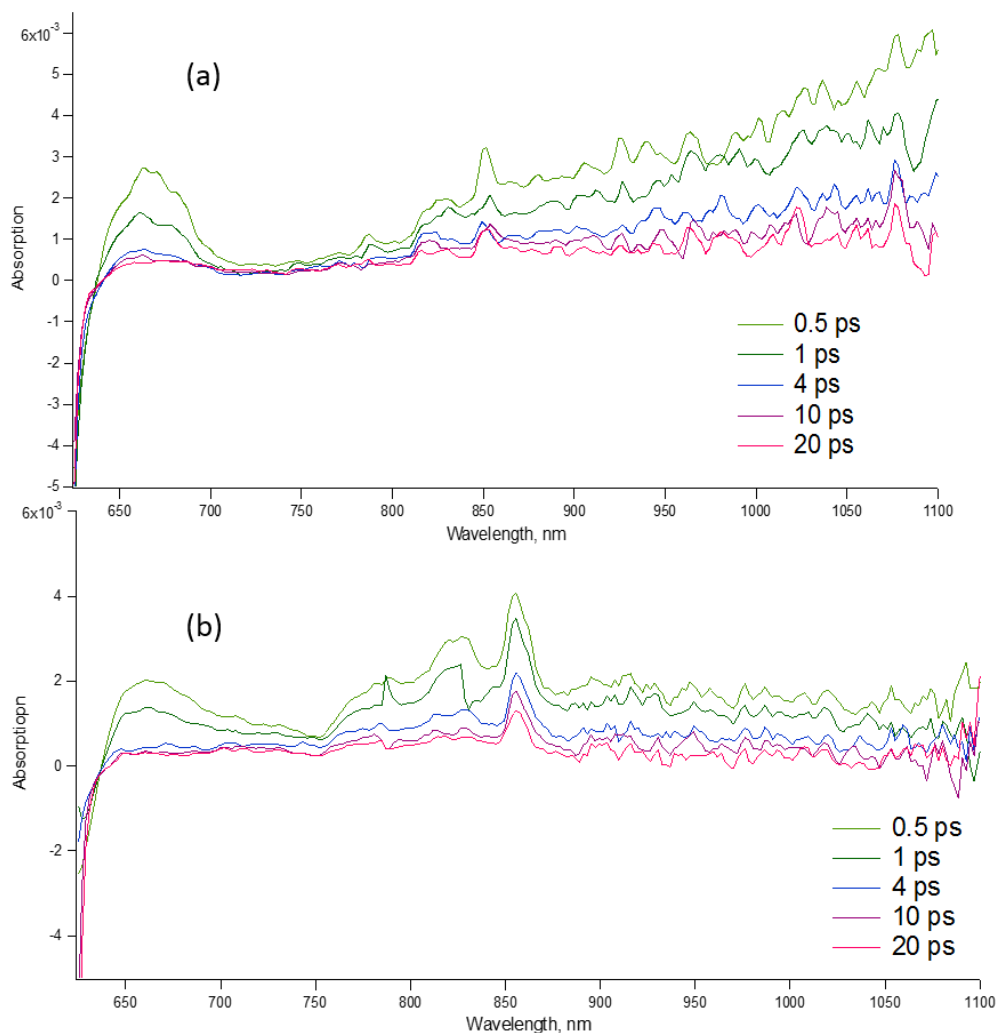


Figure 3.8 Transient absorption spectra of (a) P3HT@glass; (b) P3HT@AuNR. Data collected under 525 nm excitation at different delay times.

The strong peak at 800-850 nm is consistent with triplet excitons in RRa-P3HT [22, 23] and represents one of the most interesting findings of this project. The triplet population generated in pristine RR-P3HT is usually negligibly small because the formation of polarons and polaron pairs is faster than the intersystem crossing (ISC). In regiorandom (RRa) P3HT, the observation of triplets upon excitation well above the bandgap ($h\nu \approx 2 \cdot E_b$), has led some to propose that singlet fission may be involved [22]. In **P3HT@AuNR**, the

proximity of the metal opens new channels of triplet formation, regardless of the energy of the pump photons (in our case ~ 2.4 vs the ~ 2.0 eV bandgap). Firstly, the rapid, $\tau < 100$ fs, electron exchange at the metal-polymer interface, leads to a similarly fast loss of the spin-spin correlation between the electron and the hole (the spin polarization of an electron in a metal is lost essentially instantaneously). Subsequent charge recombination of the uncorrelated spins to the T_1 state is statistically three times as probable as the recombination to the S_0 ground state. The endoergic recombination to the S_1 state is too slow to be relevant. Furthermore, the moderately exoergic formation of the T_1 state ($\Delta G_0 \approx -0.4$ eV) is kinetically favored over the recombination directly to the S_0 state, which lies deep in the Marcus inverted region ($\Delta G_0 \approx -2.0$ eV). Acceleration of the intersystem crossing in the original S_1 singlet exciton by plasmonic field effects is also possible. Examples of such enhanced ISC and phosphorescence can be found in the literature [24-26]. Unlike the short range electron exchange, which is limited to a thin layer adjacent to the metal, the field effects extend for tens of nanometers and could modulate the ISC rate across the entire **P3HT@AuNR** sample. This is a very appealing possibility, however, the reported acceleration of the ISC and phosphorescence is small, with the highest measured plasmonic enhancement factor of 2.4 [27], which is much too low to account for the formation of the P3HT triplet on a subpicosecond timescale. As a result, if such effects are present in **P3HT@AuNR**, they are most likely of secondary importance.

The weak band at $\sim 900 - 1000$ nm in Figure 3.8b belongs to free polarons (the spectra of electrons and holes are nearly identical in P3HT). Upon closer inspection, this feature is also seen in the spectrum of **P3HT@glass** (Figure 3.8a), where it appears as a broad shoulder on the high energy side of the 1250 nm exciton band. Both in **P3HT@glass** and

P3HT@AuNR, there is strong stimulated emission overlaid with the bleach of the ground state at wavelengths shorter than 650 nm and a well-defined band at 660 - 670 nm which belongs to the polaron pairs. In **P3HT@AuNR**, this band exhibits a broad low-energy shoulder extending to 750 nm. This feature is consistent with the spectrum of polaron pairs in RRa-P3HT [22] and may indicate increased conformational disorder in the presence of the Au nanowires.

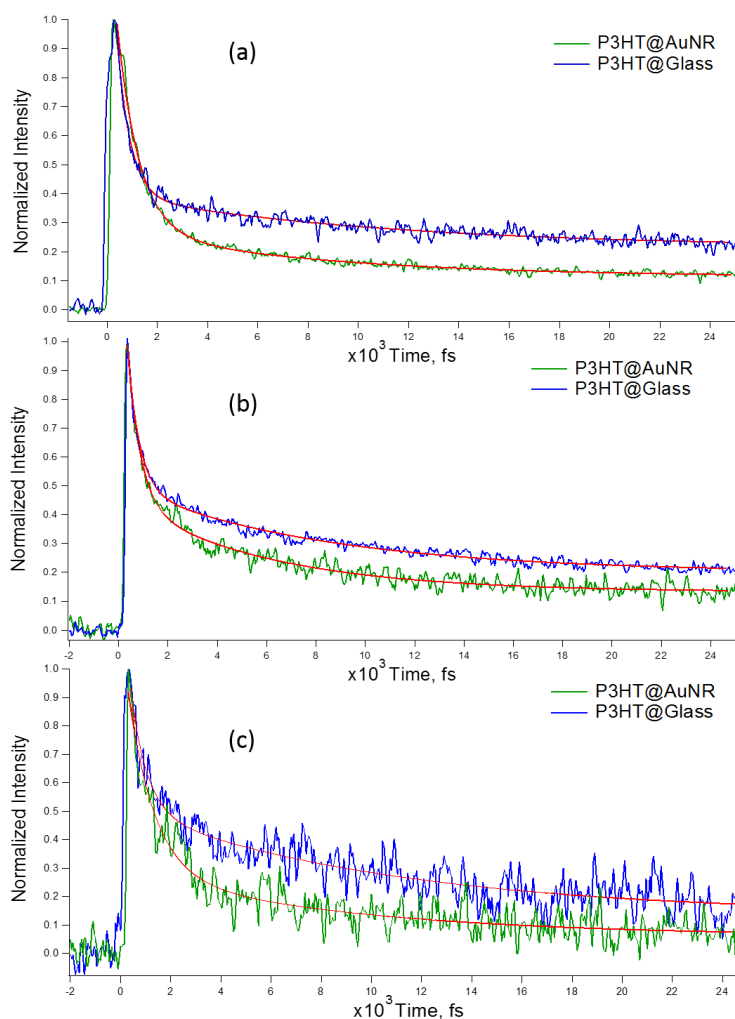


Figure 3.9 Normalized transient absorption decay profiles and the fits (red) obtained for **P3HT@glass** (blue) and **P3HT@AuNR** (green) at probe wavelengths of: (a) 668 nm; (b) 876 nm; (c) 1032 nm.

In order to better understand the dynamic behavior of the system, time profiles were collected at 668 nm (polaron pairs), 876 nm (triplet excitons and free polarons) and 1032 nm (singlet excitons and free polarons). A double exponential function $\Delta A(t) = A_1 \cdot \exp(-t/\tau_1) + A_2 \cdot \exp(-t/\tau_2) + A_\infty$ was used to fit the decay curves shown in Figure 3.9. The evolution of the interconverting transient species in P3HT does not follow first order kinetics but double [24] or triple [18-19] exponential fitting is a frequent compromise used to analyze the temporal response in systems exhibiting complex multi-order kinetics. When comparing the results presented here with these of Guo, Ohkita et al. [22] and Hwang et al. [23], it should be noted that the pump pulses employed in our experiments were 3 to 4 times shorter, and the overall time resolution ~2-times better. Consequently, the sensitivity to the fastest components of the decay was considerably higher.

	τ_1 (ps)	A_1	τ_2 (ps)	A_2	A_∞	ΔA_1	ΔA_2	ΔA_∞
668 nm								
P3HT@glass	0.52±0.02	0.61±0.01	10±1.0	0.18±0.004	0.21±0.006			
P3HT@AuNR	0.86±0.02	0.72±0.01	8.1±0.6	0.16±0.005	0.12±0.003	+18%	-11%	-43%
876 nm								
P3HT@glass	0.47±0.02	0.51±0.01	8.1±0.3	0.29±0.004	0.20±0.003			
P3HT@AuNR	0.52±0.03	0.56±0.02	5.8±0.3	0.31±0.010	0.13±0.003	+10%	+7%	-35%
1032 nm								
P3HT@glass	0.64±0.09	0.47±0.03	11±1.0	0.37±0.013	0.16±0.018			
P3HT@AuNR	1.0±0.01	0.69±0.03	8.9±2.4	0.25±0.025	0.06±0.016	+47%	-32%	-63%

Table 3.1 Double exponential decay fitting parameters for transient dynamics probed at 650, 850 and 1000 nm in **P3HT@AuNR** and **P3HT@Glass**.

Several trends are apparent in the data shown in Figure 3.9 and Table 3.1. Firstly, the amplitude A_∞ which represents the longest lived population of any detected species is lower for **P3HT@AuNR** than for **P3HT@glass** by as much as 35 to 63%. The decrease is most pronounced at 1032 nm where the absorption is dominated by singlet excitons. At 876 nm,

where triplet excitons are the strongest absorbing species, the decrease is smallest. The reduction of A_{∞} is accompanied by a commensurate increase of A_I , the amplitude of the fastest decaying component, $\tau_I \approx 0.5\text{--}1$ ps. In this case the change is also the greatest in the near IR (47%), underscoring the notion that the singlet excitons are most affected by the presence of the Au substrate. The smallest, 10% increase of A_I is observed at 876 nm, once again suggesting the rapidly disappearing singlet excitons and polarons are replaced by the longer lived the triplet excitons. The two-zone model shown in Figure 3.5 is helpful in rationalizing the above observations. Based on the literature value of the exciton radius, 4.3-6.7 nm [22, 28, 29] and the geometric parameters of the nanorod array, the ratio of volume where singlet excitons are in contact with gold to the volume where direct contact is not possible is 6:4 and implies that 60% of the excitons can undergo electron exchange with the metal immediately upon photoexcitation. The ΔA_{∞} of -63% observed for **P3HT@AuNR** at 1032 nm agrees surprisingly well with the estimated interaction volume.

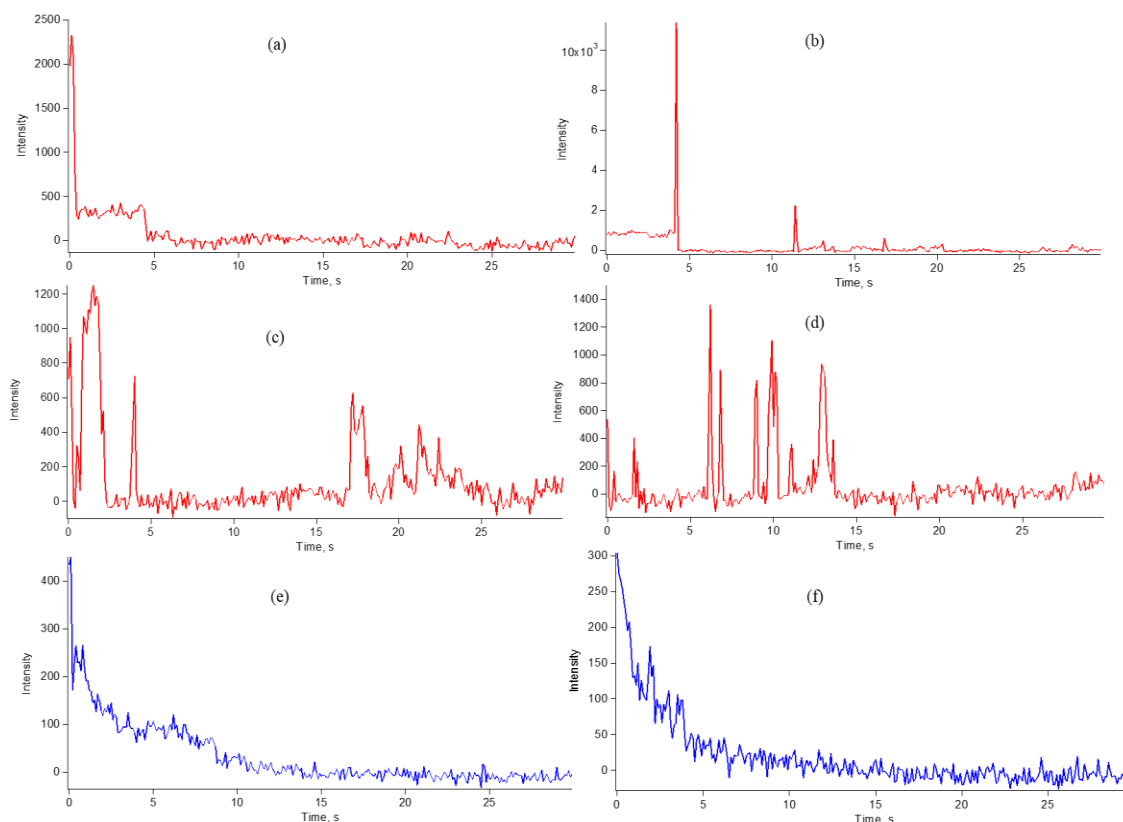


Figure 3.10 Single molecule fluorescence blinking profiles for P3HT embedded in PMMA deposited on the Au-nanorod array (a-d) and on glass (e-f). Each trace shows the photon count of a randomly selected emitter plotted versus time.

3.3.2 Single molecule spectroscopy

Single molecule spectroscopy has been successfully applied to study spatial and dynamic heterogeneity of polymers [30-32], including polythiophene [33-36]. We conducted measurements on single P3HT chains dispersed in a PMMA and deposited on glass (**SMP3HT@glass**) as well as the nanorod array (**SMP3HT@AuNR**). While the spatial resolution of single molecule spectroscopy is not sufficient to resolve the subwavelength features of the Au nanowire array, useful insights about the behavior of P3HT coupled to the metal can be extracted from this data. The most striking feature of the single molecule

trajectories (Figure 3.10) recorded for **SMP3HT@AuNR** is the strikingly broad range of photon counts and the exceptionally erratic pattern of the “on” and “off” states in comparison with the relatively smooth blinking curves and lower intensities of **SMP3HT@glass**. The latter resemble typical trajectories of conjugated polymers in good-solvent matrices [31]. The behavior of **SMP3HT@AuNR** exacerbates the difficulty in identifying a representative set of trajectories, a task which is always challenging in single molecule spectroscopy, even in the case of well-behaved fluorophores. As seen in Figure 3.10, traces 3.10a through 3.10d, the photon count in the “on” state of the bright emitters coupled to Au exceeds the strongest emitters on glass substrate (traces 3.10e and 3.10f) by a wide margin, pointing to the presence of plasmonic enhancement effects. In some instances, e.g. 3.10b, the intensity is 25 to 40-times higher than in the absence of the metal, however, these ultrabright bursts occur only for a brief period and are followed by extended off intervals. More commonly, the enhancement is only ~3 to 8-fold, however, it persists for longer periods of time (traces 3.10c and 3.10d).

Given that the fluorescence quantum yield of P3HT in solution is ~0.3, such high enhancement factors observed upon cw excitation reflect not only the increased quantum yield but also accelerated cycling between the excited state and the ground state (the quantum yield cannot exceed 1, however, the radiative rate can be arbitrarily high). Another feature observed for **SMP3HT@AuNR** is the presence of the abrupt changes in the photon count (traces 3.10a and 3.10b), which fall short of complete on-off switching. For example, in 3.10a, the signal drops to a sustained plateau with ~8-times lower photon count before completely switching off. In 3.10b the initial plateau is ~3 times higher than

the typical signal for **SMP3HT@glass** and exhibits no fading. It culminates with an extremely bright burst immediately after which it switches off for extended period of time. The sharp steps in the photon count may be caused by sudden conformational changes of the P3HT chain, which in the presence of Au can lead to different levels of enhancement and quenching. The dynamics of single fluorescent polymer chains in glass-like matrices has been probed in the past and the possibility of large conformational jumps is well documented [37, 38]. Such conformational change may put certain sectors of the polymer strand in a position of optimum radiative enhancement and lead to the sharp emission spikes seen in 3.10b and 3.10d. A conformational jump can also bring the chain in contact with the metal, triggering interfacial electron transfer (ET) and quenching of the emission, which can be restored only upon charge recombination. In this context it is important to keep in mind that molecular weight of 55 kD is equivalent to ~330 hexylthiophene repeat units, which in the all-trans configuration would span ~120 nm, a much longer distance than the 29 nm spacing between the Au nanorods. As a result, multiple points of contact between a strand and the metal may exist. Given that the exciton length of 8.6-13.4 nm [22] is much shorter than the length of the strand, independent ET events can take place at different locations along the chain and lead to the observed stepwise blinking, even if the conformation of the polymer remains static. Indeed, in our view such position dependent P3HT-to-metal and metal-to-P3HT ET processes play critical role in **SMP3HT@AuNR**, regardless of conformational gating.

As mentioned earlier, both electron and hole transfer between photoexcited P3HT and gold are thermodynamically possible. The corresponding tunneling rate follows exponential distance dependence, $k_{ET} \propto e^{-R\beta}$ controlled by the damping factor β which has been

determined for a range of intervening media, including a variety of polymers [39]. Given that in PMMA $\beta \approx 1 \text{ \AA}^{-1}$, the quenching of fluorescence by ET will show steep dependence on the separation between the P3HT strand and the Au surface. For example, if at a certain distance R_1 , the rate of electron transfer is 10-times slower than the intrinsic decay of the excited state of P3HT, quenching by ET will on the average occur once per 10 excitations. At a distance $R_2 = 3R_1$ the ET rate will be 20 times slower than at R_1 and thus it will occur only once per 200 excitations. As the ET quenching events grow more sporadic with increasing distance, so does the restoration of the emission because charge recombination follows analogous exponential distance dependence. The combination of these two low probability events (ET quenching and charge recombination) is the most likely cause of the sparse fluorescence trajectories in **SMP3HT@Au**. The trapping of the charges will further slow down the recombination and extend the “off” period. Conversely, P3HT strands for which the rate of ET to a nearby Au nanorod exceeds the intrinsic excited state decay rate, will undergo quenching upon most excitations and only rarely emit a photon. In either case, the presence of the ET channel will reduce the net “on” time of the fluorophore and counteract the enhancement effects, in some cases suppressing them altogether.

One way to analyze the dynamical events in single molecule spectroscopy is to calculate intensity autocorrelation function from the time trajectories of individual

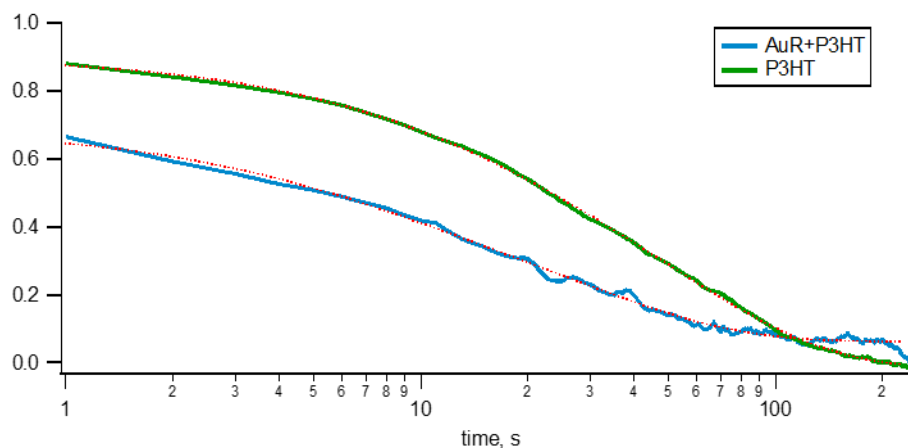


Figure 3.11 The average autocorrelation curves of P3HT embedded in PMMA on Au nanorod array (blue) and on glass (green).

molecules to extract the characteristic relaxation times [26]. Here, the autocorrelation function was applied to the averaged blinking trajectories recorded on glass and on the Au substrate rather than to individual traces. This compromise solution was adopted because the individual trajectories of **SMP3HT@Au** are too sparse to yield a well-behaved autocorrelation. The resulting autocorrelation curves are well reproduced by a double exponential decay function as shown in Figure 3.11. Both time components of the autocorrelation decay are nearly twice as fast for **SMP3HT@Au** as for **SMP3HT@glass** (Table 3.2). The faster loss of correlation for **SMP3HT@Au** points to a higher randomness of blinking, consistent with the presence of additional quenching channels and broader distribution of the duration of the “off” periods. Notably, the fast time constant τ_1 accounts for a much larger fraction (~23% vs 13%) of the amplitude in **SMP3HT@Au**. The total autocorrelation amplitudes in **SMP3HT@Au** and **SMP3HT@glass** are 0.55 and 0.91, respectively, suggesting that in the case of the

former a large fraction of correlation is lost within the duration of the sampling window.

	A_1	τ_1 (s)	A_2	τ_2 (s)	A_∞
P3HT@AuNR	0.23±0.02	5.3±0.91	0.68± 0.02	29±0.93	0.094±0.001
P3HT@glass	0.13±0.007	9.6±0.81	0.86±0.007	53±0.44	0.019±0.0007

Table 3.2 Time constants recovered from the autocorrelation curves shown in Figure 3.11.

The fluorescence spectra for **SMP3HT@Au** show on the average an approximately five-fold enhancement of intensity in comparison with **P3HT@glass** (Figure 3.12a), thus confirming a substantial plasmonic enhancement in the presence of Au nanorods. As above, because of the extremely erratic blinking and long off-periods in **SMP3HT@Au**, collecting complete single molecule spectra with a consistent signal to noise ratio was challenging. As a compromise, we analyzed averaged fluorescence spectra of 10 individual emitters on the Au substrate and 6 on glass. Aside from the enhancement, the spectrum of **SMP3HT@Au** (black) is very similar to that of **SMP3HT@glass** (red). This suggests that the coupling between the emissive strands of P3HT and the Au nanorods is moderate, i.e. sufficient to accelerate the radiative rate but not large enough to cause gross spectral changes (Table 3.3). For chromophores which are strongly coupled to the metal, the quenching at the interface dominates over the radiative enhancement. While the instantaneous brightness of such strongly coupled chromophores at $t = 0$ may be high, under cw excitation they will appear less bright than the **SMP3HT@glass**.

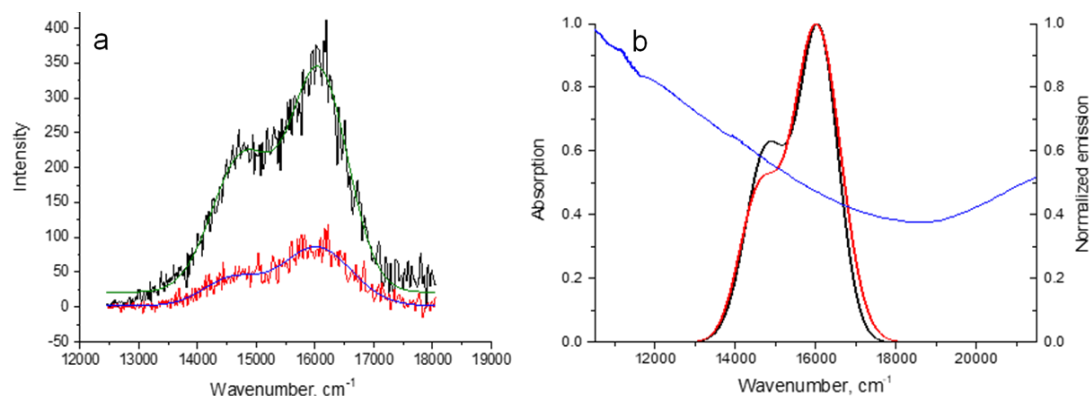


Figure 3.12 (a) Averaged single molecule emission spectra measured on glass (red) and the Au nanorod substrate (black); (b) Normalized double Gaussian fits of the spectra in (a) plotted together with the spectrum of the Au nanorod array (blue).

The parameters of the Gaussian fit of the fluorescence spectrum (Figure 3.12b and Table 3.3) of **SMP3HT@AuNR** reveals different degree of enhancement for the 0-0 and 0-1 vibronic peaks, with the latter gaining ~ 1.75 -times more intensity as the former. Even the weak 0-2 peak becomes discernible as a shoulder at $\sim 13500 \text{ cm}^{-1}$ in the presence of the Au nanorods. The plasmon band of the nanorod array (Figure 3.12b) is approximately 1.5 times more intense at ν_{01} than at ν_{00} and grows stronger at longer wavelengths possibly explaining the higher enhancement of the 0-1 peak. The blue shift of the 0-1 peak is also greater than of the 0-0 one by a significant amount (~ 200 vs $\sim 50 \text{ cm}^{-1}$). It is not clear how to interpret the implicit large difference of the vibrational frequency in terms of the coupling between fluorophore and the meta.

.	$\nu_{00} (\text{cm}^{-1})$	$\nu_{01} (\text{cm}^{-1})$	$\text{FWHM}_{00} (\text{cm}^{-1})$	$\text{FWHM}_{01} (\text{cm}^{-1})$	A_{01}/A_{00}
P3HT@AuNR	16066 ± 9	14763 ± 15	1151 ± 17	1222 ± 27	0.65 ± 0.030
P3HT@glass	16020 ± 15	14578 ± 29	1399 ± 34	1151 ± 55	0.37 ± 0.028

Table 3.3 Fitting parameters retrieved from the fluorescence spectra in Figure 3.12.

3.4 Conclusions

While comprehensive understanding of the dynamics in photoexcited P3HT coupled to a nanostructured gold substrate remains challenging, several important insights were gained as a result of the reported experiments. Expectedly, the behavior in bulk **P3HT@AuNR** is more complex than of **P3HT@glass**, primarily because additional pathways for charge separation and recombination are available in the former. The general trend is a significant reduction of the lifetime of excitons and charge carriers of the presence of metal. The overall population of transient species which survive past the 10 ps mark is approximately 50% lower than for the samples on glass. We conclude that in the regions of P3HT which are within the exciton length of the interface, excitons and nascent polaron pairs dissociate rapidly via tunneling of one of the carriers to the metal, leading to nearly instantaneous quenching of the excited state. This behavior is common for the bulk P3HT and for single strands of the polymer dispersed in PMMA on the AuNR substrate.

Very interestingly, the presence of the Au nanorod array greatly increases the yield of triplet excitons in the deposited bulk P3HT. We postulate that this effect is caused by the rapid loss of the electron-hole spin-spin correlation via efficient electron exchange at the polymer-metal interface followed by the statistically favored formation of triplet excitons rather than by the acceleration of intersystem crossing in the initial singlet exciton.

The single molecule experiments show that fortuitously located excitons in can experience very large radiative enhancement in the presence of the Au nanostructure. Such enhanced emission by a small fraction of excitons may be present also in the bulk P3HT on the gold substrate, however, it is not discernible in the pump-probe transient absorption experiments. The unique feature observed in the single molecule experiments is the extremely erratic

blinking behavior, both in terms of the duration of the “off” periods and the abruptly changing fluorescence amplitude. We ascribe it to sporadic electron transfer events between the P3HT strands and the Au substrate, which quench sections of the chain for long periods of time. On the basis of the limited data set, the fluorescence of single strands of P3HT interacting with the Au nanorods appears to fall into two well defined extremes of either nearly total quenching or strong enhancement of the emission with the “off” periods modulated by interfacial electron transfer.

References

1. Braga, D. and G. Horowitz, *High-performance organic field-effect transistors*. Advanced Materials, 2009. **21**(14-15): p. 1473-1486.
2. Khurgin, J.B. and G. Sun, *Enhancement of optical properties of nanoscaled objects by metal nanoparticles*. Journal of the Optical Society of America B, 2009. **26**(12).
3. Atwater, H.A. and A. Polman, *Plasmonics for improved photovoltaic devices*. Nature Materials, 2010. **9**(3): p. 205-213.
4. Heo, M., et al., *High-performance organic optoelectronic devices enhanced by surface plasmon resonance*. Advanced Materials, 2011. **23**(47): p. 5689-5693.
5. Komiyama, H., et al., *Longitudinal and lateral integration of conducting polymer nanowire arrays via block-copolymer-templated electropolymerization*. Chemistry of Materials, 2015. **27**(14): p. 4972-4982.
6. Bao, Z., A. Dodabalapur, and A.J. Lovinger, *Soluble and processable regioregular poly(3-hexylthiophene) for thin film field-effect transistor applications with high mobility*. Applied Physics Letters, 1996. **69**(26): p. 4108-4110.
7. Spano, F.C., *Modeling disorder in polymer aggregates: The optical spectroscopy of regioregular poly(3-hexylthiophene) thin films*. The Journal of Chemical Physics, 2005. **122**(23).
8. Tremel, K. and S. Ludwigs, *Morphology of P3HT in thin films in relation to optical and electrical properties*. 2014. **265**: p. 39-82.
9. Cardona, C.M., et al., *Electrochemical considerations for determining absolute frontier orbital energy levels of conjugated polymers for solar cell applications*. Advanced Materials, 2011. **23**(20): p. 2367-2371.

10. Ogata, Y., D. Kawaguchi, and K. Tanaka, *An effect of molecular motion on carrier formation in a poly(3-hexylthiophene) film*. Scientific Reports, 2015. **5**(1).
11. Arkhipov, V.I., E.V. Emelianova, and H. Bässler, *Hot exciton dissociation in a conjugated polymer*. Physical Review Letters, 1999. **82**(6): p. 1321-1324.
12. Arkhipov, V.I., et al., *Ultrafast on-chain dissociation of hot excitons in conjugated polymers*. Physical Review B, 2000. **61**(12): p. 8207-8214.
13. Basko, D.M. and E.M. Conwell, *Hot exciton dissociation in conjugated polymers*. Physical Review B, 2002. **66**(15).
14. Soller, T., et al., *Radiative and nonradiative rates of phosphors attached to gold nanoparticles*. Nano Letters, 2007. **7**(7): p. 1941-1946.
15. Goda, T. and T. Iyoda, *Ultrahigh density electrolytic nanoreactors composed of liquid crystalline block copolymer template: water-electrolysis-induced deposition of cerium oxyhydroxide nanorod array*. Journal of Materials Chemistry, 2012. **22**(19).
16. Morita, S., A.A. Zakhidov, and K. Yoshino, *Doping effect of buckminsterfullerene in conducting polymer: Change of absorption spectrum and quenching of luminescence*. Solid State Communications, 1992. **82**(4): p. 249-252.
17. Zhang, W., A.O. Govorov, and G.W. Bryant, *Semiconductor-metal nanoparticle molecules: hybrid excitons and the nonlinear fano effect*. Physical Review Letters, 2006. **97**(14).
18. Bouhelier, A., et al., *Electromagnetic interactions in plasmonic nanoparticle arrays*. The Journal of Physical Chemistry B, 2005. **109**(8): p. 3195-3198.

19. Rechberger, W., et al., *Optical properties of two interacting gold nanoparticles*. Optics Communications, 2003. **220**(1-3): p. 137-141.
20. Korovyanko, O.J., et al., *Photoexcitation dynamics in regioregular and regiorandom polythiophene films*. Physical Review B, 2001. **64**(23).
21. Jiang, X.M., et al., *Advanced Functional Materials*, 2002. **12**(9): p. 587-597.
22. Guo, J., et al., *Near-IR femtosecond transient absorption spectroscopy of ultrafast polaron and triplet exciton formation in polythiophene films with different regioregularities*. Journal of the American Chemical Society, 2009. **131**(46): p. 16869-16880.
23. Hwang, I.-W., D. Moses, and A.J. Heeger, *Photoinduced carrier generation in P3HT/PCBM bulk heterojunction materials*. The Journal of Physical Chemistry C, 2008. **112**(11): p. 4350-4354.
24. Lee, S.M. and K.C. Choi, *Distance-dependent plasmonic enhancement via radiative transitions of Europium complex*. Optics Letters, 2013. **38**(8): p. 1355.
25. Ostrowski, J.C., et al., *Enhancement of phosphorescence by surface-plasmon resonances in colloidal metal nanoparticles: the role of aggregates*. Advanced Functional Materials, 2006. **16**(9): p. 1221-1227.
26. Pan, S. and L.J. Rothberg, *Enhancement of platinum octaethyl porphyrin phosphorescence near nanotextured silver surfaces*. Journal of the American Chemical Society, 2005. **127**(16): p. 6087-6094.
27. Djiango, M., et al., *Spectral tuning of the phosphorescence from metalloporphyrins attached to gold nanorods*. Optics Express, 2012. **20**(17).

28. Guo, J., et al., *Charge generation and recombination dynamics in poly(3-hexylthiophene)/fullerene blend films with different regioregularities and morphologies*. Journal of the American Chemical Society, 2010. **132**(17): p. 6154-6164.
29. Takeda, N. and J.R. Miller, *Poly(3-decylthiophene) radical anions and cations in solution: single and multiple polarons and their delocalization lengths in conjugated polymers*. The Journal of Physical Chemistry B, 2012. **116**(50): p. 14715-14723.
30. Wöll, D., et al., *Polymers and single molecule fluorescence spectroscopy, what can we learn?* Chem. Soc. Rev., 2009. **38**(2): p. 313-328.
31. Vacha, M. and S. Habuchi, *Conformation and physics of polymer chains: a single-molecule perspective*. NPG Asia Materials, 2010. **2**(4): p. 134-142.
32. Lupton, J.M., *Single-molecule spectroscopy for plastic electronics: materials analysis from the bottom-up*. Advanced Materials, 2010. **22**(15): p. 1689-1721.
33. Sugimoto, T., et al., *Structure-dependent photophysics studied in single molecules of polythiophene derivatives*. ChemPhysChem, 2007. **8**(11): p. 1623-1628.
34. Sugimoto, T., et al., *Conformation-related exciton localization and charge-pair formation in polythiophenes: ensemble and single-molecule study*. The Journal of Physical Chemistry B, 2009. **113**(36): p. 12220-12226.
35. Adachi, T., et al., *Regioregularity and single polythiophene chain conformation*. The Journal of Physical Chemistry Letters, 2011. **2**(12): p. 1400-1404.

36. Thiessen, A., et al., *Unraveling the chromophoric disorder of poly(3-hexylthiophene)*. Proceedings of the National Academy of Sciences, 2013. **110**(38): p. E3550-E3556.
37. Lin, H., et al., *Fluorescence blinking, exciton dynamics, and energy transfer domains in single conjugated polymer chains*. Journal of the American Chemical Society, 2008. **130**(22): p. 7042-7051.
38. Honmou, Y., et al., *Single-molecule electroluminescence and photoluminescence of polyfluorene unveils the photophysics behind the green emission band*. Nature Communications, 2014. **5**.
39. Wold, D.J., et al., *Distance dependence of electron tunneling through self-assembled monolayers measured by conducting probe atomic force microscopy: unsaturated versus saturated molecular junctions*. The Journal of Physical Chemistry B, 2002. **106**(11): p. 2813-2816.

Chapter 4. Vibrational cooling and electron transfer in oligomeric viologens of different size and topology

In this chapter, vibrational cooling was investigated in a set of homologous dimers and trimers with methyl viologen repeat units (MV^{2+}). The rapid, < 500 fs decay of the D_1 excited state of monoreduced viologen ($MV^{+\bullet}$) via a conical intersection allows the preparation of a vibrationally hot D_0 ground state with large excess energy of 0.6 eV, which is equivalent to initial effective temperature of ~ 800 K. The subsequent decay rates for the hot D_0 states were probed by pump-probe spectroscopy and corroborated by molecular dynamics (MD) simulations. The observed cooling rates depend on the size and topology of the oligomer, with the linear trimer exhibiting significantly faster thermalization than the branched one. The dynamics of the thermal equilibration in these systems appears to be consistent with the primarily ballistic propagation of the vibrational excess energy and exhibits interference between the equivalent pathways in the branched trimer.

Later, it was found that in a covalently linked viologen dimer, $MV^{++}-MV^{++}$, the photoexcited singly reduced mixed valence species $MV^{+\bullet}-MV^{++}$ returns to the ground state considerably faster than either the monomeric $MV^{+\bullet}$ or the fully symmetric, $MV^{+\bullet}-MV^{+\bullet}$, doubly reduced form of the dimer. We postulate that the deactivation of the D_1 excited state in the mixed valence species is accelerated by the competition between the local, intramolecular internal conversion in the excited $MV^{+\bullet}$ moiety and photoinduced electron transfer to the MV^{++} unit. The extracted electron transfer rate agrees well with the thermodynamic parameters and computational estimates of the viologen-viologen electronic coupling.

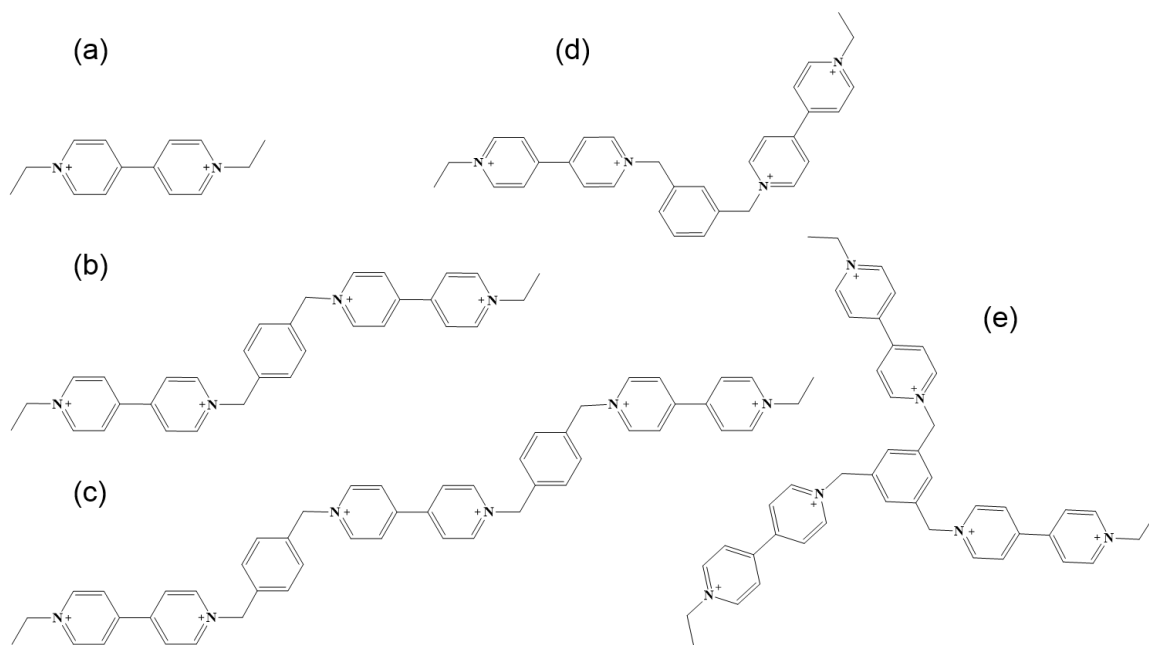


Figure 4.1 Molecular structure of oligomers. (a) Monomer. (b) Para (linear) dimer. (c) Para (linear) trimer. (d) Meta dimer. (e) Meta (star) dimer.

4.1 Introduction

As discussed in section 1.2, molecules with not fully equilibrated thermal energies or “hot” molecules generated by the IVR dominated processes are crucial in the study of vibrational cooling. The excess vibrational energy contained by such molecules can sometimes be equivalent to thousands of kelvins, which is very difficult, often impossible to achieve by routine experimental methodologies [1-5]. The dominating mechanism of the dissipation of the corresponding excess vibrational energy (ballistically or diffusively) can be described and determined by models of heat transfer in molecular junctions, which has been elaborated in section 1.2.1 [6-8]. While it is universal for all molecules returning to electronic ground state via internal conversion to contain excess vibrational energies, for

the application in the study of vibrational cooling, the internal conversion (IC) need to be very rapid. For instance, one of the molecules most widely used in the study of vibrational cooling is azulene, which exhibit rapid internal conversion from S_1 to S_0 in 2 ps [9, 10]. Other experimental and theoretical studies have been carried out on a broad variety of systems such as large chromophores connected by bridges [9, 11], alkane chains [12, 13], biomolecules [14], nanostructures [8, 15] and SAMs [16].

Our interest in vibrational relaxation and cooling has been prompted by the pivotal role they play in intramolecular electron transfer processes occurring on sub-picosecond and short picosecond timescales [17]. Because such systems are not fully thermally equilibrated, neither internally nor with the surroundings, they cannot be expected to obey the predictions of the convenient and widely used closed-form theoretical models such as the Marcus or Marcus-Jortner equations, which are based on equilibrium thermodynamics. It has been demonstrated both in molecular systems and at interfaces that electron transfer from vibrationally hot states may be orders of magnitude faster, leading to unexpected results and interesting venues for the design of light harvesting materials [18].

Here we report the investigation of vibrational cooling and electron transfer in a series of oligoviologen arrays (Figure 4.1). In the context of this work, the methyl viologen radical cation moiety served as the building block to construct molecular junctions. By altering the number of viologen units and the linkage to the bridge (para and meta), the influence of molecular size and linear vs branched topology on the energy redistribution and equilibration with the solvent were probed in detail in section 4.3.1.

4.1.1 Properties of the methyl viologen radical cation

Methyl viologen is commonly used in photochemistry, where due to its outstanding ability to accept electrons it often serves as a component of the donor-acceptor systems [19]. Upon accepting an electron, the methyl viologen cation becomes brightly colored monoreduced radical $MV^{+\bullet}$. Most relevant to this study is the ultrafast internal conversion of the D_1 excited state of $MV^{+\bullet}$ which within less than 0.5 ps decays via a conical intersection to the to highly vibrationally excited (~ 0.6 eV) ground state which can be readily detected by pump-probe spectroscopy. The formation of the latter has been detected by femtosecond resonance Raman spectroscopy (Huang and Hopkins) and subsequently by transient absorption spectroscopy (Häupl et al.) [20, 21]. It is therefore an ideal system that allows one to employ electronic excitation to set up nearly instantaneously a localized vibrationally hot state and monitor its subsequent evolution.

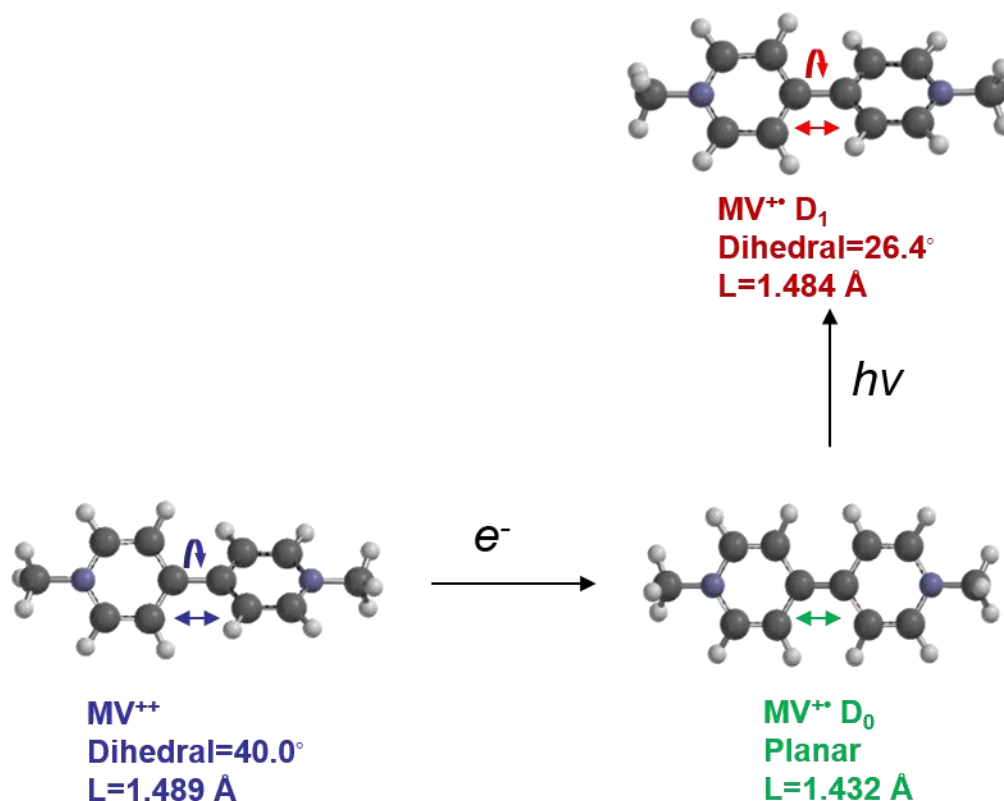


Figure 4.2 Schematic diagram showing the monoreduction of MV^{++} and the photoexcitation of $MV^{+•}$.

$MV^{+•}$ in D₀ state exhibits a quinonoid planar structure. Upon photoexcitation to the D₁ state, the two rings in the molecule twist to form a dihedral angle of approximately 30°. Figure 4.3 shows the 3D plot of molecular energies of MV^{++} and $MV^{+•}$ versus varying dihedral angle and central bond length. The plot suggests that the D₁ to D₀ internal conversion is closely correlated to the relaxation rotation of the rings in the molecule. As a result, the respective skeletal (high frequency) and torsional (low frequency) normal modes and the corresponding D₀-D₁ Franck-Condon factors have strong influence on the observed decay dynamics and spectral evolution. Furthermore, the similarities in the shape of energy plot

of MV^{++} and $MV^{+\bullet}$ in D_1 indicates a highly possible electron transfer between the two states in oligoviologens consisting of $*MV^{+\bullet}$ and MV^{++} .

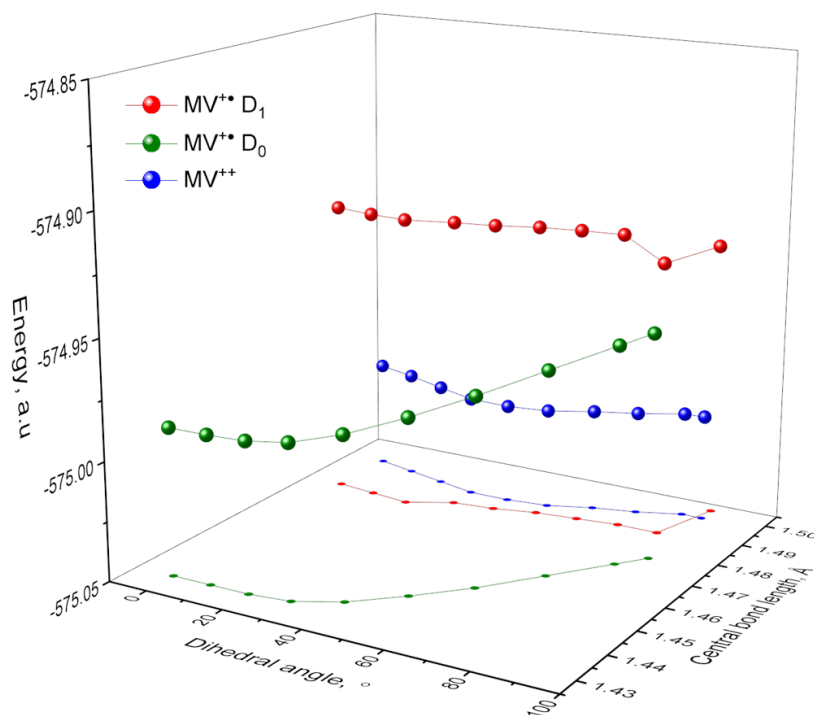


Figure 4.3 3D plot of energy versus varying dihedral angle and central bond lengths in D_0 and D_1 states of $MV^{+\bullet}$ and the S_0 state of MV^{++} , calculated by DFT at B3LYP 6-31G* level.

In the simplest case of a mixed valence dimer (Figure 4.4 top) $MV^{+\bullet}-MV^{++}$, the $D_1-S_0 \rightarrow S_0-D_0$ electron transfer is spin allowed. Electron transfer in the $*MV^{+\bullet}-MV^{++}$ system lies very close to the thermodynamic optimum, allowing it to be sufficiently fast to compete with the local internal conversion at the photoexcited $MV^{+\bullet}$ site and could in principle accelerate the overall cooling rate of hot viologen moiety. The influence of electron transfer

and the vibrational cooling of hot D_0 state in such mixed valence dimer is also studied. The discussion can be found in section 4.3.2.

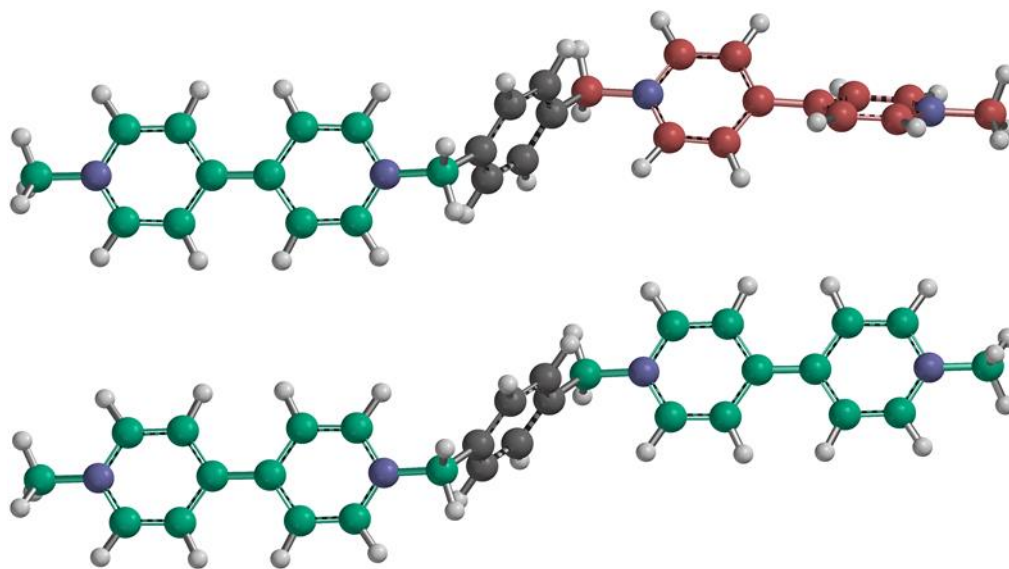


Figure 4.4 Structure of the singly (top) and doubly (bottom) reduced dimer.

4.2 Sample preparation

Fully reduced oligomers: Each compound (monomer, L-dimer, L-trimer and star trimer) was dissolved in degassed acetonitrile (>99.9%, Sigma-Aldrich) to make a concentrated solution of $\sim 3 \times 10^{-3}$ M. Excess of zinc powder was added and allowed to react for overnight to singly reduce every viologen units in each array. Each concentrated solution was diluted using degassed acetonitrile to reach a concentration of $\sim 8 \times 10^{-5}$ M and pipetted into a 1 cm quartz cell with an air tight seal for subsequent measurements. All steps were performed in a glove box.

Mixed valence dimer: The singly reduced form $MV^{+\bullet}-MV^{++}$ was made by mixing equal concentrated $MV^{+\bullet}-MV^{+\bullet}$ and $MV^{++}-MV^{++}$ with 1 to 1 ratio. All preparation steps were

performed in a glove box and spectroscopic measurements were done in a 1 cm quartz cuvette with an air tight seal.

4.3 Vibrational cooling in linear and branched oligoviologens

4.3.1 Steady state absorption measurements

The D₀-D₁ ground state absorption spectra of all four reduced oligomers exhibit vibronic structure and peak position at 600 nm, which are nearly identical to these of the monomeric MV^{••} (Figure 4.5). The trimers show slightly more pronounced broadening of the high energy side of the spectrum which in the case of the linear para-bridged compound is magnified by the contributions of the inequivalent sites at the termini and in the center of the molecule. Overall, these differences are minor and do not merit further discussion. By correlating concentration and the measured absorption coefficient, it was concluded that every viologen unit in each oligomer was singly reduced. The close similarity of the spectra shows that the MV^{••} moieties interact only weakly with one another and that the electronic states of interest remain well localized on just one repeat unit. As a result, in the pump-probe experiments, the excited state and the resulting vibrationally hot ground state are initially localized at a single MV^{••} site. Due to the low photon density employed in these experiments, the probability of exciting more than one reduced viologen unit per oligomer is negligibly small. The localization of electronic states is supported by the calculated electronic coupling between the LUMO orbitals of the MV⁺⁺ sites, which is 68 cm⁻¹ for the para and 97 cm⁻¹ for the meta linkage. (HF, 6-311+G**, Spartan'16 by Wavefunction, Inc.). The larger interaction in the meta bridged systems indicates the dominance of the σ coupling pathway.

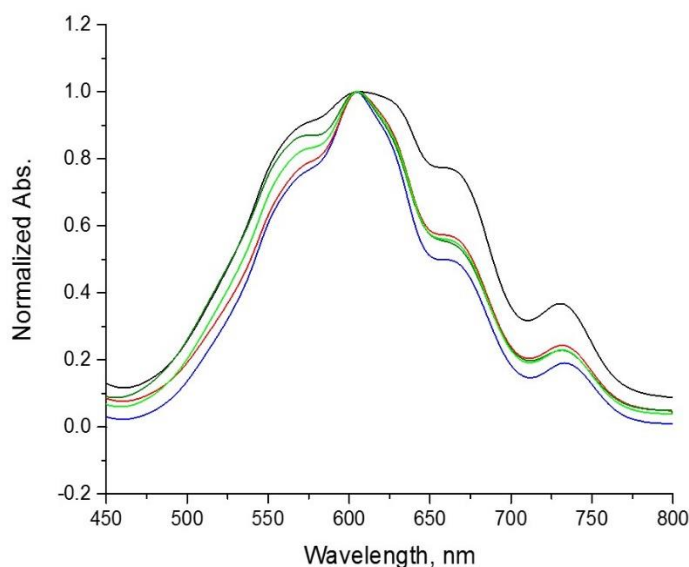


Figure 4.5 Ground state absorption of the reduced monomer (blue), linear dimer (red), meta dimer (light green), linear trimer (black) and star trimer (olive).

4.3.2 Pump-probe experiments

The transient absorption spectra of the five compounds are also similar to one another and display three discernible bands at ~ 710 , ~ 770 and ~ 850 nm (Figure 4.6), which aside from the red shift mimic the appearance of the cw spectrum of $MV^{+\bullet}$. This similarity and the spectral dynamics lead Häupl *et al* to assign the transient spectrum to the vibrationally “hot” electronic ground state rather than the D_1 excited state.[21] The temporal evolution of the transient spectrum reflects the vibrational temperature of the molecule, with the red-most wavelengths reporting the hottest ground state species immediately after the internal conversion and the shorter ones encompassing a broader range of excess energy and persisting at more advanced stages of thermal equilibration with the solvent. Accordingly, the measurements were carried out at three values of λ_{probe} : 845, 762 and 703 nm. On the other hand, similarly to monomeric viologen, the cooling dynamics in the oligomers is only

weakly dependent on the excitation wavelength and all results discussed below were carried out at a fixed $\lambda_{exc} = 550$ nm. In the $MV^{+\bullet}$ oligomers, the evolving hot spectrum is a sum of contributions from the photoexcited moiety whose internal temperature decreases throughout the scan, as well as the remaining sites, whose vibrational temperature initially increases until the entire system begins to cool down and equilibrate with the solvent.

λ_{probe} , nm	703	762	845
Rise time, fs	562 \pm 22	317 \pm 13	239 \pm 17

Table 4.1 Rise time of populations probed at 703 nm, 762 nm and 845 nm in the linear dimer excited at 550 nm.

The probe wavelength – internal temperature correlation is reflected both in the rise time and the decay of the hot spectrum. As expected, we observed the fastest, ~240 fs formation of the ground state, at the longest probe wavelength of 845 nm (Table 4.1). At shorter probe wavelengths the rate of formation of the hot ground state is slower because the overall rise of the signal is a composite result of direct population by internal conversion combined with vibrational energy redistribution (IVR) from the highest vibrational states. These results are consistent with our prior observations in monomeric $MV^{+\bullet}$, confirming that the electronic interactions between the sites are weak and do not significantly alter the internal conversion process. As in the case of the monomer, the formation rates reported here are faster than the early literature value [20, 21], most likely because of the superior time resolution of the present experimental setup.

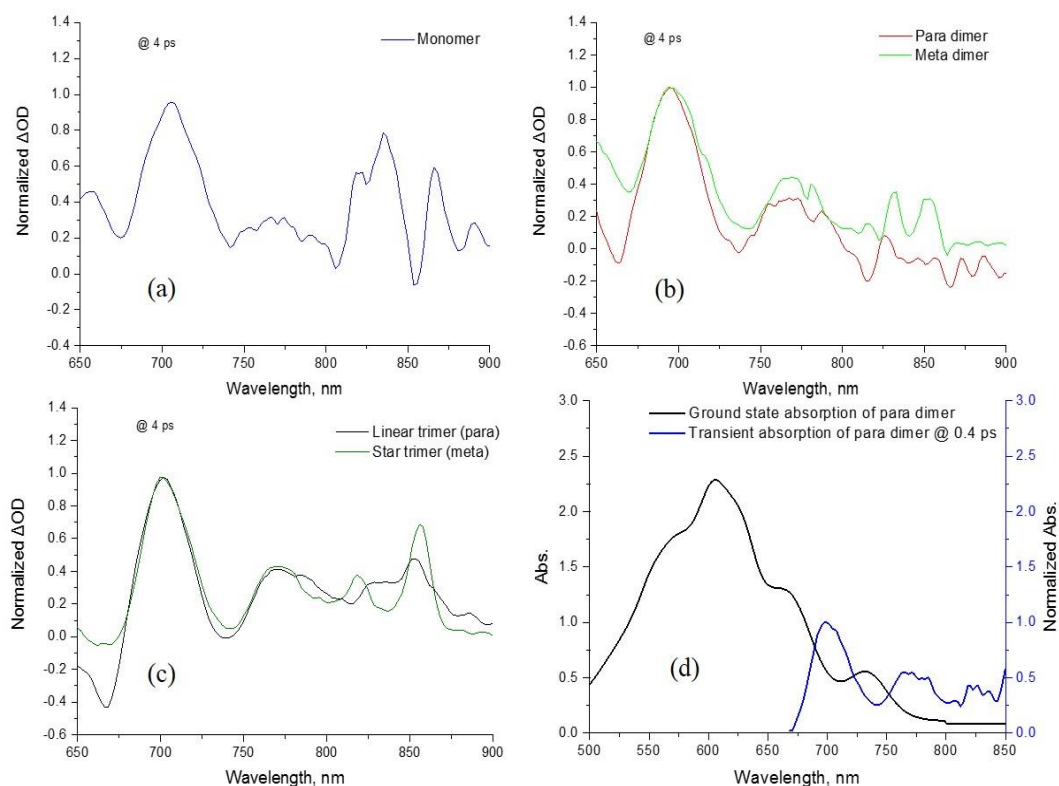


Figure 4.6 (a) Normalized transient absorption spectra of the reduced monomer (blue), linear dimer (red), meta dimer (light green), linear trimer (black) and star trimer (olive) at 4 ps after excitation at 550 nm. (b) Overlay of ground state absorption and TA spectrum at 4 ps spectrum of the reduced dimer.

The cooling profiles are collected in Figure 4.7. It is apparent that for all molecules the decay dynamics is by far fastest at the longest probe wavelength of 845 nm, which is sensitive to the hottest population of the ground state. Secondly, at all probe wavelengths the cooling process is perceptibly faster in the oligomers than in monomeric viologen, however, the differences among the oligomers are much more subtle. The lack of pronounced dependence on the number of repeat units is consistent with ballistic

propagation dominating over stochastic, heat-like energy redistribution and intramolecular equilibration [4, 6].

Parameters recovered from double exponential fitting of the decay profiles are gathered in Table 4.2. In order to achieve convergence, the fitting required the inclusion of an adjustable offset, A_∞ , of variable magnitude. The origin of this behavior is uncertain and we tentatively ascribe it to an artifact caused by residual thermal lensing. Given the complexity of the cooling process, empirical fitting does not have direct mechanistic correspondence, however, the existence of two general cooling regimes can be identified. The initial, steep decay of the hot population occurs with $\tau = 1.4 - 2.3$ ps, while the slowest components extend all the way to 18 ps, consistent with IVR dominating the early times followed by slower dissipation to the solvent. The biphasic nature of the equilibration is most pronounced at the longer wavelengths, especially in the monomer, for which at 703 nm the decay can be fitted only with a single exponential. This behavior is reasonable because in the monomer the cutoff between the internal vibrational equilibrated and subsequent heat transfer to the solvent should be most pronounced.

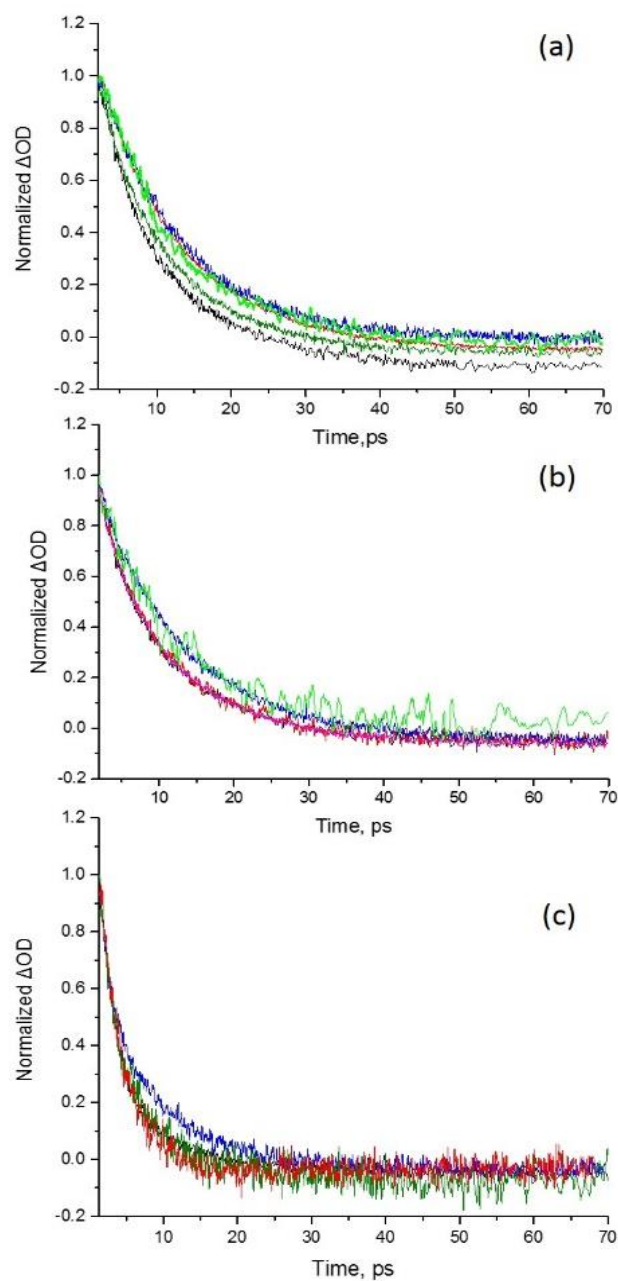


Figure 4.7 Transient absorption decay profiles for the monomer (blue), para dimer (red), meta dimer (light green), linear trimer (black) and star trimer (olive) excited at 550 nm and probed at different wavelengths: (a) 703 nm; (b) 762 nm; (c) 845 nm.

λ_{probe}		τ_1/ps	A_1	τ_2/ps	A_2	A_∞
703 nm	Monomer	11 ± 0.04	0.89 ± 0.002			0.1 ± 0.0005
	Linear dimer	8.3 ± 0.6	0.49 ± 0.1			-0.06 ± 0.001
	Meta dimer	9 ± 1.5	0.71 ± 0.3			-0.04 ± 0.002
	Linear trimer	5.0 ± 0.3	0.57 ± 0.05			-0.12 ± 0.002
	Meta trimer	3.7 ± 0.4	0.16 ± 0.03			-0.06 ± 0.001
762 nm	Monomer	8.6 ± 0.1	0.49 ± 0.3	15 ± 0.3	0.51 ± 0.03	-0.05 ± 0.003
	Linear dimer	3.3 ± 0.3	0.28 ± 0.03	11 ± 0.2	0.77 ± 0.03	-0.05 ± 0.001
	Meta dimer	3.5 ± 0.2	0.22 ± 0.07	11 ± 0.5	0.74 ± 0.09	0.01 ± 0.006
	Linear trimer	3.9 ± 0.2	0.38 ± 0.03	12 ± 0.3	0.67 ± 0.03	-0.07 ± 0.001
	Meta trimer	3.4 ± 0.01	0.25 ± 0.01	11 ± 0.01	0.81 ± 0.001	-0.06 ± 0.001
845 nm	Monomer	1.7 ± 0.07	0.44 ± 0.01	9.1 ± 0.2	0.57 ± 0.01	-0.04 ± 0.001
	Linear dimer	1.4 ± 0.7	0.17 ± 0.1	3.6 ± 0.2	0.88 ± 0.01	-0.04 ± 0.003
	Linear trimer	2.2 ± 0.04	0.75 ± 0.01	10 ± 0.4	0.28 ± 0.01	-0.05 ± 0.001
	Meta trimer	2.3 ± 0.2	0.69 ± 0.04	8.8 ± 0.7	0.39 ± 0.05	-0.08 ± 0.002

Table 4.2 Double exponential decay fitting parameters of monomer, linear dimer, meta dimer, linear trimer and meta trimer excited at 550nm and probed at 703 nm, 762 nm and 845 nm.

The substantial crosstalk between the fitting parameters in Table 4.2 (both time constants and relative amplitudes of the fast and slow decay components) cautions one not to over-interpret the differences between individual rates and amplitudes. With the τ_1/τ_2 ratio rarely exceeding 3, the time constants are not well separated and it is very helpful to examine the data plotted as survival time τ_s of a certain fraction of the initial population (Figure 4.8). In

this simplistic representation, at the longest probe wavelengths reporting initial stages of the equilibration, the behavior of all three oligomers is practically indistinguishable, reinforcing the notion of ballistic propagation of vibrational energy dominating the early stages of the cooling process. The greatest differences among the examined systems are seen at the shortest probe wavelength, $\lambda_{probe} = 703$ nm, i.e. for the already somewhat internally equilibrated and cooled molecules. While the dimers are nearly indistinguishable from one another or the monomer, the trimers reach thermal equilibrium with the solvent up to 35% sooner. This difference is likely a combined outcome of the increased surface area of the trimers, which is partially balanced by lower temperature gradient between the molecule and the solvent upon the completion of intramolecular redistribution of the vibrational energy among three rather than two viologen moieties. Very interestingly, at 703 nm the cooling profiles of the linear and star trimer diverge, with the latter exhibiting ~15 % slower relaxation. This divergence cannot be rationalized in terms of simple surface area or number of vibrational modes arguments and suggests the possibility of vibrational interference between the equivalent pathways in the branched meta bridged system.

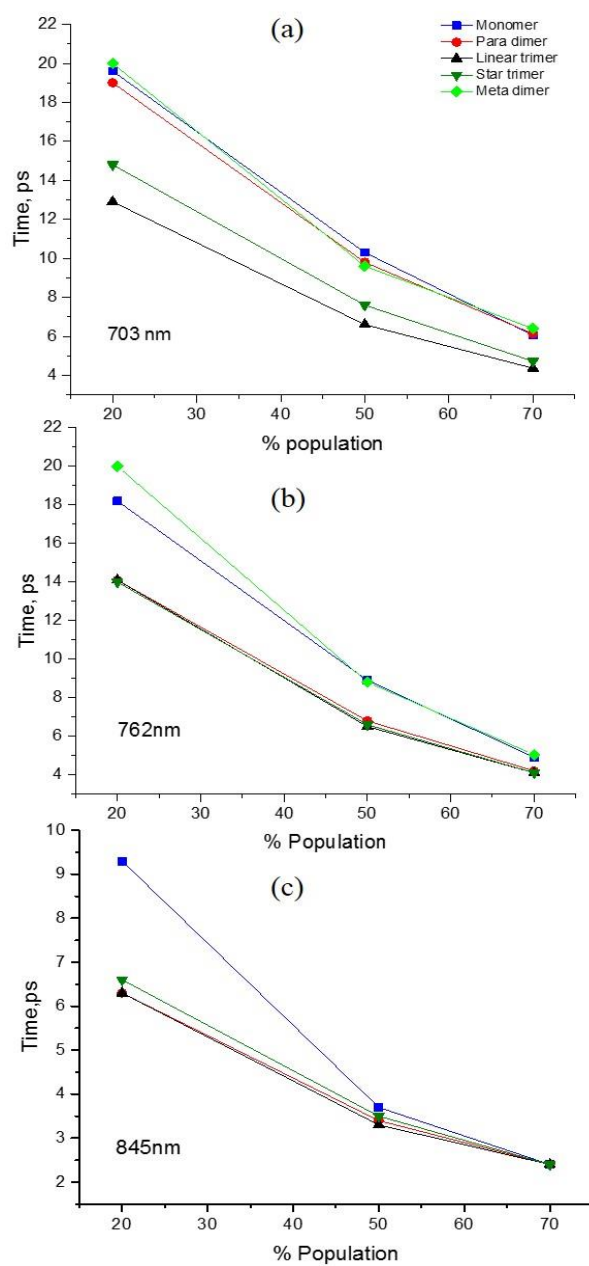


Figure 4.8 Survival time vs. population profiles at different probe wavelengths. Blue: monomer; Red: dimer; Black: linear trimer; Green: star trimer.

4.3.3 MD simulations

Standard pump-probe spectra and decay profiles monitor only the average evolution of the ensemble and cannot unravel the full complexity of the intramolecular heat flow and the cooling process. Classical molecular dynamics (MD) simulations were carried out in order to augment our understanding of the underlying vibrational energy redistribution, especially at early times. In addition, we could monitor not only the energy loss of the initially excited site but also the vibrational energy gain of the remaining viologens and bridging units. The computational procedures were selected to realistically mimic the conditions and limitations of the experiment. Because our 1-D pump-probe measurements do not reveal any apparent coherence and, unless a strongly coupled dominant mode is present, are generally insensitive to such effects, it was chosen to “heat” a monomeric viologen moiety to 1000 K at the beginning of the simulation while the rest of the oligomer remained at room temperature. The initial temperature of the hot viologen was estimated on the basis of the known overall excess energy ($18,200\text{ cm}^{-1}$) and the number of normal modes. By simulating the vibrational excitation via rescaling of atom velocities rather than depositing an equivalent amount of energy in a mode or modes which may be selectively populated upon passing through the conical intersection, the unintended mode specificity has been eliminated. More advanced four wave mixing experiments on these systems might reveal the existence of vibrational coherence at early times after the formation of the hot ground state and would necessitate a different ansatz and computational approach.

Each trajectory shown in Figure 4.9 is an average of five individual simulations. The loss of energy by the hot viologen and the corresponding gain by the remainder of the molecule is evident in all traces. Given the simplicity of the model, the general agreement with the

experimental results, especially at early times after photoexcitation, is good. For example, the biphasic equilibration in the linear dimer (Figure 4.9a) consists of components with $\tau_1 = 2.0 \pm 0.1$ ps and $\tau_2 = 11.0 \pm 0.4$ ps. The former time constant agrees very well with the experimental $\tau_1 = 1.4 \pm 0.7$ ps, while the latter is considerably slower than the measured value of $\tau_2 = 3.6 \pm 0.4$ ps. This is likely to reflect anharmonicity and heat transfer to the solvent. The trajectories for the star trimer can be fitted only with a single exponential with $\tau = 5.9 \pm 0.1$ ps.

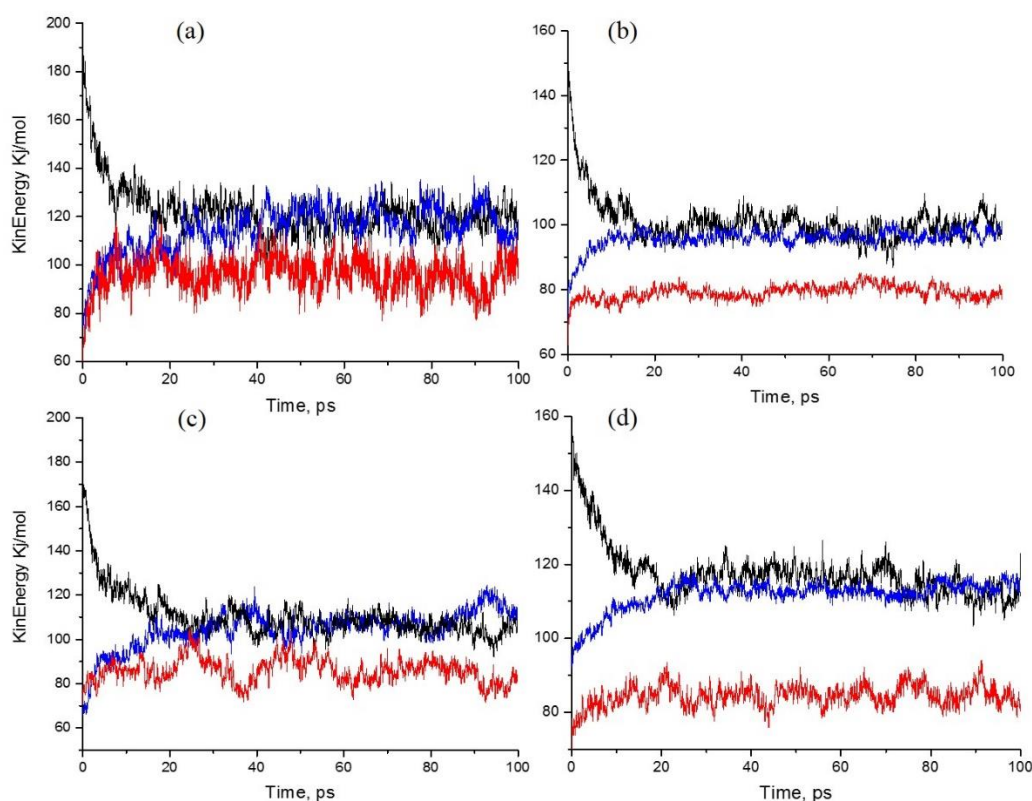


Figure 4.9 Averaged MD trajectories of the hot viologen (black), cold viologen (blue) and the bridge (red) in: (a) para dimer; (b) linear trimer; (c) meta dimer; (d) star trimer.

Significantly, we observe similar time scales for the energy flow to the bridging units and the cold viologen moieties, again pointing to the ballistic rather than stochastic nature of the process, where the latter would lead to a more gradual propagation of the energy across the system. There is no indication that the excess energy is at any time localized on the bridge and only subsequently dissipated onto the cold viologens.

	τ_1 /ps	A_1	τ_2 /ps	A_2
Energy loss by the hot viologen				
Linear dimer	2.0±0.08	0.63±0.01	11±0.4	0.37±0.01
Meta dimer	1.1±0.05	0.65±0.03	11±0.2	0.35±0.004
Linear trimer	0.76±0.06	0.40±0.01	5.2±0.09	0.60±0.01
Star trimer	5.9±0.05	1±0.006		
Energy gain of the cold viologens				
Linear dimer	1.1±0.08	0.5±0.03	23±0.4	0.5±0.006
Meta dimer	0.99±0.06	0.54±0.03	12±0.2	0.46±0.005
Linear trimer	3.8±0.04	1±0.007		
Star trimer	8.4±0.06	1±0.005		
Energy gain by the bridging moieties				
Linear dimer	1.6±0.05	1±0.03		
Linear trimer	0.57±0.03	1±0.03		
Star trimer	4.0±0.1	1±0.02		

Table 4.3 Fitting parameters for the cooling of hot viologen units as well as the heating of the bridge moieties and the cold viologens. Energy gain by bridging moieties of meta dimer is absent due to poor fitting convergence.

Lastly, it is of interest to compare the behavior of the para (linear) vs meta bridged dimers and trimers. The linear dimer and trimer show qualitatively similar temporal profiles, with, as expected, the trimer equilibrating faster. Their meta bridged equivalents exhibit more distinct equilibration dynamics. The star trimer appears to lack the fast ~1 ps component which accounts for as much as ~60% of the relaxation in the dimer. Similarly as in the case

of the experimental results, this suggests that the redistribution of energy in the trimer is hampered by symmetry and vibrational interference between the branching pathways. Similar quantum interference effects were predicted theoretically for electron transfer in symmetric branched systems consisting of a single donor and multiple acceptors [22].

4.4 Electron transfer competes with a conical intersection in $MV^{+\bullet}-MV^{++}$ and $MV^{+\bullet}-MV^{+\bullet}$ dimeric viologens

4.4.1 Ground state absorption spectra

The ground state absorption spectra of both fully reduced and singly reduced dimers show very similar features as the absorption for monomeric $MV^{+\bullet}$ (Figure 4.10). Once again, it suggests that the interaction between the viologen sites is weak and the electronic states of interest remain localized on a single viologen unit. Calculations at the Hartree-Fock level carried out for the parent $MV^{++}-MV^{++}$ dimer also confirms that the electronic coupling between the relevant localized orbitals is in weak coupling range of ~ 11 to ~ 68 cm^{-1} , depending on the basis set.

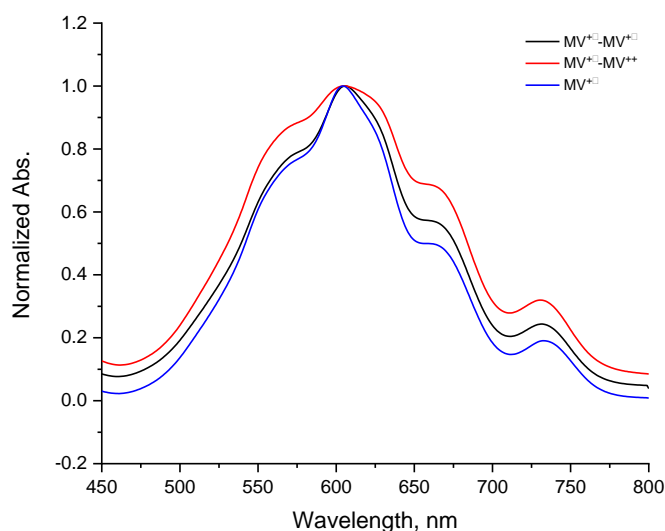


Figure 4.10 Normalized ground state absorption spectra of the $MV^{+\bullet}$ monomer (blue), the $MV^{+\bullet}-MV^{++}$ dimer (red) and $MV^{+\bullet}-MV^{+\bullet}$ dimer (black).

4.4.2 Pump-probe measurements

The excitation of the $MV^{+\bullet}$ leads to the formation of a short-lived D_1 state which is known to very rapidly decay back to the ground state D_0 as discussed in section 4.3.1. Figure 4.11 shows the transient kinetics at early time scales under three wavelengths probing ground state with different vibrational temperatures in monomeric $MV^{+\bullet}$ and the two dimers. The formation rates are gathered and compared in doubly reduced $MV^{+\bullet}-MV^{+\bullet}$ and singly reduced $MV^{+\bullet}-MV^{++}$ dimers in Table 4.4.

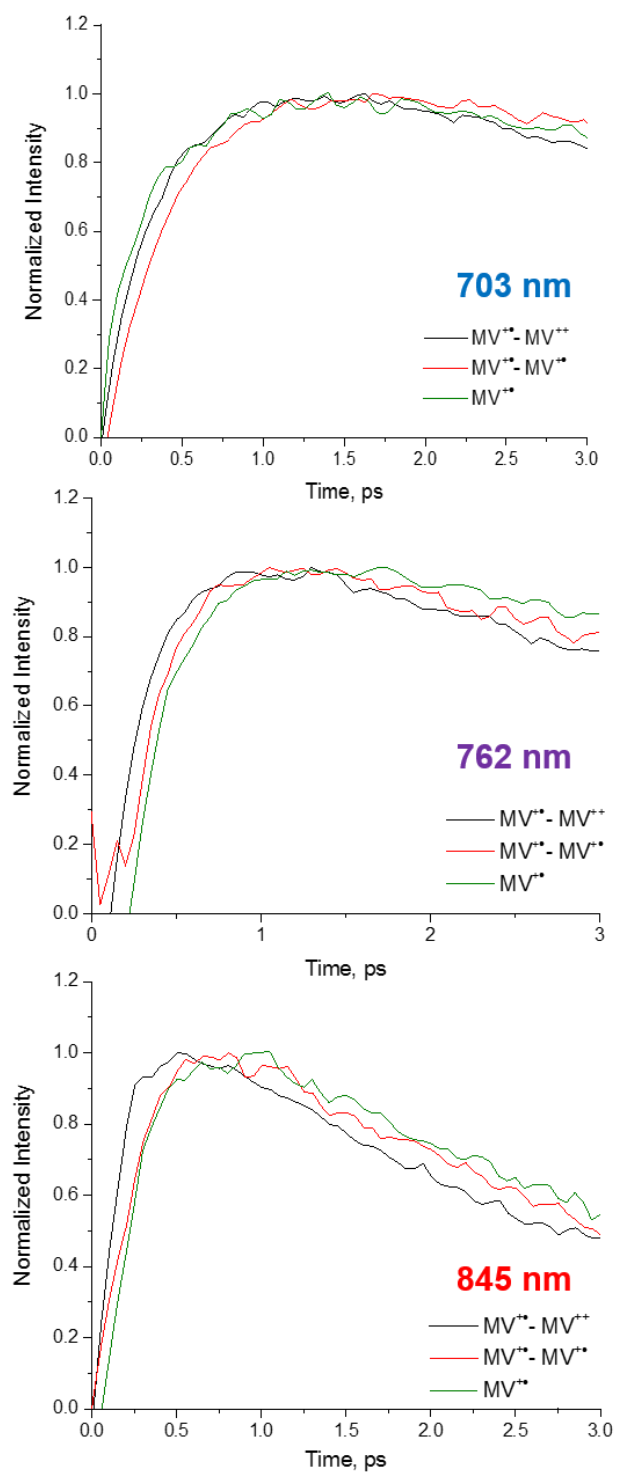


Figure 4.11 Transient decay kinetics at early times probed at 703, 762 and 845 nm.

The rates collected in Table 4.4 shows that regardless of the probe wavelength, the formation of the vibrationally hot ground state is always faster in the dimers than in the monomer possibly due to the higher density of state of the former. Furthermore, there is also a consistent difference in the rate of return to the ground state in the doubly versus singly reduced dimer with the latter exhibiting rates which are faster by 7.1×10^{11} to $1.4 \times 10^{12} \text{ s}^{-1}$ (~15 to 25 %), with the largest discrepancy occurring at the longest probe wavelength 845 nm, which corresponds to the hottest ground state molecules.

	703 nm	762 nm	845 nm
$MV^{+\bullet}, \text{ s}^{-1}$	$1.69 \pm 0.08 \times 10^{12}$	$1.85 \pm 0.07 \times 10^{12}$	$3.33 \pm 0.11 \times 10^{12}$
$MV^{+\bullet} - MV^{++}, \text{ s}^{-1}$	$2.08 \pm 0.04 \times 10^{12}$	$3.57 \pm 0.12 \times 10^{12}$	$5.56 \pm 0.29 \times 10^{12}$
$MV^{+\bullet} - MV^{\bullet\bullet}, \text{ s}^{-1}$	$1.79 \pm 0.07 \times 10^{12}$	$3.13 \pm 0.1 \times 10^{12}$	$4.17 \pm 0.32 \times 10^{12}$
$\Delta k_{decay}, \text{ s}^{-1}$	2.9×10^{11}	4.4×10^{11}	1.4×10^{12}

Table 4.4 The rates of the formation of the hot ground state in the studied viologen systems probed at several wavelengths. The Δk_{decay} is the difference between the hot ground state formation rate in $MV^{+\bullet} - MV^{++}$ and $MV^{+\bullet} - MV^{\bullet\bullet}$.

The formation of hot ground state in singly reduced dimer is likely to have accelerated by the competition between local IC in excited $MV^{+\bullet}$ moiety and photoinduced electron transfer to MV^{++} as discussed in 4.1. A similar fast photo-assisted electro hopping process was reported by Lu et al in oligomeric perylene diimide radical anions [23]. The empty orbitals contained by the unreduced MV^{++} moiety provide additional destinations for the electrons to hop, while it is impossible for doubly reduced dimers (Figure 4.12). The electron transfer may be as fast as $1.4 \times 10^{12} \text{ s}^{-1}$ (700 fs) from the Δk_{decay} gathered in Table

4.4, consistent with the estimated 290 fs based on the semi-classical Marcus-Jortner equation (Equation 1.27). All parameters including driving force, reorganization energy, most strongly coupled donor-acceptor vibrational frequency and electronic coupling between the viologen units are collected from DFT calculations carried by Spartan 18 (Wavefunction, Inc) at B3LYP 6-311+G** level. Most intriguing to us, the calculated result 290 fs is even faster than the experimental value of 700 fs, which not only confirms that the photoinduced electron transfer between $^*\text{MV}^{+\bullet}$ and MV^{++} accelerates the formation of hot ground state but also suggests that such channel may dominate the process in comparison with intramolecular internal conversion.

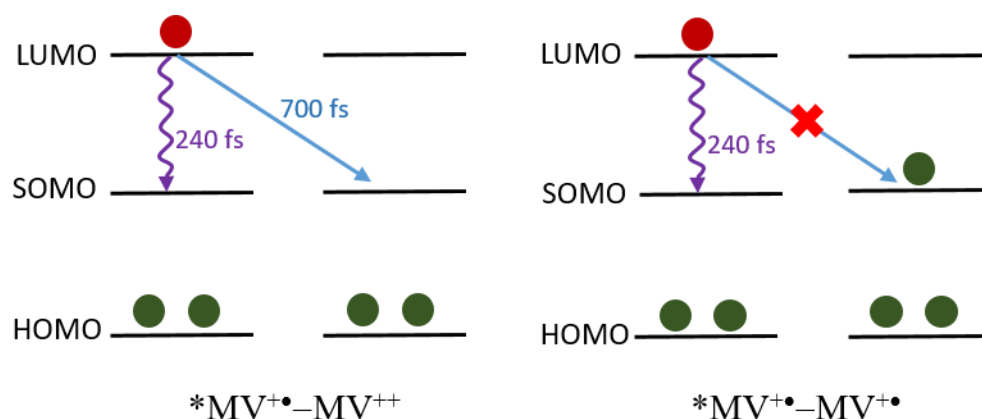


Figure 4.12 Schematic representation of the competing internal conversion (IC) and electron transfer (ET) deactivation pathways of the D_1 excited state in the mixed-valence $\text{MV}^{+\bullet} - \text{MV}^{++}$ and the doubly reduced $\text{MV}^{+\bullet} - \text{MV}^{+\bullet}$ redox form of the dimer.

It should be noted that there are two more electron transfer processes which are possible in the valence shell of $\text{MV}^{+\bullet} - \text{MV}^{++}$: the $\text{D}_0 - \text{S}_0 \leftrightarrow \text{S}_0 - \text{D}_0$ ground state hopping, which is intrinsically irrelevant to the deactivation of the excited state, as well as the $\text{LUMO} \leftrightarrow \text{LUMO}$ electron exchange, which in a mixed-valence system is synonymous with the $\text{D}_1 - \text{S}_1$

$\leftrightarrow S_1-D_1$ degenerate electronic energy transfer. These degenerate, $\Delta G^0 = 0$, ET processes have to overcome the full $\Delta G^* = \lambda/4$ activation barrier. As a consequence, they are both very slow, with estimated rates on the order of $1 \times 10^6 - 1 \times 10^7 \text{ s}^{-1}$ [17], i.e. several orders of magnitude too low to be of significance in the context of our observations.

Interestingly, when it comes to the vibrational redistribution and cooling of the hot ground state, the trend appears to be reversed. The doubly reduced dimer $MV^{+\bullet}-MV^{+\bullet}$ equilibrates faster than either the monomer or the mixed-valence species $MV^{+\bullet}-MV^{++}$.

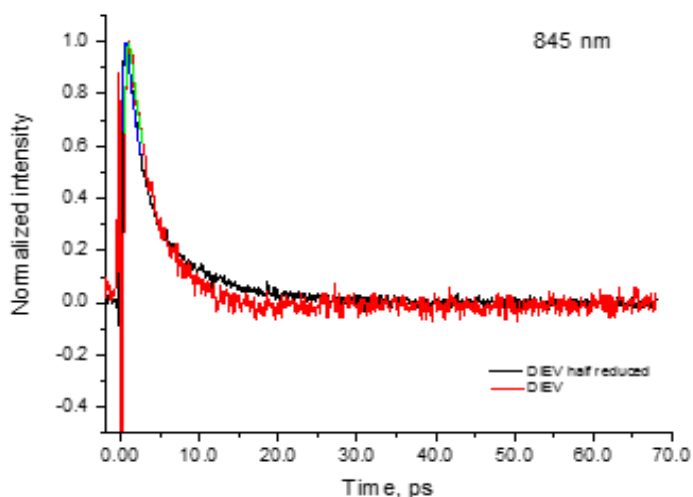


Figure 4.13 Transient decay profiles of $MV^{+\bullet}-MV^{+\bullet}$ and $MV^{+\bullet}-MV^{++}$.

In Table 4.5 we have gathered the cooling parameters obtained at the longest reliably measured wavelength of 845 nm, which probes the hottest population of the initially formed ground state and the result represents a combination of IVR and the early stages of energy dissipation to the solvent. The monomer and the mixed-valence $MV^{+\bullet}-MV^{++}$ exhibit strongly biexponential cooling, with the τ_1/τ_2 ratio of 4.1 - 5.6. In the mixed-valence dimer the biexponentiality is much less pronounced, with the fast-to-slow ratio of only 2.6.

This behavior suggests that temporal separation between the intramolecular redistribution and cooling to the solvent is not as clear in the symmetric $MV^{+\bullet}-MV^{+\bullet}$.

Species	A_1	τ_1 , ps	A_2	τ_2 , ps
$MV^{+\bullet}$, s ⁻¹	0.44±0.01	1.7±0.10	0.56±0.01	9.1±0.2
$MV^{+\bullet}-MV^{++}$, s ⁻¹	0.64±0.01	2.0±0.04	0.36±0.01	8.2±0.19
$MV^{++}-MV^{+\bullet}$, s ⁻¹	0.16±0.01	1.4±0.71	0.84±0.01	3.6±0.24

Table 4.5 Kinetic parameters of the cooling of the hot ground state probed at 845 nm for monomer, para dimer and meta dimer.

We attribute this behavior to the perfect vibrational frequency matching between the identical viologen sites in $MV^{+\bullet}-MV^{+\bullet}$, which facilitates ballistic propagation of the excess energy in the ground state of the dimer, as it was seen in section 4.3.1 and other work [13, 24]. As a result, the IVR within the originally excited hot viologen unit and vibrational energy transfer to the cold viologens are both rapid and temporally not well separated from one another. In contrast, in the mixed-valence compound, the geometry of the viologen moieties is different. The $MV^{+\bullet}$ has a nearly planar quinonoid configuration, while MV^{++} exhibits the twisted structure of biphenyl (Figure 4.4). The resulting vibrational frequency mismatch between critical skeletal modes of the viologen sites in the $MV^{+\bullet}-MV^{++}$ is on the average only ~ 10 cm⁻¹ and just a few cases of the most affected force constants reaches 50 cm⁻¹. Nevertheless, this modest mismatch appears to be sufficient to reduce the ballistic component of the vibrational energy redistribution in the mixed valence dimer.

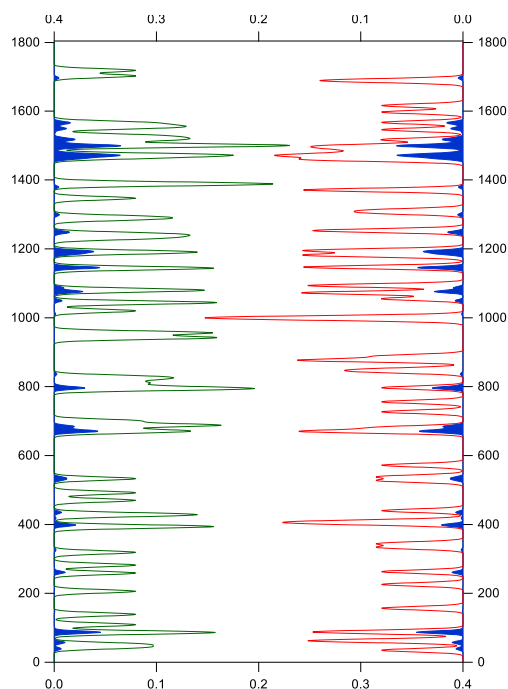


Figure 4.14 Vibrational frequency matching between $MV^{+\bullet}$ (green line on the left) and MV^{++} (red line on the right) normal modes based on B3LYP, 6-31G** calculations (Spartan '16). The frequency overlap based on an arbitrary 15 cm^{-1} linewidth is shown in solid blue on both sides of the graph. The high frequency CH stretching modes are of minor relevance to the cooling process and were not included.

4.5 Conclusions

The redistribution of vibrational energy undergoes acceleration upon the addition of viologen units to the monomer and points to a major ballistic component of the process. Perhaps most interestingly, equilibration in the branched star trimer is considerably slower than in its linear counterpart. The dependence on the branching topology reinforces the

notion of non-stochastic nature of the redistribution of process and suggests that the skeletal modes propagate ballistically along the oligomer backbone. Branching in the meta linked star trimer leads to mode degeneracies and imposes symmetry barriers on the ballistic propagation. Molecular dynamics simulations carried out within the harmonic approximation corroborate the importance of ballistic effects and the significant influence of topology on the propagation of vibrational excess energy in these systems. These findings have fascinating implications for electron transfer processes in donor-acceptor systems in which one or both partners are far from thermal equilibrium, for example in the dendritic networks of electron acceptors which were recently studied by this group.¹⁸ Depending on the details of the electronic coupling and the driving force, ballistic propagation of vibrational excitation may allow the heat front to propagate along the system considerably faster than the tunneling or hopping electron, thus dynamically altering the effective local temperature for the electron transfer event.

The observed apparent acceleration of internal conversion in the covalently bridged $MV^{+\bullet}-MV^{++}$ mixed valence dimer due to the $*MV^{+\bullet}-MV^{++} \rightarrow MV^{++}-MV^{+\bullet}$ electron transfer is likely to be a general phenomenon in similar open shell systems, regardless of the specific IC mechanism in the monomeric unit. The magnitude of the effect will be determined by the relative rates of internal conversion in the monomer and electron transfer between the coupled units. When the excited state lifetime of the monomer is long and the electron transfer fast, the latter may become the dominant channel of return to the ground state. Separately, the redistribution of the excess vibrational energy appears to be slower in the mixed valence dimer than in the corresponding fully symmetric, doubly reduced species. This is attributed to the vibrational frequency mismatch between the sites and hence

reduced efficiency of the ballistic propagation of the excess energy across the dimeric system.

References

1. Felker, P.M. and A.H. Zewail, *Dynamics of intramolecular vibrational-energy redistribution (IVR). II. Excess energy dependence*. The Journal of Chemical Physics, 1985. **82**(7): p. 2975-2993.
2. Felker, P.M. and A.H. Zewail, *Dynamics of intramolecular vibrational-energy redistribution (IVR). I. Coherence effects*. The Journal of Chemical Physics, 1985. **82**(7): p. 2961-2974.
3. Nesbitt, D.J. and R.W. Field, *Vibrational energy flow in highly excited molecules: role of intramolecular vibrational redistribution*. The Journal of Physical Chemistry, 1996. **100**(31): p. 12735-12756.
4. Schwarzer, D., et al., *Intramolecular vibrational energy redistribution in bridged azulene-anthracene compounds: Ballistic energy transport through molecular chains*. The Journal of Chemical Physics, 2004. **121**(4): p. 1754-1764.
5. Uzer, T. and W.H. Miller, *Theories of intramolecular vibrational energy transfer*. Physics Reports, 1991. **199**(2): p. 73-146.
6. Segal, D. and B.K. Agarwalla, *Vibrational heat transport in molecular junctions*. Annual Review of Physical Chemistry, 2016. **67**(1): p. 185-209.
7. Chen, G., *Ballistic-diffusive equations for transient heat conduction from nano to macroscales*. Journal of Heat Transfer, 2002. **124**(2).
8. Shiomi, J. and S. Maruyama, *Molecular dynamics of diffusive-ballistic heat conduction in single-walled carbon nanotubes*. Japanese Journal of Applied Physics, 2008. **47**(4): p. 2005-2009.

9. Wurzer, A.J., et al., *Comprehensive measurement of the S_1 azulene relaxation dynamics and observation of vibrational wavepacket motion*. Chemical Physics Letters, 1999. **299**(3-4): p. 296-302.
10. Hochstrasser, R.M. and C.A. Nyi, *Resonance fluorescence, Raman spectra and relaxation of single vibronic levels in the condensed phase: Azulene in naphthalene*. The Journal of Chemical Physics, 1979. **70**(3): p. 1112-1128.
11. Wild, W., et al., *Ultrafast investigations of vibrationally hot molecules after internal conversion in solution*. Chemical Physics Letters, 1985. **119**(4): p. 259-263.
12. Kurnosov, A.A., I.V. Rubtsov, and A.L. Burin, *Communication: Fast transport and relaxation of vibrational energy in polymer chains*. The Journal of Chemical Physics, 2015. **142**(1).
13. Rubtsova, N.I., et al., *Room-temperature ballistic energy transport in molecules with repeating units*. The Journal of Chemical Physics, 2015. **142**(21).
14. Pecourt, J.-M.L., J. Peon, and B. Kohler, *DNA excited-state dynamics: ultrafast internal conversion and vibrational cooling in a series of nucleosides*. Journal of the American Chemical Society, 2001. **123**(42): p. 10370-10378.
15. Cahill, D.G., et al., *Nanoscale thermal transport*. Journal of Applied Physics, 2003. **93**(2): p. 793-818.
16. Rubtsova, N.I., et al., *Ballistic energy transport in oligomers*. Accounts of Chemical Research, 2015. **48**(9): p. 2547-2555.

17. Gong, Z., et al., *Generation dependent ultrafast charge separation and recombination in a pyrene-viologen family of dendrons*. The Journal of Physical Chemistry B, 2016. **120**(18): p. 4286-4295.
18. Myahkostupov, M., et al., *Vibrational state dependence of interfacial electron transfer: hot electron injection from the S_1 state of azulene into TiO₂ nanoparticles*. The Journal of Physical Chemistry C, 2013. **117**(40): p. 20485-20493.
19. Monk, P.M.S., *The viologens : physicochemical properties, synthesis, and applications of the salts of 4,4'-bipyridine*. 1998, Chichester ; New York: Wiley. xix, 311 p.
20. Huang, Y. and J.B. Hopkins, *Femtosecond resonance raman investigation of four univalent bipyridinium radicals*. The Journal of Physical Chemistry, 1996. **100**(23): p. 9585-9591.
21. Häupl, T., R. Lomoth, and L. Hammarström, *Femtosecond dynamics of the photoexcited methyl viologen radical cation*. The Journal of Physical Chemistry A, 2003. **107**(4): p. 435-438.
22. Risser, S.M., D.N. Beratan, and J.N. Onuchic, *Electronic coupling in starburst dendrimers: connectivity, disorder, and finite size effects in macromolecular Bethe lattices*. The Journal of Physical Chemistry, 1993. **97**(17): p. 4523-4527.
23. Lu, C., et al., *Unprecedented intramolecular electron transfer from excited perylenediimide radical anion*. The Journal of Physical Chemistry C, 2016. **120**(23): p. 12734-12741.

24. Liu, M., et al., *Vibrational cooling in oligomeric viologens of different sizes and topologies*. The Journal of Physical Chemistry B, 2019. **123**(8): p. 1847-1854.

Chapter 5. Excited state dynamics of an anthracenylboronic compound

5.1 Introduction

In the past decade, π -conjugated polymers and molecules have drawn great attention among chemists due to their metal-like properties which enable the design of new materials for potential applications in optoelectronics and organic light-emitting diodes (OLEDs). In particular, the incorporation of main group elements such as boron, nitrogen and silicon can allow further tuning of the electronic properties of these molecules [1, 2]. For example, in some polyboroles and polysiloles, the LUMO energy level can be significantly lowered due to effective interactions between the vacant p or σ^* orbitals of the boron or silicon atoms and π^* orbital of the π -conjugated system [3, 4]. In other π -conjugated molecules containing four coordinated boron or boron clusters, second order nonlinear optical properties were discovered [5, 6]. In this context, it is even more intriguing if two main group elements that exhibit donor-acceptor properties are incorporated into the π -conjugated systems. An intensely studied example is boron-nitrogen compounds. Depending on the number of substituents and the bond order of the B-N bond, boron-nitrogen compounds can be classified into three types: borazanes, borazenes and borazines [7, 8].

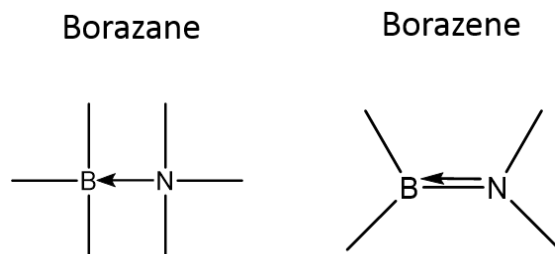


Figure 5.1 Structure of amine-borane adduct and aminoborane.

Borazanes contain tetravalent boron atom bound to a tetravalent nitrogen atom by two unshared electrons on nitrogen. The structure is roughly comparable to alkanes, where the two carbon atoms are linked by a single bond. A known property of amine-borane is the conformational change from staggered to eclipsed form upon photoexcitation.

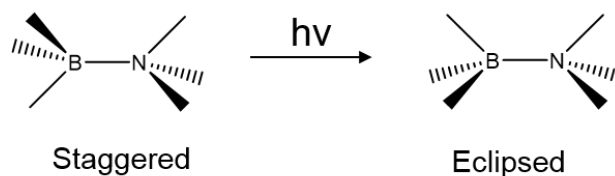


Figure 5.2 Conformational change of amine-borane upon photoexcitation.

In borazenes, boron and nitrogen atoms are linked by one covalent σ -bond. The two unshared electrons on nitrogen atom also participate in the bonding, therefore, the B-N bond in borazenes exhibits certain degree of double bond character. In this sense, borazenes are very similar to alkenes. Borazene compounds can also undergo geometry change that is closely related to the B-N bond twisting relaxation after photoexcitation. This could lead to charge transfer emission with an unusually large Stokes shift [7, 9-11].

In this work, the excited state dynamics as well as charge transfer properties of a borazene compound bisanthryboryldiphenylamine containing sterically crowded anthracene groups

were carefully studied by steady state fluorescence spectroscopy, pump-probe spectroscopy together with theoretical modeling utilizing semi-classical Marcus-Jortner equation. The structure of the molecule is shown in Figure 5.3. For simplicity, from this point on, the molecule will be referred as BN. The B-N bond in BN exhibits approximately 36% double bond character with a dihedral angle of 17.4 degrees between diagonal phenyl ring and anthracene group according to DFT calculations at B3LYP, 6-31G* level.

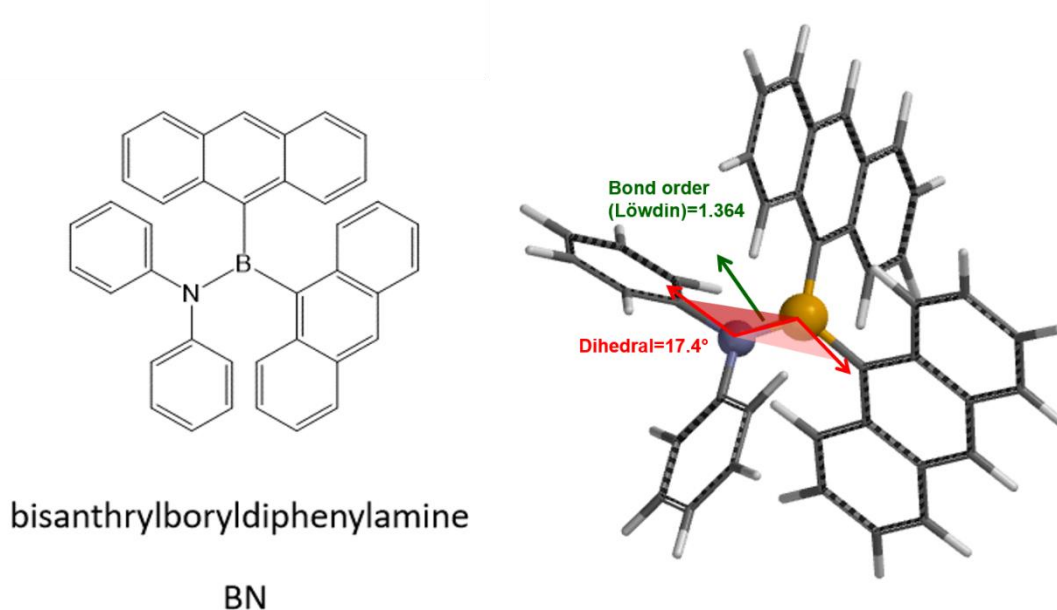


Figure 5.3 Structure of the BN molecule.

Ground state energy of BN was calculated and plotted with respect to dihedral angle and the bond order of the B-N bond. The correlation between the order of the B-N bond and the dihedral angle appears to be nearly linear (Figure 5.4 blue projection curve). At zero degrees, the B-N bond exhibits the highest double bond character, while at larger dihedral angles of about 30 degrees, the bond order decreases by about 5%. The overall energy change of 0.05 eV, however, is modest considering the 30 degree twist. This suggests

relatively easy change of bond order in the BN molecule. The small change of energy also implies that BN may exhibits a wide range of twist angles at room temperature in solution. The distribution of rotamers may be very sensitive to the influence of varying the solvent.

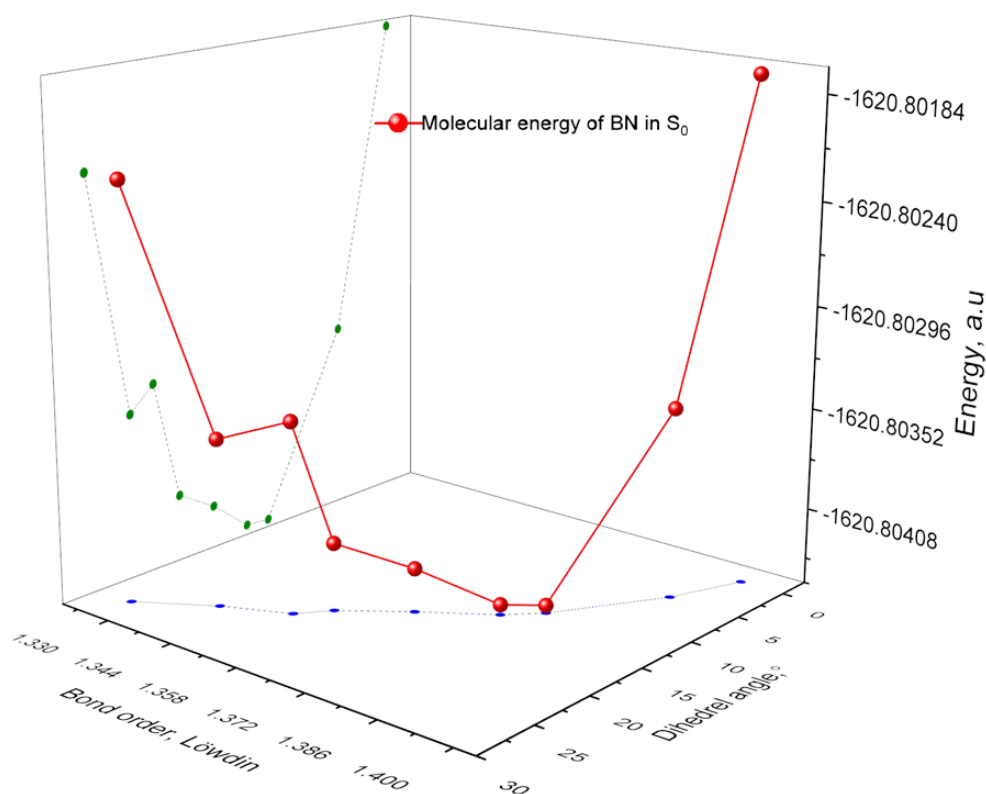


Figure 5.4 3D plot of the ground state energy of BN plotted as a function of the dihedral angle and the B-N bond order.

5.2 Sample preparation

This project is carried out in collaboration with Prof. Thilagar at the Indian Institute of Science. The BN molecule is used directly as received. All solvents used in this work are HPLC grade. The concentration of each solution was approximately 1×10^{-5} M.

5.3 Results and discussion

5.3.1 Steady state absorption

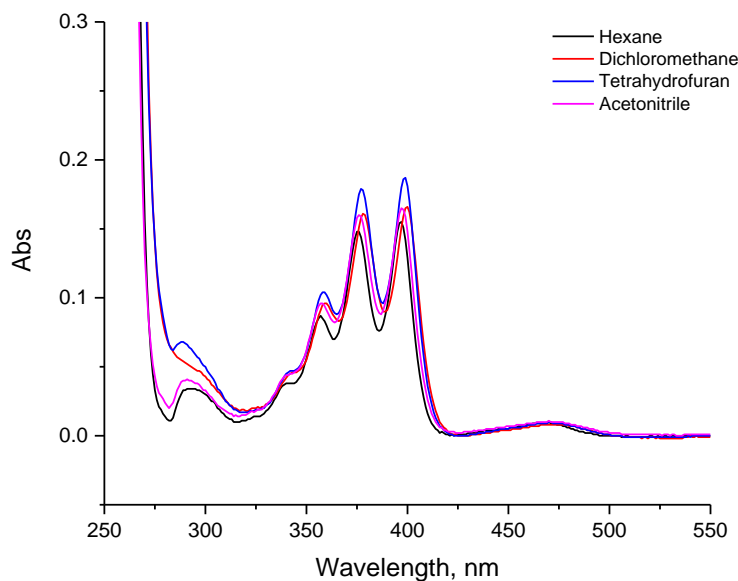


Figure 5.5 UV-Vis spectra of BN in different solvents.

The UV-VIS spectrum of BN shows two regions of absorption: the 400 nm region exhibits signature features of anthracene absorption and the band around 470 nm is assigned to charge transfer state of BN. We carried out a series of DFT calculations at B3LYP 6-31G level in order to simulate the UV-VIS spectrum and decompose the transition into orbital contributions. The results show three bands centered at 335 nm, 404 nm and 431 nm.

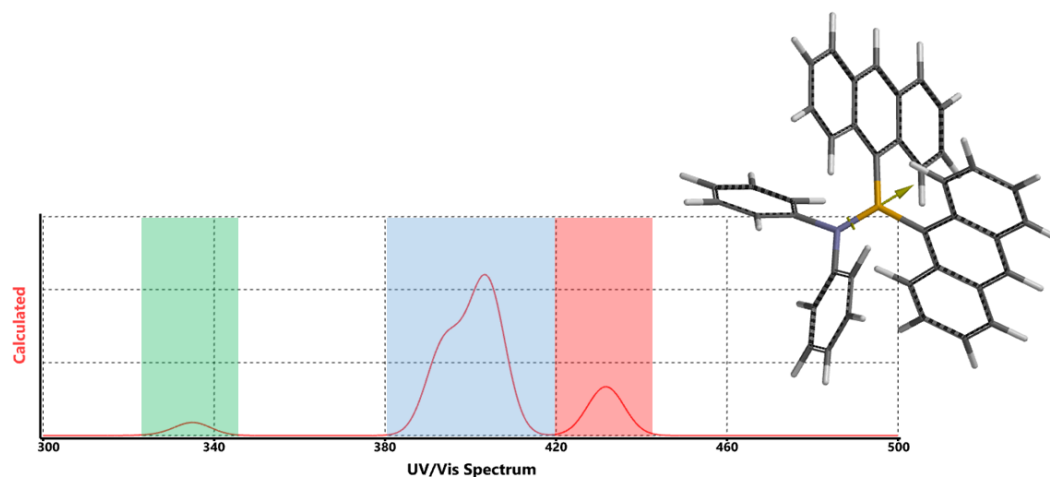


Figure 5.6 Simulated UV-VIS spectrum of BN in vacuum.

Based on the analysis of the orbital composition for each absorption band, the 335 nm peak originates from the charge transfer between the diphenylamine and one of the anthracenes, and consists almost completely of the HOMO-2 to LUMO transition. The electron density shifts entirely from the nitrogen atom and its substituents to the anthracene groups. This corresponds to charge transfer from the nitrogen side to boron side of BN molecule. However, this band is hidden beneath the strong anthracene absorption in the experimental UV-VIS spectrum. The 404 nm band consists of 80% HOMO to LUMO+1 transition, which is localized only on the anthracene groups and confirms the anthracene-like absorption at these wavelengths. The minor component of 20% is dominated by the HOMO-1 to LUMO transition, which exhibits some charge transfer character from anthracene groups to boron and nitrogen atoms. As for 431 nm band, the major component (~80%) is the transition from the HOMO to LUMO orbital, which clearly shows an electron density shift from the anthracene groups to boron atom. The remaining 20% of 431 nm band is dominated by the HOMO-1 to LUMO+1 transition that once again points to

anthracene-like absorption. Based on these results, we concluded that the 475 nm charge transfer band observed in the experimental UV-VIS spectrum originates from a relatively small electron density shift from anthracene groups to the boron atom instead of a complete charge transfer between boron and nitrogen atom. Indeed, the calculations show an increase of electron density on the boron of 2.68%, while the electron density on nitrogen decreases by a minor amount of 0.37%, confirming that the primary charge shift in this molecule is from anthracene to boron.

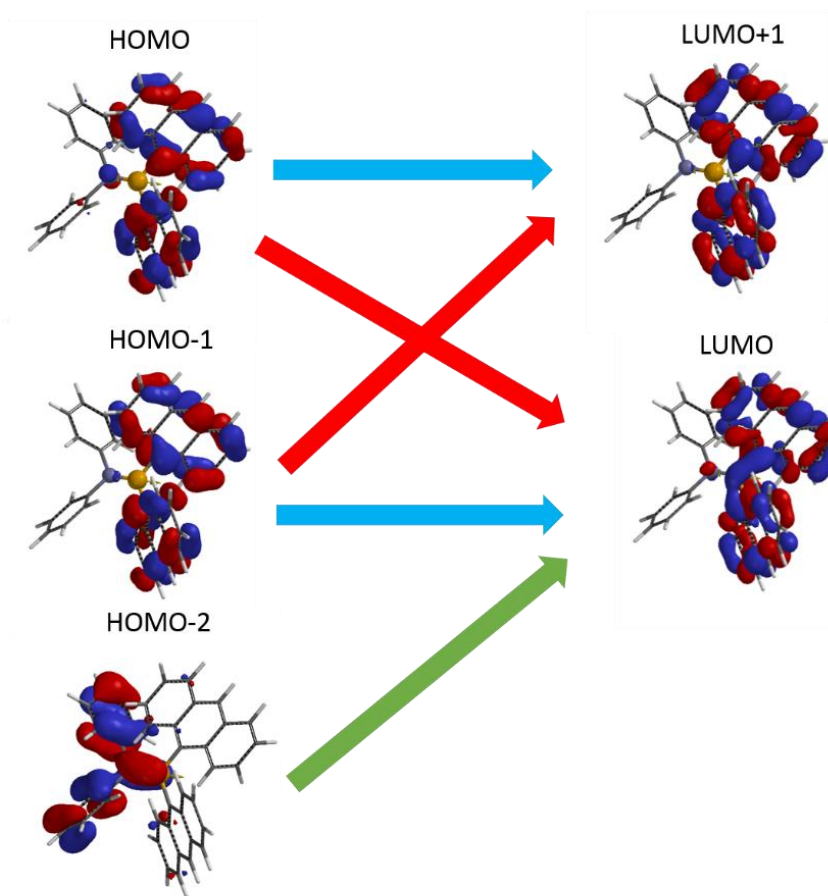


Figure 5.7 Molecular orbitals of BN with arrows indicating the contributions to the low-lying electronic transitions.

Center wavelength, nm	Orbital components	Weight
335	HOMO-2 to LUMO	97%
404	HOMO to LUMO+1	80%
	HOMO-1 to LUMO	19%
431	HOMO to LUMO	77%
	HOMO-1 to LUMO+1	23%

Table 5.1 Molecular orbital composition of the calculated absorption bands of BN.

The color shading corresponds to the transitions indicated in Figure 5.7.

The origin of 475 nm “charge shift” band is also confirmed by Figure 5.8, which shows the calculated B-N bond lengths plotted versus the dihedral angle with green stars labeling the optimum geometries in the S_0 and S_1 state of BN molecule. From the plot, it is observed that the B-N bond elongates upon photo excitation, which points to a higher single bond character in S_1 state of BN. Therefore, it is possible for the empty p orbital of boron atom to receive more contribution of electron density from adjacent anthracenes instead of nitrogen atom.

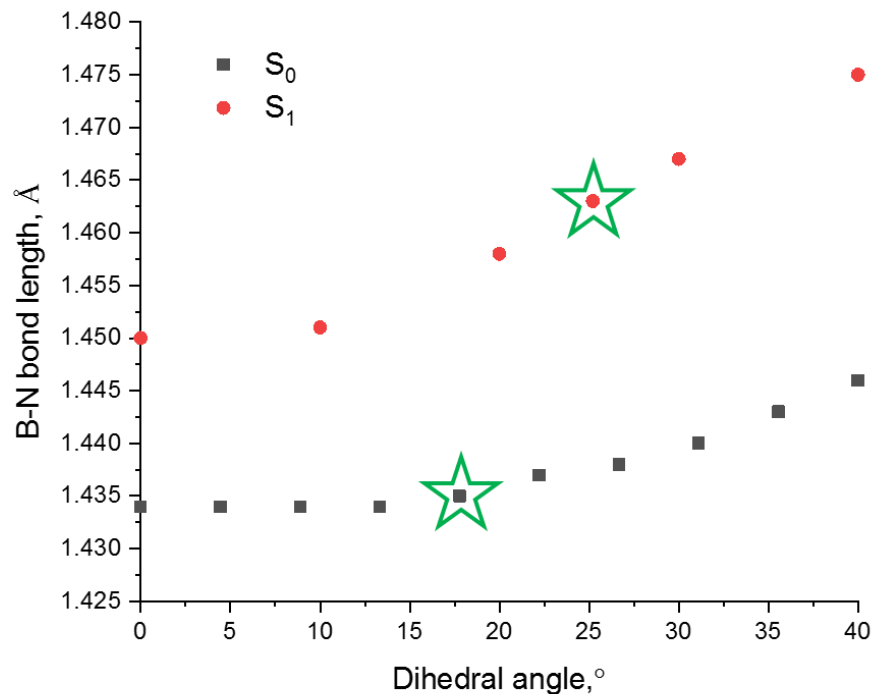


Figure 5.8 Calculated B-N bond lengths with respect to different dihedral angles in the S₀ and the S₁ of BN. Green stars show the optimum B-N bond length and the dihedral angle at both states.

From the spectra and MO calculation results, it appears that the nitrogen atom and its substituents play a very subtle role in determining the optical properties of the BN molecule, especially the “charge shift” band at 475 nm.

It is reasonable to carry out additional measurements on reference samples containing only anthracene and boron groups to compare the spectroscopic features. Three reference molecules were selected: 9-methylanthracene, 9-anthracene boronic acid and 9,10-anthracenediboronic acid bis(pinacol) ester. The UV-Vis spectra for all three reference molecules show very similar yet slightly shifted bands around 300-400 nm featuring

anthracene absorption. None of the reference samples shows a sign of a charge transfer/shift band around 475 nm, even though the HOMO and LUMO orbitals of 9-anthracene boronic acid also exhibit electron density shift from anthracene to boron atom (Figure 5.9).

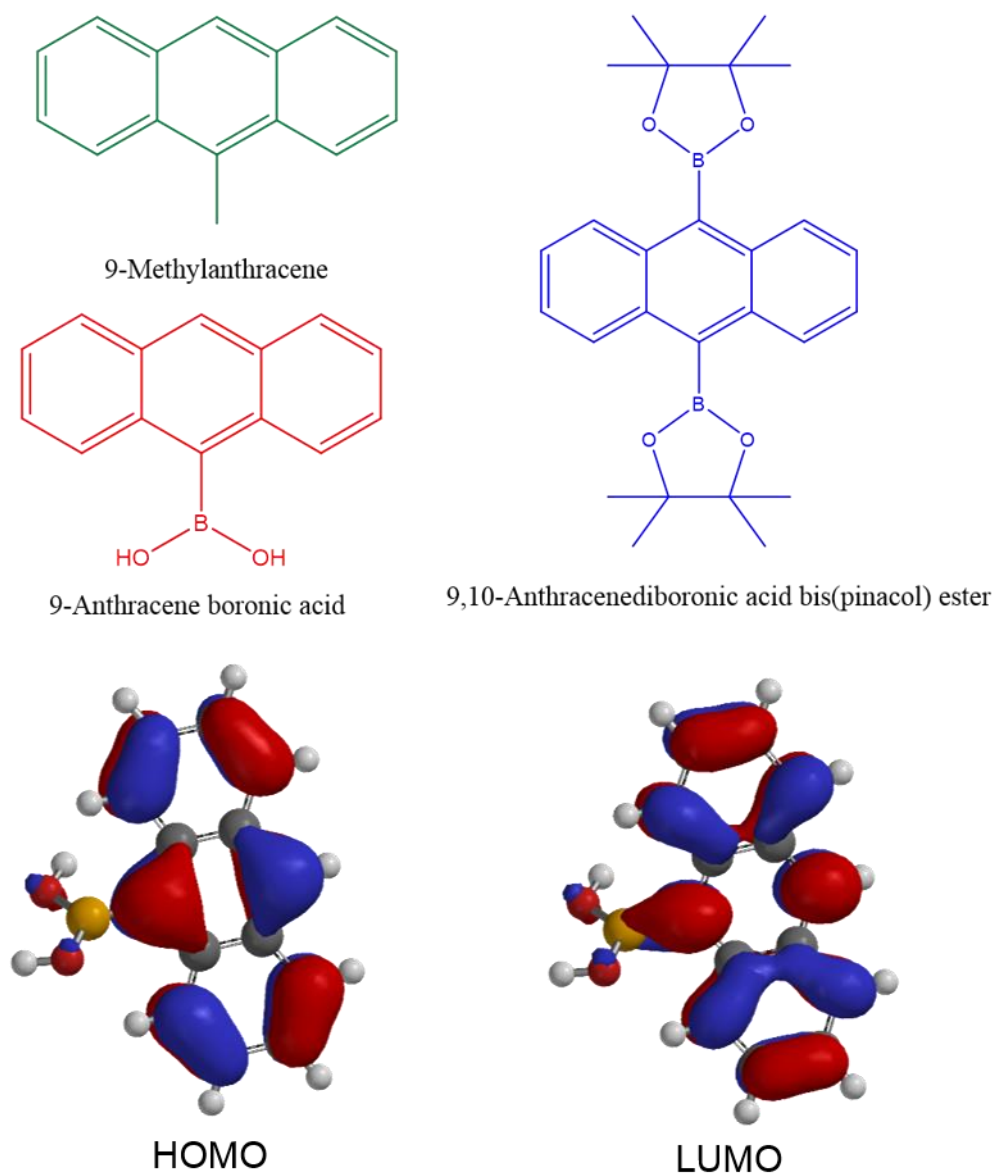


Figure 5.9 Structures of the reference molecules and the HOMO, LUMO orbitals for 9-anthracene boronic acid.

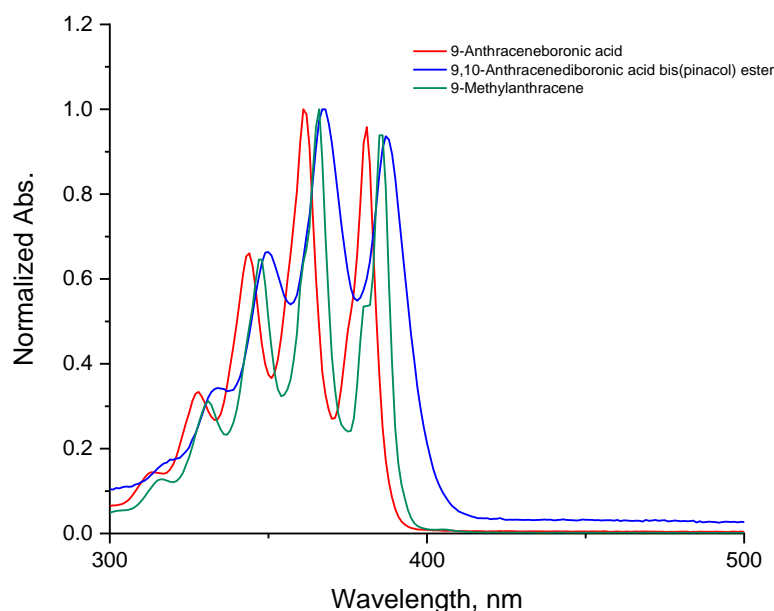


Figure 5.10 UV-Vis spectra of the reference molecules in hexane.

The measurements on these reference samples offer important hints as to the appearance of the “charge shift” band in BN. Two possible reasons are postulated. First of all, the presence of two anthracene groups in BN molecule facilitate the charge shift between the anthracenes and the boron atom. The LUMO orbital is delocalized on these two anthracenes and therefore lowered the transition energy. Second, the sterical crowding in the BN molecules may also be vital. With the participation of two anthracene groups and two phenyl groups on the nitrogen side, any geometry change of BN in S_1 could be difficult. Therefore, the pre-twisted conformation that favors the charge shift between the anthracenes and the boron atom can be easily maintained.

5.3.2 Charge transfer emission of BN

Excitation of the 475 nm band of BN leads to strong charge transfer fluorescence in the emission spectrum shown in Figure 5.11. The weaker peak at around 420 nm corresponds

to the local anthracene fluorescence, while the strong band around 520 nm originates from the charge transfer state. Solvent dependence of the fluorescence was investigated by direct excitation of charge transfer band at 467 nm in seven solvents with different polarity. The resulting spectra are plotted in Figure 5.12. As the solvent polarity increases, the charge transfer emission of BN is dramatically quenched. In addition, there is a moderate red shift of the peak in more polar solvents.

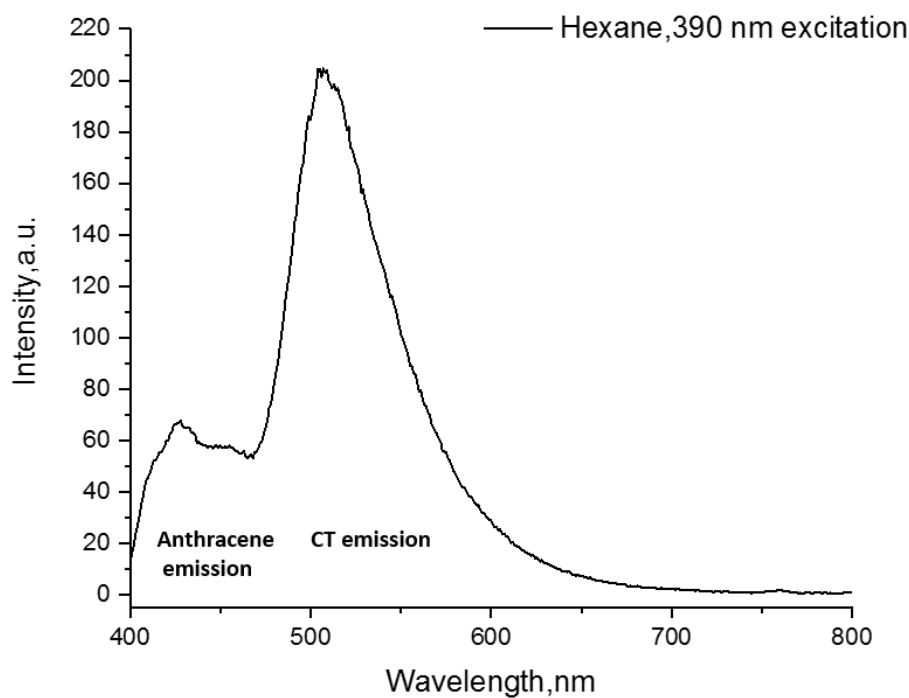


Figure 5.11 Emission spectrum of BN in hexane.

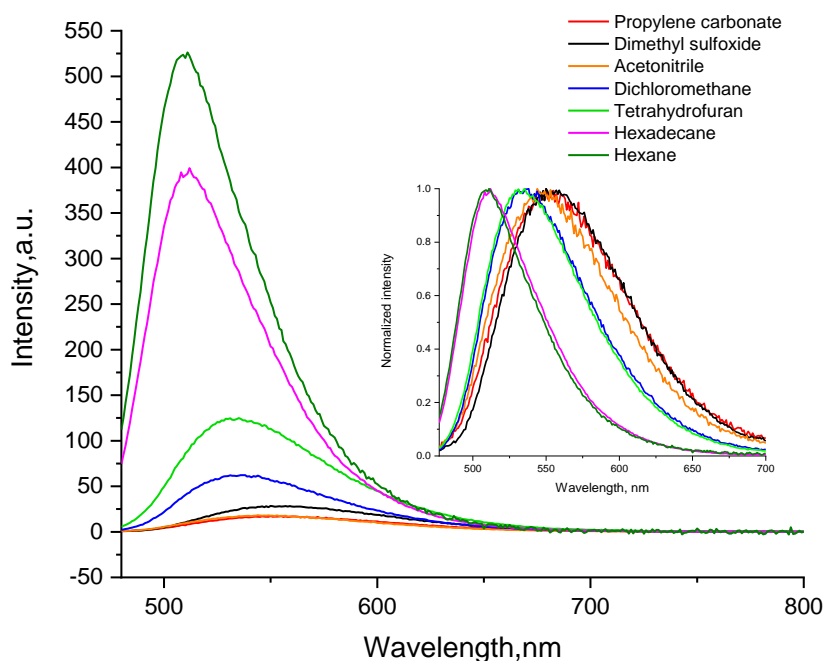


Figure 5.12 Charge transfer emission spectra of BN in different solvents. Inset: Normalized charge transfer emission spectra of BN.

To better understand these trends, Marcus-Jortner equation (Equation 5.1) for charge transfer emission is applied and fitted to all spectra to obtain driving forces and solvent reorganization energies. This equation describes the radiative charge recombination process between boron atom (donor) and anthracene groups (acceptor),

$$I_{(v)} = \frac{2\pi}{\hbar} V^2 \frac{1}{\sqrt{4\pi k_B T}} \sum_{i=0}^{\infty} \exp(-S) \frac{S^i}{i!} \exp \left[-\frac{(\Delta G_0 + \lambda_S + i\hbar\nu_V + \hbar\nu)^2}{4\lambda k_B T} \right] \quad (5.2)$$

where $S = \frac{\lambda_{inner}}{\hbar\nu_V}$. The summation is carried out from $i = 0$ to $i = 2$. The internal reorganization energy $\lambda_{inner} = 0.07 \text{ eV}$ was obtained by fitting of emission spectrum of BN in hexane. The small value for λ_{inner} confirms once more that the charge separation and recombination in BN amounts to a slight electron density shift between anthracene

groups and the boron atom. As a result, the geometry change of both donor and acceptor should be relatively subtle. The in-plane skeletal breathing mode is selected for the most strongly coupled donor-accepter vibrational frequency with $\nu_V = 1330 \text{ cm}^{-1}$ obtained from calculated IR spectrum.

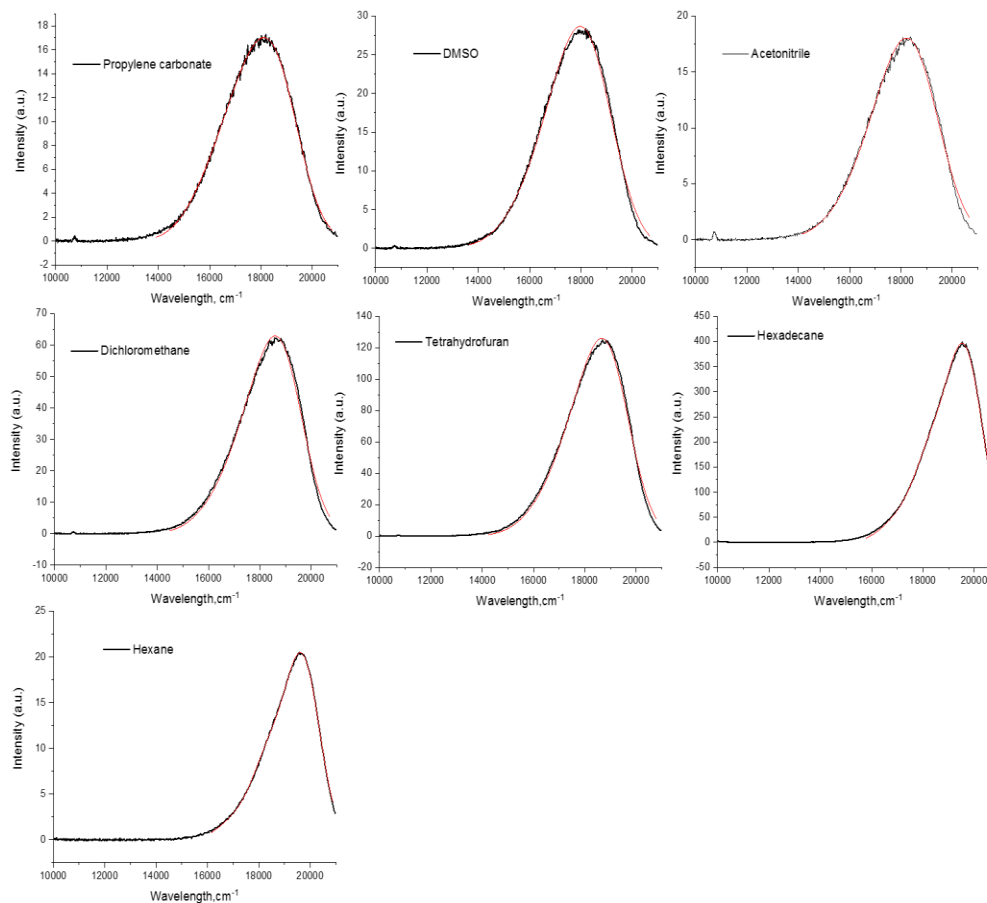


Figure 5.13 Charge transfer emission spectra of BN in various solvents and the corresponding fits by the Marcus-Jortner equation.

The fitting results are summarized in Table 5.2. The driving force in all seven solvents changes remarkably little, with the maximum difference of less than 400 cm^{-1} . The solvent reorganization energies in general increased as the solvent became more polar, however,

there are a few discrepancies in this trend. From acetonitrile to propylene carbonate, the solvent reorganization energy decreased by about 600 cm^{-1} even though the dielectric constant was almost doubled. This can be explained by the two-sphere model for solvent reorganization energy (Equation 1.26), which also takes into account the influence of refractive index. With other parameters being the same, the solvent reorganization energy should be linearly dependent on the difference between $\frac{1}{n_s^2}$ and $\frac{1}{\epsilon_s}$. If this difference is defined as parameter $A = \frac{1}{n_s^2} - \frac{1}{\epsilon_s}$, the value of A for all seven solvents agrees very well with the trend of solvent reorganization energies, except DMSO and propylene carbonate. The viscosity of the solvent also plays an important role in determining the solvent reorganization, albeit when it comes to the dynamics rather than energetics of the process. In more viscose solvent like propylene carbonate, the motions of solvent molecules are slower than in DMSO, not to mention that the propylene carbonate is a bigger molecule than DMSO. The molar volume of DMSO is $71.1 \pm 3\text{ cm}^3$, while the molar volume of propylene carbonate is $87.3 \pm 3\text{ cm}^3$ (values predicted by ADC/Labs). Therefore, it is reasonable that the apparent solvent reorganization energy in propylene carbonate maybe smaller than in DMSO.

Solvent	Maxima/ cm^{-1}	$\Delta G_0/\text{cm}^{-1}$	λ/cm^{-1}	ϵ	n^{20}	A	η/mPas
Hexane	19569	-20780 ± 8	1072 ± 8	1.89	1.38	0	0.33
Hexadecane	19531	-20795 ± 10	1151 ± 10	2.09	1.43	0.01	3.00
Tetrahydrofuran	18692	-20791 ± 30	1895 ± 29	7.40	1.41	0.36	0.55
Dichloromethane	18587	-20723 ± 5	1886 ± 5	8.93	1.42	0.39	0.43
Acetonitrile	18382	-21261 ± 40	2731 ± 38	37.5	1.34	0.53	0.37
Dimethyl sulfoxide	18215	-20872 ± 33	2595 ± 32	46.7	1.48	0.44	2.24
Propylene carbonate	18215	-20760 ± 2	2139 ± 2	64.0	1.42	0.48	2.53

Table 5.2 Charge transfer fluorescence fitting parameters obtained by using the Marcus-Jortner equation.

The driving force is a function of the magnitude of the transition dipole moment, while the solvent reorganization energy is related both to the magnitude and the orientation (Equation 5.2). Therefore, the nearly constant driving force recovered from fitting suggests that the magnitude of the transition dipole moment does not change much in different solvents ($\Delta|\vec{\mu}| = 0$). The substantial change in the solvent reorganization energy in response to varying polarity indicates the change in orientation of dipole moment in all solvents.

$$\begin{aligned}\Delta G_0 &= f(|\vec{\mu}_1| - |\vec{\mu}_0|) \\ \lambda_s &= f(|\vec{\mu}_1 - \vec{\mu}_0|)\end{aligned}\tag{5.2}$$

From the DFT calculations, the dipole moment of BN in S_0 state is pointing from nitrogen to boron. In the S_1 state, the dipole moment almost completely reverses, pointing from anthracene to the boron as shown in Figure 5.14 ($\vec{\mu}_1 \approx -\vec{\mu}_0$). Therefore, it was concluded that the change in charge transfer emission spectrum in all solvents originates from the change in the orientation of the dipole moment and the associated reorganization energy, which also explains the relatively small red shift of the fluorescence spectrum in increasing polar solvents.

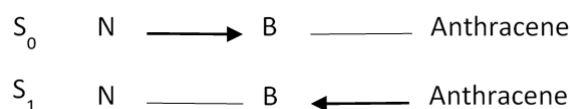


Figure 5.14 Schematic diagram showing the change of dipole moment orientation with arrows in BN molecule.

Based on the fitting parameters, it is observed that the absolute value of driving force is much larger than solvent reorganization energy. As shown in Figure 1.10 presenting the Marcus parabola and the three regions defined by the Marcus theory, the radiative charge

recombination process from S_1 to S_0 of BN lies in the Marcus inverted region. Therefore, the charge recombination rate accelerates as λ_s increases. In other word, the charge transfer fluorescence quenches in more polar solvents. The above analysis corroborates very well with the experimental results that the fluorescence intensity in propylene carbonate decreased approximately 96% in comparison with the fluorescence intensity in hexane.

5.3.3 Transient absorption measurements

Pump-probe spectroscopy was applied to study the transient species of BN in both acetonitrile and hexane. Two excitation wavelengths, 390 nm and 450 nm were used. When exciting at 390 nm, anthracenes in BN are excited to the presumably localized singlet excited state S_A . According to the DFT calculation of the relevant energy levels in BN (Figure 5.15), the transition to the charge separated/shifted S_1 state is possible. Upon 450 nm excitation, the charge separated/shifted state S_1 is directly populated, followed by possible intersystem crossing to triplet state of BN. Therefore, these three states are expected to dominate the transient absorption spectrum of BN.

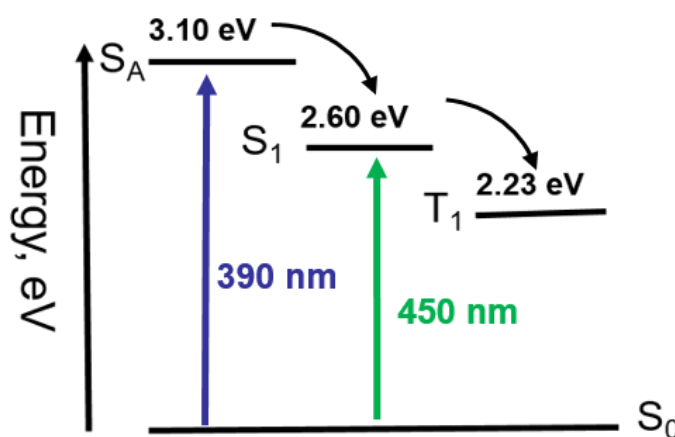


Figure 5.15 Energy level diagram of BN obtained by DFT calculations.

As shown in the 2D transient absorption map, the excited state of anthracene S_A gives rise to a broad band around 550-650 nm (Figure 5.17a,c). In acetonitrile, the band is broader than in hexane. When BN is excited with 450 nm light, the transient absorption spectra in acetonitrile show two very long-lived bands centered at 550 nm and 700 nm (Figure 5.16 b,d). Since the lifetimes of these two peaks are very similar, they should originate from the same electronic state, which we assigned it to the absorption by T_1 state in BN. The T_1 state of BN is very similar to the triplet state of anthracene. As shown in Figure 5.16, the spin density of BN calculated by DFT localize almost entirely on the anthracene groups and also show similarities with the HOMO orbital of S_0 . Therefore, the solvation of T_1 is expected to resemble the solvation of S_0 in BN.

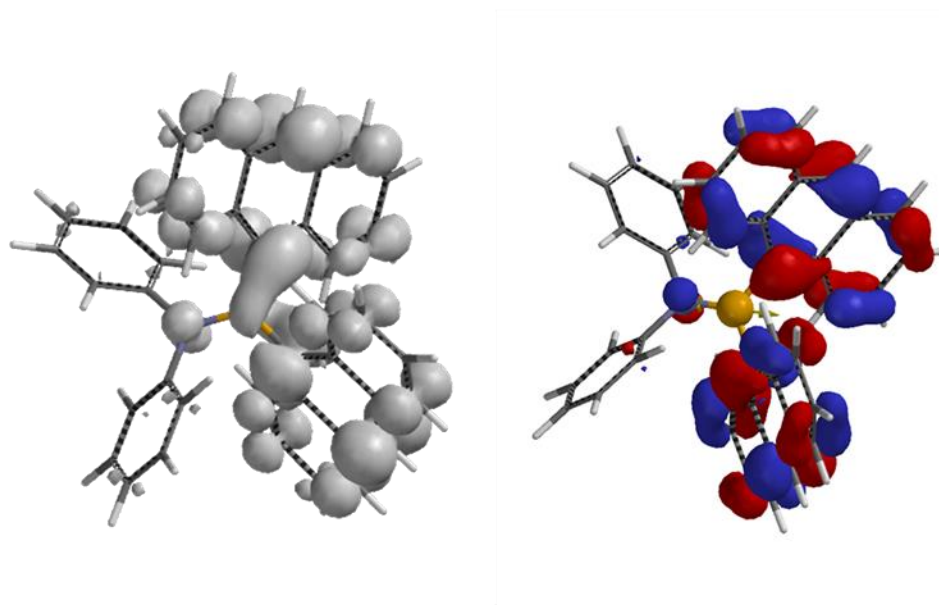


Figure 5.16 DFT calculated spin density of the triplet state in comparison with the HOMO orbital of S_0 of BN.

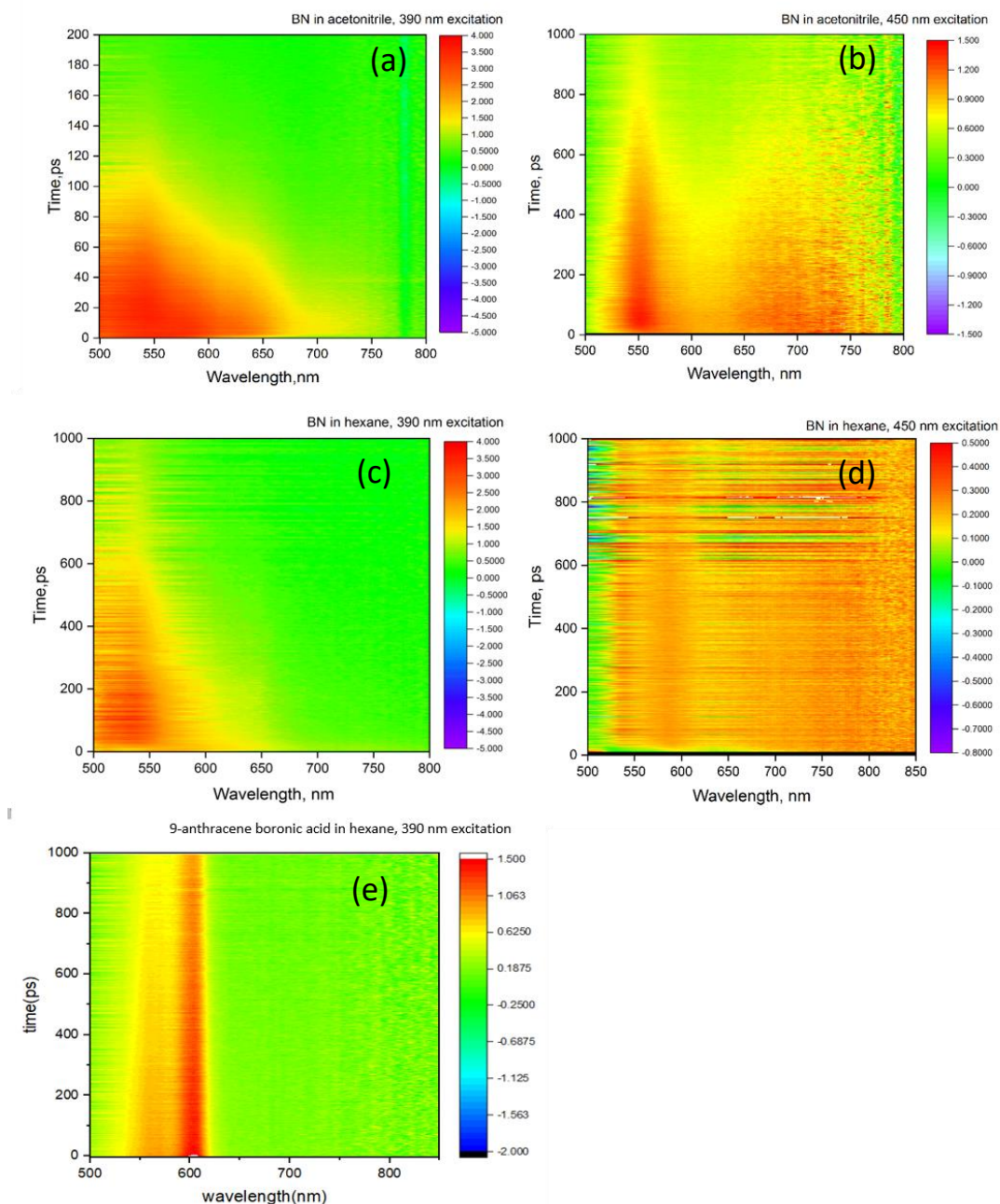


Figure 5.17 2D transient absorption maps of BN molecule in acetonitrile and hexane obtained upon 390 nm and 450 nm excitation. The transient spectrum of the reference compound 9-anthracene boronic acid in hexane obtained upon excitation of 390 nm is shown at the bottom.

1D transient absorption spectra at different delay times are extracted from the 2D maps. Figure 5.18 shows the spectra for BN with 390 nm excitation. Except for the broader absorption band in acetonitrile, an apparent rise at around 650 nm is observed in both spectra.

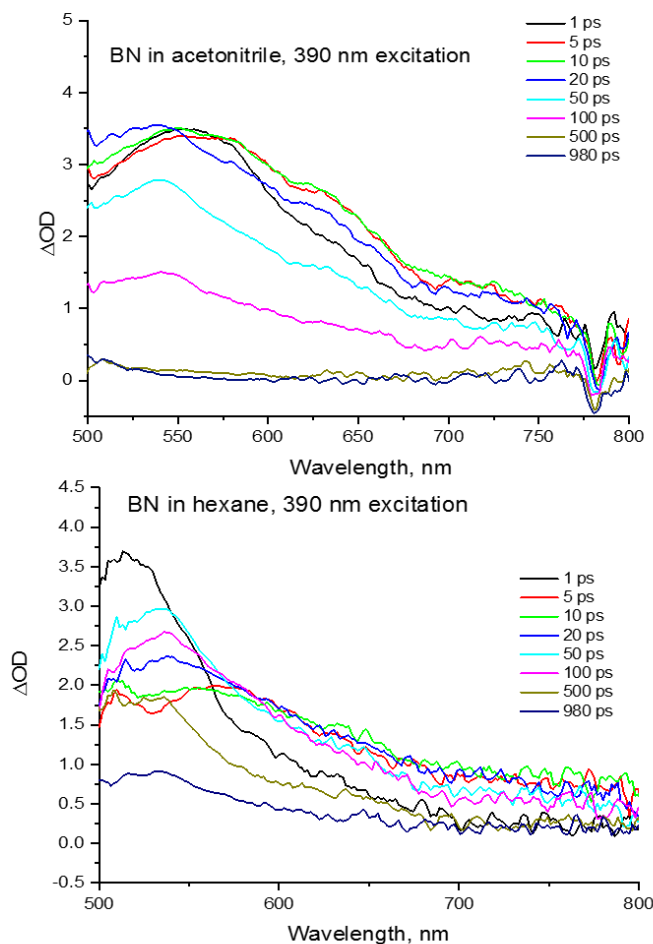


Figure 5.18 1D transient absorption spectra of BN with 390 nm excitation in acetonitrile and in hexane.

The rising absorption is assigned to the formation charge separated/shifted state S_1 . This assignment can be bolstered by the comparison of the transient absorption maps of BN and

9-anthracene boronic acid in hexane with 390 nm excitation (Figure 5.17c, e). The additional absorption feature observed for BN at around 650 nm can be attributed to the S_1 . The broader band for transient spectra in acetonitrile can be explained by the thermodynamic parameters obtained from the fitting of the charge transfer emission described in 5.3.2. The driving force for the transition from S_A to S_1 is $\Delta G_{0,S_A \rightarrow S_{cs}} = -0.5$ eV. A comparison with solvent reorganization energies in acetonitrile (0.33 eV) and in hexane (0.13 eV) indicates that the transition in both solvents lies in the Marcus inverted region. As shown in the diagram (Figure 5.19), with the energy level of S_1 remains the same, a larger solvent reorganization energy in acetonitrile corresponds to a lateral displacement away from S_A , which leads to a broader range of S_1 transient absorption with respect to S_A .

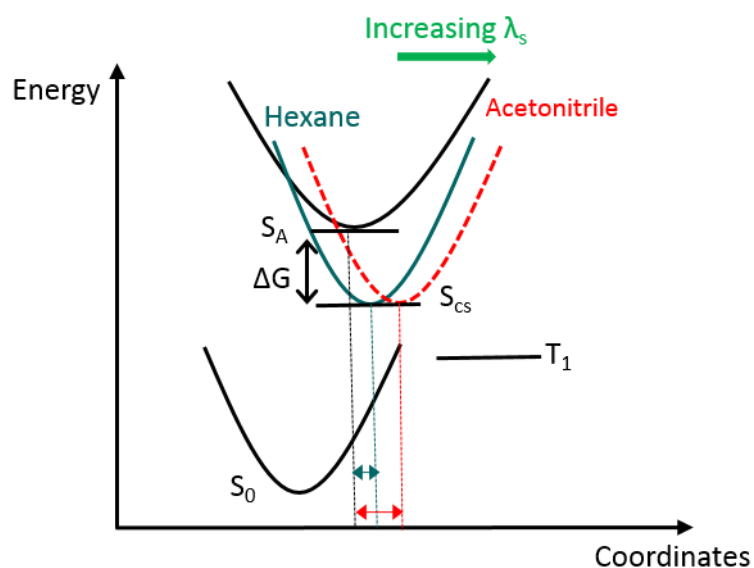


Figure 5.19 Schematic diagram of the energy levels involved in the deactivation of the S_A state in BN molecule.

Being in the Marcus inverted region also implies that the transition from S_A to S_{cs} (S_1) is faster in acetonitrile due to the relatively larger solvent reorganization energy. This is confirmed by the decay kinetics probed at 700 nm in both solvents (Figure 5.19). An apparent shorter rise time can be observed for the transient kinetics in acetonitrile. The corresponding single exponential growth fitting parameters summarized in Table 5.3 show that the formation time of S_1 in acetonitrile is approximately 30% faster than the one in hexane.

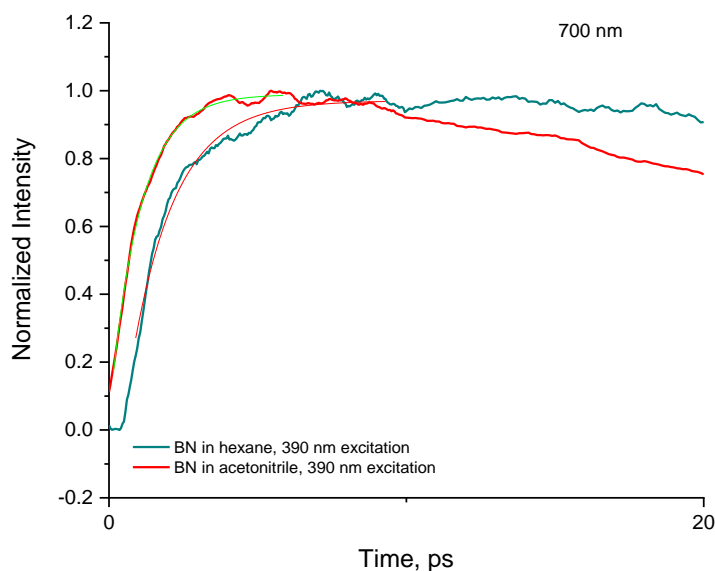


Figure 5.20 Transient decay kinetics of BN obtained upon 390 nm excitation in acetonitrile and in hexane, probed at 700 nm.

BN 390 nm excitation	τ_1 , ps	A_1	Y_0
In acetonitrile	-1.0 ± 0.01	-0.94 ± 0.006	0.99 ± 0.002
In hexane	-1.4 ± 0.04	-1.3 ± 0.03	0.97 ± 0.003

Table 5.3 Single exponential growth fitting parameters gathered for transient decay kinetics upon 390 nm excitation of BN in acetonitrile and hexane.

Transient absorption spectra with excitation of 450 nm also exhibit initial growth, which is caused by the formation of triplet state of BN. In acetonitrile, this growth starts from negative absorption which is caused by strong stimulated emission around 550 nm. In hexane, the growth at early times extends to almost the entire spectrum, indicating a much slower formation of both T_1 absorption peaks in such solvent.

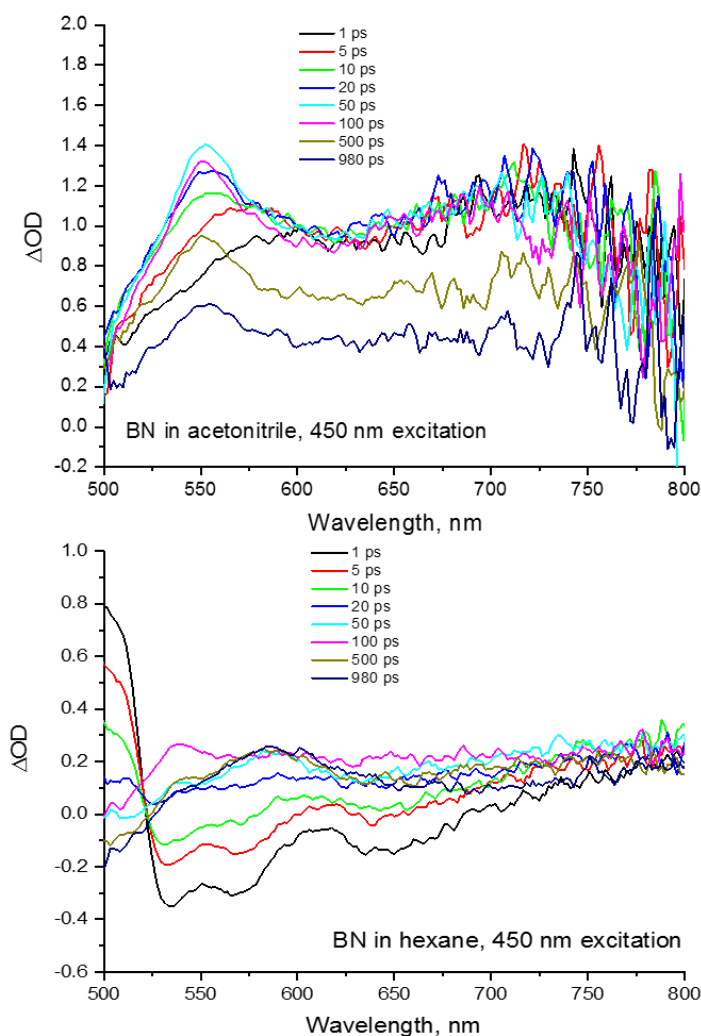


Figure 5.21 1D transient absorption spectra of BN obtained upon 450 nm excitation in acetonitrile and in hexane.

As stated earlier, the solvation of the triplet of BN should be very similar to the S_0 . As a result, the same thermodynamic parameters obtained above can therefore be used once more for the analysis of the transition from S_1 to T_1 .

The driving force for the transition, $\Delta G_{0,S_{CS} \rightarrow T_1} = 0.38$ eV, compared with the solvent reorganization energies in acetonitrile (0.33 eV) and hexane (0.13 eV) indicates that the

process is again in the Marcus inverted region. The $S_1 \rightarrow T_1$ intersystem crossing rate in hexane is thus slower than in acetonitrile. Furthermore, since the $\lambda_{S, ACN}$ is nearly matching the driving force, the transition in acetonitrile is very close to the Marcus maximum, which means that the formation of T_1 state in this solvent should be very fast.

The transient decay kinetics probed at 700 nm in both solvents confirm the above analysis, with an almost immediate formation of T_1 (0.6 ps) observed in acetonitrile while the time needed in hexane is on the scale of 10 ps. The electronic component of the $S_1 \rightarrow T_1$ intersystem crossing process is determined by the spin-orbit coupling and therefore it is not expected to depend on solvent polarity.

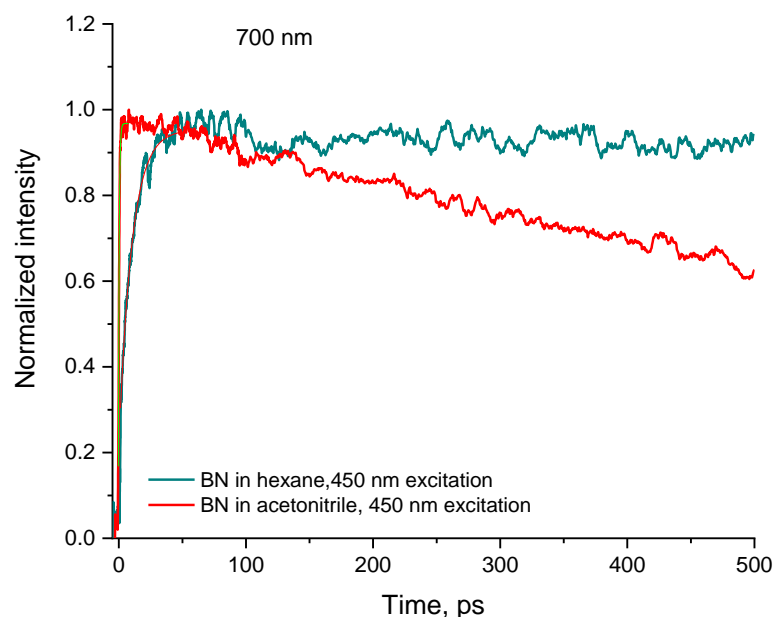


Figure 5.22 Transient decay kinetics of BN obtained upon 450 nm excitation in acetonitrile and in hexane, probed at 700 nm.

BN 450 nm excitation	τ_1 , ps	A_1	Y_0
In acetonitrile	-0.61 ± 0.01	-0.45 ± 0.005	0.97 ± 0.002
In hexane	-10 ± 0.12	-0.74 ± 0.004	0.95 ± 0.002

Table 5.4 Single exponential growth fitting parameters gathered for transient decay kinetics upon 450 nm excitation of BN in acetonitrile and hexane.

5.4 Conclusion

The solvent effects on the excited state dynamics in a borazene compound containing sterically crowded anthracene groups were carefully studied by pump-probe spectroscopy augmented by DFT calculations and fluorescence analysis by the semi-classical Marcus-Jortner equation. A complex interplay between fully localized S_A , partially delocalized and charge separated states S_1 , as well as intersystem crossing to T_1 emerges from the analysis. The observed “charge shift” band at 475 nm in ground state UV-VIS spectrum originates from an electron density shift from anthracene to boron atom. The subsequent charge transfer fluorescence shows quenching effects in more polar solvents with only a modest Stokes shift. Fitting of these charge transfer fluorescence spectra allowed us to determine the driving forces and solvent reorganization energies in different solvents. The driving forces are nearly constant in all solvents, while the solvent reorganization energy increases in more polar solvents. The results show that the modest Stokes shift is caused primarily by the reversal of the orientation rather than change of the magnitude of the dipole moment upon transition from S_1 to S_0 state in these solvents.

Thermodynamic calculations regarding transitions between S_A , S_1 and T_1 states were carried out using the parameters obtained from the fitting. The results show that both $S_A \rightarrow S_1$ transition and $S_1 \rightarrow T_1$ intersystem crossing process lie in the Marcus inverted region

and therefore should accelerate in solvents with larger λ_S . Transient absorption measurements in acetonitrile and in hexane corroborate the prediction based on the calculations. An almost 30% faster formation of the S_1 state in acetonitrile in comparison with in hexane was observed with direct excitation to localized state S_A at 390 nm and probed at 700 nm. Similar trend was also observed with 450 nm excitation and 700 nm probe, where rise of the T_1 signal in acetonitrile was nearly immediate in comparison with a significantly much slower formation in hexane.

References

1. Yamaguchi, S. and K. Tamao, *Theoretical study of the electronic structure of 2,2'-bisilole in comparison with 1,1'-bi-1,3-cyclopentadiene: $\sigma^*-\pi^*$ conjugation and a low-lying LUMO as the origin of the unusual optical properties of 3,3',4,4'-tetraphenyl-2,2'-bisilole*. Bulletin of the Chemical Society of Japan, 1996. **69**(8): p. 2327-2334.
2. Yamaguchi, S., et al., *Dibenzoborole-containing π -electron systems: remarkable fluorescence change based on the "On/Off" control of the $p\pi-\pi^*$ conjugation*. Journal of the American Chemical Society, 2002. **124**(30): p. 8816-8817.
3. Yamaguchi, S. and K. Tamao, *A key role of orbital interaction in the main group element-containing π -electron systems*. Chemistry Letters, 2005. **34**(1): p. 2-7.
4. Salzner, U., et al., *Comparison of geometries and electronic structures of polyacetylene, polyborole, polycyclopentadiene, polypyrrole, polyfuran, polysilole, polyphosphole, polythiophene, polyselenophene and polytellurophene*. Synthetic Metals, 1998. **96**(3): p. 177-189.
5. Entwistle, C.D. and T.B. Marder, *Boron chemistry lights the way: optical properties of molecular and polymeric systems*. Angewandte Chemie International Edition, 2002. **41**(16).
6. Lambert, C., et al., *Polarisierte π -Elektronensysteme in einem chemisch erzeugten elektrischen Feld: nichtlineare optische Eigenschaften zweiter Ordnung von Ammonium-Borat-Zwitterionen*. Angewandte Chemie, 1996. **108**(6): p. 710-712.
7. Glogowski, M.E., et al., *Boron photochemistry*. Journal of Organometallic Chemistry, 1974. **74**(2): p. 175-183.

8. *Boron-Nitrogen Compounds*. Anorganische und Allgemeine Chemie in Einzeldarstellungen. 1965.
9. Taniguchi, T., et al., *TICT fluorescence of N-borylated 2,5-diarylpyrroles: a gear like dual motion in the excited state*. Dalton Trans., 2013. **42**(3): p. 620-624.
10. Hancock, K.G., et al., *Fluorescence spectra of aminoboranes. The nature of emission in boron—nitrogen analogs of stilbene and styrene and characterization of aminoborane singlet excited states*. Journal of Organometallic Chemistry, 1975. **90**(1): p. 23-39.
11. Cornelissen-Gude, C. and W. Rettig, *An Experimental and ab Initio CI Study for Charge Transfer Excited States and Their Relaxation in Pyrroloborane Derivatives*. The Journal of Physical Chemistry A, 1999. **103**(22): p. 4371-4377.